

University of Windsor

## Scholarship at UWindor

---

Electronic Theses and Dissertations

Theses, Dissertations, and Major Papers

---

8-15-2019

# Wear and Fatigue Behaviour of Additive Manufactured Titanium with TiB Particles

Liza-Anastasia DiCecco  
*University of Windsor*

Follow this and additional works at: <https://scholar.uwindsor.ca/etd>

---

### Recommended Citation

DiCecco, Liza-Anastasia, "Wear and Fatigue Behaviour of Additive Manufactured Titanium with TiB Particles" (2019). *Electronic Theses and Dissertations*. 7782.  
<https://scholar.uwindsor.ca/etd/7782>

This online database contains the full-text of PhD dissertations and Masters' theses of University of Windsor students from 1954 forward. These documents are made available for personal study and research purposes only, in accordance with the Canadian Copyright Act and the Creative Commons license—CC BY-NC-ND (Attribution, Non-Commercial, No Derivative Works). Under this license, works must always be attributed to the copyright holder (original author), cannot be used for any commercial purposes, and may not be altered. Any other use would require the permission of the copyright holder. Students may inquire about withdrawing their dissertation and/or thesis from this database. For additional inquiries, please contact the repository administrator via email ([scholarship@uwindsor.ca](mailto:scholarship@uwindsor.ca)) or by telephone at 519-253-3000ext. 3208.

Wear and Fatigue Behaviour of Additive Manufactured Titanium with TiB Particles

By

Liza-Anastasia DiCecco

A Thesis  
Submitted to the Faculty of Graduate Studies  
through the Department of Mechanical, Automotive and Materials Engineering in  
Partial Fulfillment of the Requirements for  
the Degree of Master of Applied Science  
at the University of Windsor

Windsor, Ontario, Canada

2019

© 2019 Liza-Anastasia DiCecco

Wear and Fatigue Behaviour of Additive Manufactured Titanium with TiB Reinforcement

By

Liza-Anastasia DiCecco

APPROVED BY:

---

R. J. Urbanic  
Department of Mechanical, Automotive and Materials Engineering

---

A. Alpas  
Department of Mechanical, Automotive and Materials Engineering

---

A. Edrisy, Advisor  
Department of Mechanical, Automotive and Materials Engineering

August 15, 2019

## **DECLARATION OF ORIGINALITY**

I hereby certify that I am the sole author of this thesis and that no part of this thesis has been published or submitted for publication.

I certify that, to the best of my knowledge, my thesis does not infringe upon anyone's copyright nor violate any proprietary rights and that any ideas, techniques, quotations, or any other material from the work of other people included in my thesis, published or otherwise, are fully acknowledged in accordance with the standard referencing practices. Furthermore, to the extent that I have included copyrighted material that surpasses the bounds of fair dealing within the meaning of the Canada Copyright Act, I certify that I have obtained a written permission from the copyright owner(s) to include such material(s) in my thesis and have included copies of such copyright clearances to my appendix.

I declare that this is a true copy of my thesis, including any final revisions, as approved by my thesis committee and the Graduate Studies office, and that this thesis has not been submitted for a higher degree to any other University or Institution.



## ABSTRACT

While titanium remains an attractive candidate in lightweighting applications, it is often restricted in use due of its poor tribological behaviour and inferior machinability characteristics, leading to its higher relative cost. To address these shortcomings, manufacturers are turning towards alternate, non-conventional manufacturing methods such as additive manufacturing (AM). The mechanical and microstructural properties of alpha, near-commercially pure, titanium made from a novel AM process, termed plasma transferred arc solid free form fabrication, is studied in this research work. Low amounts of titanium-boride (TiB) particles are of interest in as-received samples for their role as a stiffener and strengthener, which can lead to improvements in mechanical and tribological behaviour. This investigation focuses on understanding how the AM build metallurgy and TiB in studied samples influences the mechanical and tribological behaviour of samples. Specially, the research concentrates on wear characterization through ball-on-disk testing and the fatigue behaviour found through rotating-bending testing. Moreover, a final goal of the work was to explore the influence of shot-peening to improve the fatigue and wear behaviour of this material. The investigation revealed that as-received AM blocks showed a near-isotropic behaviour within the structure. Transitional wear behaviour was noted which occurred at the 10N applied loading condition but did not occur in shot-peened samples, which stayed within the first wear regime described. Shot-peening was also found to result in improved fatigue values, increasing the fatigue resistance of samples by 28%, and led to maintained wear resistance with similar COF and wear rate values obtained.

## **DEDICATION**

*To my family and friends, whose love and support brought me this far.*

## ACKNOWLEDGEMENTS

To begin, I would like to express my sincerest and deepest gratitude to my advisor Dr. A. Edrisy for her guidance, mentorship, and continuous support throughout my graduate studies. I would also like to thank my other committee members, Dr. J. Urbanic and Dr. A. Alpas, for their time spent on my committee, their helpful feedback, as well as their insightful suggestions during my studies. The support of the Natural Sciences and Engineering Research Council of Canada (NSERC) in the pursuit of my studies and in this research work funding is also greatly acknowledged.

I would like to sincerely express my gratitude to my research colleagues, particularly Dr. R. Riahi, Dr. O. Gali, Mr. L. Chauvin, Mr. T. Tran, Dr. M. Mehdi, Dr. M. Alam, and Mr. D. Munghen. I truly appreciate all of your support, guidance, training, and company that you have provided me throughout my studies. Special thanks go out to the hard-working and amazing technicians at the University of Windsor who went above and beyond to help me finish my work, particularly Mr. A. Jenner, Mr. K. Harkai, Mr. B. Middleton, and Mr. M. St Louis, for their technical assistance and support. I am extremely grateful and thankful to have been trained and mentored by Ms. S. Lackie on advanced microscopy techniques using scanning electron microscopy (SEM) through the Great Lakes Institute for Environmental Research (GLIER), who helped foster my passion for SEM and love of microscopy.

Last of all, I would like to thank my family and friends for their love and support throughout my studies. I truly appreciate all the patience and encouragement that they have shown me during my graduate studies, without which I would have

surely failed in my endeavors. A special thanks goes out to Anthony, Alexa, and Alexandra, who have listened to my countless hours of talking about titanium and helped with proofreading more documents and presentations than I can count.

# TABLE OF CONTENTS

DECLARATION OF ORIGINALITY .....	iii
ABSTRACT .....	iv
DEDICATION .....	v
ACKNOWLEDGEMENTS .....	vi
LIST OF TABLES .....	x
LIST OF FIGURES .....	xi
NOMENCLATURE .....	xix
CHAPTER 1: INTRODUCTION .....	1
1.1 Background and Motivation .....	1
1.2 Objectives of Study .....	2
1.3 Organization of Thesis .....	3
CHAPTER 2: LITERATURE SURVEY .....	4
2.1 Introduction .....	4
2.2 Titanium Alloys .....	4
2.3 Tribological Behaviour of Titanium Alloys .....	10
2.4 Fatigue Behaviour of Titanium Alloys .....	11
2.5 Shot-peening of Titanium Alloys .....	14
2.5.1 Shot-peening Treatment .....	14
2.5.2 Shot-peening Influence on Tribological Behaviour of Titanium Alloys	15
2.5.3 Shot-peening Influence on Fatigue Behaviour of Titanium Alloys ..	17
2.6 TiB Particle Reinforcement in Titanium Alloys .....	19
2.6.1 Morphology and Crystallography of TiB .....	23
2.6.2 TiB Influence on Tribological Behaviour of Titanium Alloys .....	26
2.6.3 TiB Influence on Fatigue Behaviour of Titanium Alloys .....	29
2.7 Additive Manufacturing Fundamentals .....	32
2.7.1 Titanium Additive Manufactured Parts Made Through Directed	
Energy Deposition .....	35
2.7.2 Applications of Additive Manufactured Titanium Parts .....	37
CHAPTER 3: MATERIALS AND EXPERIMENTAL METHODS .....	41
3.1 Material: Additive Manufactured Titanium Featuring TiB Reinforcement	
41	
3.2 Metallography Characterization Methods .....	42
3.2.1 Sample Preparation for Cross-Sectional Analysis .....	42
3.2.2 X-Ray Spectroscopy .....	44
3.2.3 TiB Image Analysis .....	44
3.2.4 Focused Ion Beam and Transmission Electron Microscopy .....	46
3.3 Shot-peening Process .....	49

3.4	Mechanical Testing Methods .....	50
3.4.1	Rockwell Hardness Testing .....	50
3.4.2	Microhardness Testing.....	51
3.4.3	Nanohardness Testing.....	52
3.4.4	Uniaxial Compression Testing.....	54
3.4.5	Uniaxial Tensile Testing.....	55
3.4.6	Rotation Bending Fatigue Testing .....	57
3.5	Evaluation of Tribological Properties .....	59
3.5.1	Ball-on-Disk Testing.....	59
CHAPTER 4: EXPERIMENTAL RESULTS .....		63
4.1	Metallography Characterization.....	63
4.1.1	Microstructural Characterization .....	63
4.1.2	X-Ray Spectroscopy .....	64
4.1.3	TiB Image Analysis .....	64
4.1.4	Focused Ion Beam and Transmission Electron Microscopy.....	67
4.2	Shot-peening Microstructure Analysis.....	71
4.3	Mechanical Testing .....	73
4.3.1	Rockwell Hardness Testing .....	73
4.3.2	Microhardness Testing.....	73
4.3.3	Nanohardness Testing.....	74
4.3.4	Compression .....	76
4.3.5	Tensile Testing.....	77
4.3.6	Fatigue Testing.....	81
4.4	Ball-on-disk Testing.....	90
4.4.1	Coefficient of Friction and Wear Rates .....	90
4.4.2	SEM Observations of Worn Surfaces and Debris Particles.....	94
4.4.3	Subsurface Damage .....	106
CHAPTER 5: DISCUSSION.....		110
5.1	Mechanical Behaviour of the Ti-TiB PTA-SFFF Material .....	110
5.2	Tribological Behaviour of the PTA-SFFF Ti-TiB Material.....	116
CHAPTER 6: CONCLUSIONS .....		123
6.1	Conclusions .....	123
6.2	Recommendations .....	126
REFERENCES .....		128
APPENDIX A: RESEARCH CONTRIBUTIONS.....		139
VITA AUCTORIS .....		141

## LIST OF TABLES

<b>Table 2.1.</b> Some important characteristics of titanium and titanium based alloys as compared to other structural metallic materials based on Fe, Ni, and Al [3] .....	5
<b>Table 4.1.</b> Average TiB analysis distribution summary obtained from three SEM micrographs at 200x magnification, with presented sample standard deviation values .....	65
<b>Table 4.2.</b> Hardness results for AM PTA-SFFF Ti-TiB .....	73
<b>Table 4.3.</b> Result summary of the mechanical properties achieved through the fabrication of PTA-SFFF Ti-TiB samples obtained by nanoindentation.....	76
<b>Table 4.4.</b> Compression result summary for longitudinal, lateral, and diagonally oriented AM Ti-TiB samples .....	76
<b>Table 4.5.</b> Tensile result summary for longitudinal, lateral, and diagonally oriented AM Ti-TiB samples .....	78

## LIST OF FIGURES

<b>Fig. 2.1.</b> (a) Unit cell of alpha phase and (b) unit cell of beta phase at 900°C [3] ...	6
<b>Fig. 2.2.</b> Effect of alloying elements on phase diagrams of titanium alloys [3] .....	9
<b>Fig. 2.3.</b> Influence of shot-peening surface treatment [34].....	14
<b>Fig. 2.4.</b> Room temp, in air rotating beam fatigue results from Wagner and Luetjering, highlighting S-N curves of rounded Ti-6Al-4V samples with loading axis parallel to rolling direction (done prior to testing at 800°C) for conditions: A: Shot-peened, B: A + annealed 1h 500 °C in vacuum, C: A + 20µm surface removal, D: B + 20µm surface removal [33].....	19
<b>Fig. 2.5.</b> Boron-titanium equilibrium phase diagram [70].....	23
<b>Fig. 2.6.</b> Common metal additive manufacturing methods. Chart created based on information found in Ref. [82].....	33
<b>Fig. 2.7.</b> AM general process flow used to build metal parts through DED .....	34
<b>Fig. 3.1.</b> PTA-SFFF Ti-TiB block highlighting directions considered during mechanical testing. Enclosed in the red dashed square (not to scale) highlights the approximate area in which samples were cut from using wire electrical discharge machining (EDM). This is to show that blocks were squared off to remove any scaling from the AM process and roughness on the outside surface, which may have an influence on testing.....	41
<b>Fig. 3.2.</b> (a) Secondary electron SEM image showing the typical cross-section microstructure of the PTA-SFFF Ti-TiB samples used in this investigation, etched in Kroll's etchant (500X). (b) Shows the same image, after processing through thresholding with the ImageJ software to isolate TiB particles (in black) from the Ti matrix (white). (c) Final processed image obtained after the 'Analyze Particles' function was employed using the ImageJ software. Contours show particles which are counted in the analysis and red dots appear in the image for every particle counted.....	46
<b>Fig. 3.3.</b> SE SEM images procedure steps taken to prepare a sample for TEM observation through FIB milling. (a) Highlighted by the black and white line is the area of interest chosen for TEM observation to be milled out, which intersects TiB particles. (b) Shows the carbon coating process to protect the surface during milling while (c) shows the sections that were milled out through FIB around the	



area of interest. (d) Shows the lift-out process where the area of interest is micro-welded onto the tip of a needle and transferred to a separate stage seen in (e). (f) Shows the final preparation step, where the sample area of interest for TEM observation was slowly reduced using FIB to create a very thin wafer-like section. ....48

**Fig. 3.4.** Tensile sample dimensions used in testing (in mm).....56

**Fig. 3.5** Fatigue sample dimensions used in testing (in mm) .....58

**Fig. 3.6.** Circles highlighting generally how wear coupons were cut from AM Ti-TiB PTA-SFFF blocks using wire EDM (note: circles are not to scale). ..... 60

**Fig. 3.7.** (a) UMT CETR Bruker tribometer used to conduct pin-on-disk wear tests and (b) schematic illustrating the pin-on-disk testing configurations used for testing and sample specifications..... 61

**Fig. 4.1.** Secondary electron (SE) SEM image showing (a) the typical cross-section microstructure of the PTA-SFFF Ti-TiB samples used in this investigation, etched in Kroll's etchant. (b) Highlights the higher magnification SEM image from the enclosed box region from (a), which helps show that the microstructure is comprised of an alpha grain Ti with TiB 2<sup>nd</sup> phase fibers appearing at and within Ti grain boundaries. .... 63

**Fig. 4.2.** XRD crystallographic patterns of PTA-SFFF Ti-TiB samples studied, showing definite peaks which are consistent with TiB and the hexagonal structure of alpha Ti. .... 64

**Fig. 4.3.** Average distribution patterns for the TiB particles featured in the longitudinal PTA-SFFF Ti-TiB microstructures calculated from three SEM micrographs at 200x magnification. (a) Distribution of TiB aspect ratios (height/width) versus frequency, (b) distribution of TiB particle widths versus frequency, and (c) distribution of TiB particle heights versus frequency..... 66

**Fig. 4.4.** Average distribution patterns for the TiB particles featured in the lateral PTA-SFFF Ti-TiB microstructures calculated from three SEM micrographs at 200X magnification. (a) Distribution of TiB aspect ratios (height/width) versus frequency, (b) distribution of TiB particle widths versus frequency, and (c) distribution of TiB particle heights versus frequency..... 67

**Fig. 4.5.** FIB cross-section of the AM Ti-TiB sample observed using SEM ..... 69

**Fig. 4.6.** (a) TEM image taken from the enclosed region highlighted in Fig. 4.5. (b) HR-TEM image featuring a Ti-TiB interface in the material, taken from the enclosed dashed circular region as highlighted in (a). ..... 69

**Fig. 4.7.** SAED crystal patterns obtained from Fig 4.6 of (a) TiB and (b) Ti. .... 70

**Fig. 4.8.** (a) TEM region taken from the enclosed dash square area featured in Fig. 4.6. (b) EELS map of the area in (a), highlighting the presence of boron in yellow and titanium in green. (c) TEM line scan figure highlighting the interface of the TiB to the Ti matrix, from the dashed line featured in (a). ..... 70

**Fig. 4.9.** Secondary electron SEM image showing (a) the typical sub-surface cross-section microstructure of a PTA-SFFF Ti-TiB coupon subjected to shot-peening and polished, treatment as described in section 3.3, etched in Kroll’s etchant. (b) Highlights the higher magnification SEM image from the enclosed box region from (a), showing microstructural hatched features as a result of shot-peening. ... 72

**Fig. 4.10.** Average microhardness profile versus depth into the sample of a polished, shot-peened PTA-SFFF Ti-TiB coupon in red in comparison to an untreated PTA-SFFF Ti-TiB coupon. .... 72

**Fig. 4.11.** Representative nanoindentation load-displacement curves of the PTA-SFFF Ti-TiB material at the loading conditions of 1, 2 and 3 mN..... 75

**Fig. 4.12.** Overall results of nano-indentation testing showing load-displacement curves of the PTA-SFFF Ti-TiB material at the loading conditions of 1, 2, and 3 mN..... 75

**Fig. 4.13.** Directionally oriented compression testing results for the AM Ti-TiB material, presented in the form of engineering stress versus percent strain. .... 77

**Fig. 4.14.** Directionally oriented tensile testing results for the AM Ti-TiB material, presented in the form of engineering stress versus percent strain. .... 79

**Fig. 4.15.** SEM imaging of the tensile fracture surface of the longitudinal sample 1 through (a) BSE and (b) SE. .... 80

**Fig. 4.16.** (a) SE SEM image showing representative tensile fracture surface of the longitudinal sample 1, highlighting typical fracture features observed. (b) SE SEM higher magnification image taken from the enclosed area as highlighted in (a), exhibiting dimpled morphology. (c) SE SEM higher magnification image taken from the enclosed area as highlighted in (a), showing a less-ductile, more cleaved region in the same area. .... 81

**Fig. 4.17.** Fatigue stress amplitude versus number of cycles, S-N diagram from the untreated and shot-peened PTA-SFFF Ti-TiB material..... 85

**Fig. 4.18.** (a) BSE SEM image highlighting the overall fracture surface of a PTA-SFFF Ti-TiB fatigue sample which was tested at a stress amplitude of 307.5 MPa and failed at 105,300 cycles. (b) BSE SEM image highlighting the fatigue crack origin and crack propagation, taken from the enclosed area in Region I highlighted in (a). (c) SE SEM image showing a dimpled fracture surface with TiB particles, taken from the enclosed area in the Final Rupture region highlighted in (a). ..... 86

**Fig. 4.19.** (a) BSE SEM image highlighting the overall fracture surface of a PTA-SFFF Ti-TiB fatigue sample which was tested at a stress amplitude of 432.5 MPa and failed at 24,600 cycles. (b) SE SEM image highlighting the fatigue crack origin and crack propagation, taken from the enclosed area in Region I highlighted in (a). (c) SE SEM image showing a cracked fracture surface with TiB particles, taken from the enclosed area in the Final Rupture region highlighted in (a). ..... 87

**Fig. 4.20.** (a) BSE SEM image highlighting the overall fracture surface of a shot-peened PTA-SFFF Ti-TiB fatigue sample which was tested at a stress amplitude of 382.5 MPa and failed at 506,700 cycles. (b) BSE SEM image highlighting the fatigue crack origin area, taken from the enclosed area in Region I highlighted in (a). (c) SE SEM image showing a cross-hatched, cracked fracture surface, taken from the enclosed area in the Final Rupture region highlighted in (a). ..... 88

**Fig. 4.21.** (a) BSE SEM image highlighting the overall fracture surface of a shot-peened PTA-SFFF Ti-TiB fatigue sample which was tested at a stress amplitude of 507.5 MPa and failed at 48,000 cycles. (b) BSE SEM image highlighting the fatigue crack origin area, taken from the enclosed area in Region I highlighted in (a). (c) SE SEM image showing a dimpled structure with TiB particles within dimples, taken from the enclosed area in the Final Rupture region highlighted in (a). ..... 89

**Fig. 4.22.** Variation of the coefficient of friction (COF) with sliding distance for representative applied loading schemes of 2, 6, 10 and 15N, for the PTA-SFFF Ti-TiB samples in the (a) untreated and (b) shot-peen treated conditions..... 91

**Fig. 4.23.** Variation of the average COF as a function of applied load for PTA-SFFF Ti-TiB samples, showing an initial increase of average COF and then a gradual decrease with increasing load. .... 91

**Fig. 4.24.** Variation of volumetric wear rate as a function of applied load for the (a) untreated and (b) shot-peened PTA-SFFF Ti-TiB samples, collected from ball-

on-disk style wear tests. Departure from linearity is observed at the 10N applied loading condition for the untreated samples while a consistent linear trend is observed in shot-peened samples.....92

**Fig. 4.25.** Variation of mass wear rate as a function of applied load for the (a) untreated and (b) shot-peened PTA-SFFF Ti-TiB samples, collected from ball-on-disk style wear tests. Departure from linearity is observed at the 10N applied loading condition for the untreated samples while a consistent linear trend is observed in shot-peened samples.....93

**Fig. 4.26.** Variation of mass wear rate as a function of applied load for the AISI 52100 counterface ball samples from the (a) untreated PTA-SFFF Ti-TiB wear testing and (b) the shot-peened PTA-SFFF Ti-TiB wear testing.....93

**Fig. 4.27.** BSE SEM images of (a) the wear scar of the AISI 52100 counterface ball for the 2N applied load untreated PTA-SFFF Ti-TiB sample, with an area size fitted to 0.634 mm<sup>2</sup>. (b) Shows Ti oxide and small platelet on the steel ball as a result of ball-on-disk wear testing against the untreated sample, taken from the area enclosed by the dashed white rectangle in (a). .....95

**Fig. 4.28.** BSE SEM images of (a) the wear scar of the AISI 52100 counterface ball for the 10N applied load untreated PTA-SFFF Ti-TiB sample, with an area size fitted to 1.629 mm<sup>2</sup>. (b) Shows Ti oxide and coarse platelet on the steel ball as a result of ball-on-disk wear testing against the untreated sample, taken from the area enclosed by the dashed white rectangle in (a).....95

**Fig. 4.29.** BSE SEM images of (a) the wear scar of the AISI 52100 counterface ball for the 17.5N applied load untreated PTA-SFFF Ti-TiB sample, with an area size fitted to 2.149 mm<sup>2</sup>. (b) Shows Ti material transfer through large platelets, oxides, and Ti integration directly into the steel ball as a result of ball-on-disk wear testing against the untreated sample, taken from the area enclosed by the dashed white rectangle in (a). .....96

**Fig. 4.30.** BSE SEM images of (a) the wear scar of the AISI 52100 counterface ball for the 2N applied load shot-peened PTA-SFFF Ti-TiB sample, with an area size fitted to 0.716 mm<sup>2</sup>. (b) Shows Ti oxide and small platelet adhesion on the steel ball as a result of ball-on-disk wear testing against the sample, taken from the area enclosed by the dashed white rectangle in (a).....97

**Fig. 4.31.** BSE SEM images of (a) the wear scar of the AISI 52100 counterface ball for the 10N applied load shot-peened PTA-SFFF Ti-TiB sample, with an area size fitted to 1.855 mm<sup>2</sup>. (b) Shows Ti oxide and coarse platelet adhesion on the

steel ball as a result of ball-on-disk wear testing against the shot-peened sample, taken from the area enclosed by the dashed white rectangle in (a). .....98

**Fig. 4.32.** BSE SEM images of (a) the wear scar of the AISI 52100 counterface ball for the 15N applied load shot-peened PTA-SFFF Ti-TiB sample, with an area size fitted to 2.057 mm<sup>2</sup>. (b) Shows Ti material transfer through large platelets, oxides, and Ti integration directly into the steel ball as a result of ball-on-disk wear testing against the shot-peened sample, taken from the area enclosed by the dashed white rectangle in (a). .....98

**Fig. 4.33.** SE SEM image of the 1N load untreated PTA-SFFF Ti-TiB wear track (a) showing fine oxide debris particles on the surface. (b) Higher magnification SE SEM imaging featuring surface abrasion towards the center of the track, taken from the enclosed white dashed rectangle in (a)..... 100

**Fig. 4.34.** SE SEM image of the 8N load untreated PTA-SFFF Ti-TiB wear track highlighting (a) material back-transfer on the track. (b) Higher magnification of a separate area directly in the centre of the track where wear fatigue cracks are observed with fine oxide particle debris featured on the worn surface. .... 100

**Fig. 4.35.** BSE SEM images of the 12.5N load untreated PTA-SFFF Ti-TiB sample wear track (a) showing a portion of the wear track and (b) showing in greater detail the wear morphology of a smaller representative section of the track, taken from the red dashed box in (a). EDS elemental analysis detected that the bright white areas observed were composed dominantly of iron, with chrome, titanium, oxygen, and trace amounts of boron detected, indicative of material transfer from the AISI 52100 ball to the wear track as shown in (b)..... 101

**Fig. 4.36.** SE SEM image of the 1N load shot-peened PTA-SFFF Ti-TiB wear track (a) showing fine oxide debris particles on the surface. (b) Higher magnification SE SEM imaging featuring surface abrasion towards the center of the track, taken from the enclosed white dashed rectangle in (a). ..... 102

**Fig. 4.37.** SE SEM image of the 8N load shot-peened PTA-SFFF Ti-TiB wear track (a) showing fine oxide debris particles on the surface with abrasive tracks. (b) Higher magnification of the area in the enclosed white dashed box in (a) where wear fatigue cracks are observed with fine oxide particle debris featured on the worn surface..... 102

**Fig. 4.38.** BSE SEM images of the 10N load shot-peened PTA-SFFF Ti-TiB sample wear track (a) showing a portion of the wear track and (b) showing in greater detail the wear morphology of a smaller representative section of the track,

taken from the white dashed box in (a). EDS elemental analysis detected that the bright white areas observed were composed dominantly of iron, with chrome, titanium, oxygen, and trace amounts of boron detected, indicative of material transfer from the AISI 52100 ball to the wear track as shown in (b)..... 103

**Fig. 4.39.** Typical SE SEM images of wear debris particles collected during the untreated PTA-SFFF Ti-TiB wear testing. For the 1N applied load, (a) shows Ti oxide debris particles with some loose agglomerated matrix particles, and (b) shows at higher magnification the fine Ti oxide debris particles. For the 10N applied load, highlighted in (c) are coarse detached Ti platelet and agglomerated Ti debris particles, also with fine Ti oxide particles shown in (d). For the 17.5N applied load, (e) shows large detached Ti platelets with smaller wear debris and Ti oxides still present. (f) Highlights the severe plastic deformation of one of the large Ti debris taken from the enclosed dashed rectangle in (e)..... 104

**Fig. 4.40.** Typical SE SEM images of wear debris particles collected during the shot-peened PTA-SFFF Ti-TiB wear testing. For the 1N applied load, (a) shows very fine Ti oxide debris particles, with some larger Ti particles present, and (b) shows at higher magnification the fine Ti oxide debris particles. For the 10N applied load, highlighted in (c) are coarse detached Ti platelet and agglomerated Ti debris particles, also with fine Ti oxide particles shown in (d). For the 15N applied load, (e) shows many large detached Ti platelets with smaller wear debris and Ti oxides still present. (f) Highlights the severe plastic deformation of one of the large Ti debris taken from the enclosed dashed rectangle in (e)..... 105

**Fig. 4.41.** (a) SE SEM image showing the subsurface damage present for the 17.5N PTA-SFFF Ti-TiB wear sample, etched with Kroll’s reagent. (b) Highlights at higher magnification the subsurface damage in the plastic deformation region, showing a TiB particle that is strained and fractured just below the mechanically mixed layer (MML). ..... 106

**Fig. 4.42.** (a) SE SEM image showing the subsurface damage present for the 15N PTA-SFFF Ti-TiB shot-peened wear sample, etched with Kroll’s reagent. (b) Highlights at higher magnification the subsurface damage in the plastic deformation region, showing a TiB particle that is strained and fractured just below the mechanically mixed layer (MML). ..... 107

**Fig. 4.43.** (a) Schematic developed from Fig. 4.41(a), highlighting the procedure used to measure the equivalent plastic strain from the subsurface of the 17.5N untreated and 15N shot-peened treated PTA-SFFF Ti-TiB samples, using strain lines in the microstructure in analysis to refer to. (b) Variation of the average equivalent

plastic strain with respect of depth from the top surface of each sample (MML:  
mechanically mixed layer)..... 109

**Fig. 5.1.** SE SEM images of the PTA-SFFF Ti-TiB structures showing TiB (a)  
large and (b) small agglomerations in the structure..... 113

## NOMENCLATURE

AM	Additive Manufacturing
ASM	American Society for Metals
ASTM	American Society for Testing Metals
bcc	Body-centered cubic
BSE	Back Scatter Electron
CAD	Computer-aided design
CCEM	Canadian Centre for Electron Microscopy
EBM	Electron Beam Melting
EBSD	Electron Back Scatter Diffraction
EDM	Electronic Discharge Machining
EDS	Energy Dispersive X-ray Spectroscopy
EELS	Electron Energy Loss Spectroscopy
fcc	Face-centered cubic
FIB	Focused Ion Beam
GLIER	Great Lakes Institute for Environmental Research
hcp	Hexagonal close-packed
HR-TEM	High-Resolution Transmission Electron Microscopy
HV	Vicker's Hardness
ICP-OES	Inductively Coupled Plasma Optical Emission Spectroscopy
LBM	Laser Beam Melting



MML	Mechanically Mixed Layers
MPIF	Metal Powder Industries Federation
PTA-SFFF	Plasma Transferred Arc Solid Free-Form Fabrication
rpm	Revolutions per minute
SAED	Selected Area Electron Diffraction
SE	Secondary Electron
SEM	Scanning Electron Microscopy
SLM	Selective Laser Melting
TEM	Transmission Electron Microscopy
Ti	Titanium
UTS	Ultimate Tensile Strength
XRD	X-Ray Diffraction

# CHAPTER 1: INTRODUCTION

## 1.1 Background and Motivation

As fuel consumption, dependence on imported fuels, and outputted emissions become a larger focus, limits are being pushed onto industry to become cleaner and greener. Following this trend, to meet future engineering design demands, alternative high-strength, lightweight alloys are being considered as replacement materials for conventionally used heavier alloys to lead to fuel and emission savings. For aerospace and automotive applications, titanium (Ti) makes choice material candidate due to its robust alloying capabilities, high strength-to-weight ratio, corrosion resistance, stability at elevated temperatures, and fatigue resistance [1]–[3]. However, some drawbacks to using Ti remains its poor tribological behaviour and inferior machinability characteristics, which restricts its use in application and are cause for its relative higher cost [2]–[5]. To address these shortcomings, manufacturers are turning towards alternate, non-conventional manufacturing methods such as additive manufacturing (AM) to produce complex Ti parts.

This research explores the potential of a new proprietary AM method termed Plasma Transferred Arc Solid Free Form Fabrication (PTA-SFFF). The process is of interest due to its flexible powder-fed process, large build volume, high build rate, composite structure and particle reinforcement production capability, and near-net shape tolerance capabilities of  $\pm 0.001$  in [6]. This process' ability to produce near-net shaped Ti parts anticipates reducing overall Ti machining needs and thus result in cost-savings related to manufacturing. Moreover, its ability to incorporate particle reinforcement such as TiB

offers advantageous opportunities for producing parts with higher strength and hardness, which can lead to improved tribological characteristics in produced parts [7]–[9].

An initial study from [10] featuring a near commercially pure (CP) Ti reinforced with TiB made from the PTA-SFFF process from this research group singled out the material as it possessed superior mechanical properties in comparison to the select benchmark being replaced and other powder metallurgy (PM) tested materials considered. Therefore, the in-depth mechanical properties and material characterization of this material is of interest as the choice candidate to replace the original benchmark, conventionally used material in the proprietary application. This thesis work offers a comprehensive overview of the properties and performance of this material, particularly regarding its load-induced tribological behaviour as well as overall fatigue behaviour. Better characterization of the PTA-SFFF process is esteemed to lead to better understanding of AM parts made through this process as well as lead to improved adoption rates in the design and fabrication of conventionally made components.

## **1.2 Objectives of Study**

The overall objective of this research is to expand the limited information known about Ti-TiB materials made through the PTA-SFFF AM process. To accomplish this, nearly pure titanium AM blocks featuring low amounts of TiB are studied in this research to evaluate anisotropy in samples and understand how the mechanical and tribological behaviour of samples relates to the AM build metallurgy and featured TiB particles in studied samples. Specifically, the research aims to characterize the wear and fatigue behaviour of samples and correlate observed mechanisms to observed material properties

and microstructural features. The investigation further aims to understand the role of TiB particles in samples and how it influences the mechanical, wear, and fatigue characteristics of samples through microstructural characterization. Last of all, a final goal is to explore the influence of shot-peening as a method to improve the fatigue and wear behaviour of this material.

### **1.3 Organization of Thesis**

The thesis presented herein is separated into six chapters, including the introduction. Following this introduction, chapter 2 will go over a literature review of relevant topics to the research work, which is later presented. This chapter includes a comprehensive review of the general characteristics as well as the tribological and fatigue behaviour of titanium alloys, focusing on additive manufactured titanium alloys reinforced with TiB particles. Furthermore, a brief overview of AM and its use for titanium-based applications as well as a section discussing relevant test methods for evaluating titanium parts made from this manufacturing method is presented.

Chapter 3 concentrates on the experimental methods undertaken in this research work. Chapter 4 presents the results and observations made from testing performed as outlined in Chapter 3. Chapter 5 is the discussion section of this thesis, which aims to overview results and discuss potential mechanisms as to why certain behaviour patterns and observations were made, relating results back to explanations seen in literature as well as from testing parameters used. Finally, chapter six summarizes and concludes the findings of this research work and elaborates on future steps and recommendations that could be taken into consideration in future works.

## **CHAPTER 2: LITERATURE SURVEY**

### **2.1 Introduction**

While titanium and its alloys make attractive material candidates for a diverse set of applications, notably their high strength-to-density ratio, they possess poor machinability and tribological characteristics [1]–[5]. This limits their application and has resulted in their higher relative production costs [4], [5]. To address these shortcomings, manufacturers are turning towards alternate manufacturing methods such as AM.

The study presented concentrates on elaborating the general mechanical and material properties of the AM PTA-SFFF Ti-TiB material, previously introduced in the first chapter, with a focus on wear and fatigue behaviour explored. The focus of this survey is to explore the properties and performance of Ti alloys, with a focus on alpha Ti alloys, as well as the influence of shot-peening, additive manufacturing as well as TiB particles on the mechanical behaviour of Ti. While these aspects are explored through literature, the survey has also shown that limited research is available which overviews the properties and performance of such a specific AM alloy, which makes this work's contribution to research novel.

### **2.2 Titanium Alloys**

Titanium is typically used in aerospace, automotive, bio-medical, and other mechanical applications. Its high-strength-to-weight ratio, good corrosion resistance, stability at elevated temperatures, and fatigue resistance make it a popular material selection for a diverse set of engineering applications. In comparison to commonly used

industrial metals such as iron, nickel, and aluminum, titanium has the highest strength to density ratio of the four materials and has other excellent comparative properties such as corrosion and reactivity with oxygen, as featured in Table 2.1 [3]. Titanium is also a desirable material candidate for applications requiring creep resistance due to its high melting temperature, providing a good advantage in comparison to aluminum. However, titanium alloys are not suited for use above 600°C due to their high reactivity with oxygen and nitrogen, which can cause excess oxide layers to form at the surface and lead to embrittlement [3]. Despite these attractive qualities, titanium is often avoided in materials selection for its inferior machinability, poor tribological behavior as well as high price, which is principally due to manufacturing costs related to its high reactivity with oxygen which limits processing techniques and requires the use of inert gases and high system control [2], [3].

**Table 2.1.** Some important characteristics of titanium and titanium based alloys as compared to other structural metallic materials based on Fe, Ni, and Al [3]

	Ti	Fe	Ni	Al
Melting Temperature (°C)	1670	1538	1455	660
Allotropic Transformation (°C)	$\beta \xrightarrow{882} \alpha$	$\gamma \xrightarrow{882} \alpha$	-	-
Crystal Structure	bcc $\rightarrow$ hcp	fcc $\rightarrow$ bcc	fcc	fcc
Room Temperature Elastic Modulus (GPa)	115	215	200	72
Yield Stress Level (MPa)	1000	1000	1000	500
Density (g/cm <sup>3</sup> )	4.5	7.9	8.9	2.7
Comparative Corrosion Resistance	Very High	Low	Medium	High
Comparative Reactivity with Oxygen	Very High	Low	Low	High
Comparative Price of Metal	Very High	Low	High	Medium

The reactive behaviour of titanium relates to its high affinity for interstitial elements, particularly oxygen and nitrogen, which at elevated temperatures diffused into titanium structures leading to strength increases with ductility loss. Titanium's good corrosion resistance properties are also attributed to its high reactivity with oxygen, as a protective oxide film develops on its surface almost instantaneously when exposed to air

or moisture. Hydrogen is also highly attracted to titanium though must be limited to a maximum allowable concentration of 0.015 wt% to avoid hydrogen embrittlement due to the formation of hydrides [11], [12].

Pure titanium has two distinct crystal structures: hexagonal close-packed (hcp) crystal structure in its alpha ( $\alpha$ ) lower-temperature region phase and body-centered cubic (bcc) in its beta ( $\beta$ ) higher temperature regime phase. Pure titanium is subjected to an allotropic phase transformation at 882°C, where the beta phase transforms to the alpha phase during cooling. Impurities and alloying may raise or low this transition temperature, which is also known as the beta transus temperature [3]. Alpha, beta, and alpha + beta structures compose the three main phases of titanium.

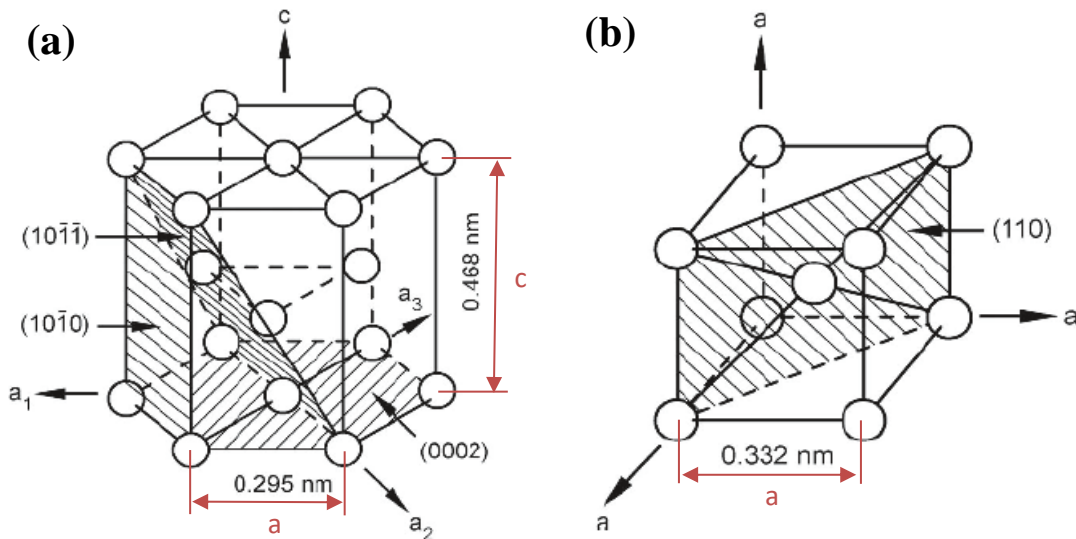


**Fig. 2.1.** (a) Unit cell of alpha phase and (b) unit cell of beta phase at 900°C [3]

The alpha and beta phases of titanium differ significantly due to their difference in metallic crystal structure. As seen in Fig. 2.1(a), the pure alpha titanium phase is a hcp

crystal structure, where lattice parameter values are provided at room temperature,  $a = 0.295$  nm &  $c = 0.468$  nm. The three close-packed planes are indicated in the figure to be the basal or (0002) plane, the {1010} family of planes, and the {1011} family of planes. The three close packed directions are along the  $a_1$ ,  $a_2$ , and  $a_3$  axes within each of the planes and are indicated by the  $\langle 1120 \rangle$  direction indices [3]. There are six atoms per each hcp unit cell, with a coordination number of 12 and an atomic packing factor of 0.74, the same as face-center cubic (fcc) crystal structures though the two structures are distinguished by their difference in stacking sequence; ABABAB for hcp, ABCABCABC for fcc. The ideal lattice parameter ratio of  $c/a$  in the hcp unit cell is 1.633 [13]. Using the given room temperature hcp  $a$  &  $c$  lattice parameters for titanium, the  $c/a$  ratio is 1.586, which is slightly below the ideal ratio [3].

Featured in Fig. 2.1(b) is the unit cell of the beta titanium phase at 900°C, showing the bcc crystal structure and a lattice parameter of  $a = 0.332$  nm. As featured, the closest-packed planes are those belonging to the {110} family and the close-packed directions are the four  $\langle 111 \rangle$  directions [3]. In pure titanium, beta is unstable at room temperature without alloying and thus lattice parameters at room temperature in Fig. 2.1(b) are not shown. There are two atoms per each bcc unit cell, with a coordination number of 8 and an atomic packing factor of 0.68, which is lower than that of the hcp crystal structure [13].

One type of defect that is clearly observed in micrographs for titanium is twinning, which arises from deformation mechanisms for alpha Ti. Twinning occurs when a twin boundary forms, in which a crystal structure is split and appears across a plane as if it were a mirror image due to a shift in atomic position. Low stacking fault energy allows for the formation of twin boundaries inside grain boundaries for some crystal structures such as



fcc. Twin boundaries further block slip and increase the strength of a material [14]. In hcp metals such as alpha titanium alloys, twinning is considered an important part of deformation, having direct influences on improving formability and impact resistance. The ductile behavior of CP Ti and alpha alloys, especially at low temperatures, results primarily from twinning deformation modes along with conventional slip. Twins are easily observed in CP Ti at the onset of deformation though for alpha + beta alloys such as Ti-6Al-4V it is not as often reported. Difference in crystal structures of beta (bcc) and alpha (hcp) particles play a role in this, as alpha + beta phase alloys may produce stress-induced martensite and/or mechanical twins subject to deformation. It is also speculated that less twinning occurs in alpha + beta alloys due to smaller phase dimensions, higher solute concentrations, and the presence of  $Ti_3Al$  precipitates. Twinning occurs less in beta alloys as well though it is also influenced by solute concentrations and only present in the single phase state [3], [15], [16].

As previously mentioned, pure titanium exhibits an allotropic transformation at high temperatures, going from liquid to beta titanium at  $1670^{\circ}C$  to alpha below  $882^{\circ}C$  during solidification [3]. Alloying elements in titanium tend to change this transition temperature. Titanium alloying elements are typically divided into two categories: alpha stabilizers and beta stabilizers. Classification is based on how alloying elements change the beta transus temperature; an alpha stabilizer will increase this temperature while the opposite is true for a beta stabilizer. There exist two types of beta stabilizers, which are classified as isomorphous and eutectoid. Isomorphous beta stabilizers include elements that are soluble in the beta phase, such as alloying elements like molybdenum, vanadium, tantalum, and niobium. The eutectoid beta stabilizer forms a eutectoid system with the

addition of alloying elements like manganese, iron, chromium, cobalt, nickel, copper, and silicon [17]. The general effect of alpha-stabilizers as well as isomorphous and eutectoid beta-stabilizers on the phase diagram of Titanium alloys is shown in Fig. 2.2. Note from Fig. 2.2, some elements, such as zirconium and tin, and have no effect on the beta transus temperature. These elements are added to slow transformation rates and for solid-solution strengthening treatment [3], [17].

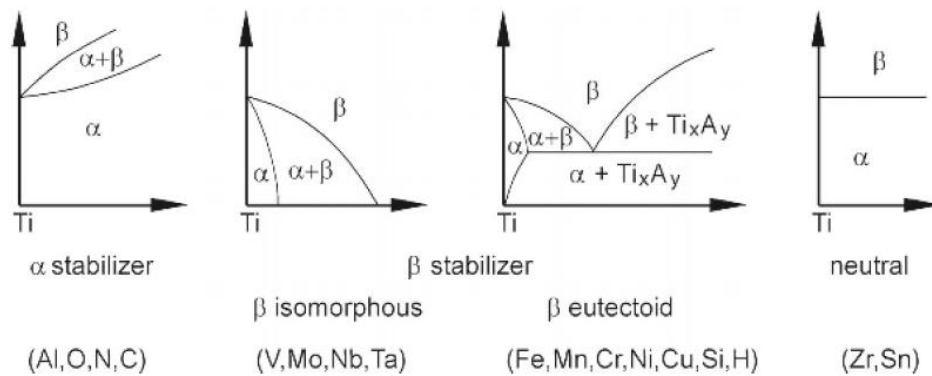


**Fig. 2.2.** Effect of alloying elements on phase diagrams of titanium alloys [3]

Apart from heat treatment and other processing techniques, much of the mechanical properties of CP Ti depends on the presence of interstitial impurities, such as residual elements from processing like carbon, oxygen, and nitrogen. Iron and oxygen interstitials help improve the strength of CP Ti titanium and are often intentionally added during processing. Extra-low interstitial (ELI) grades of titanium exist which have very low levels of impurities, giving them generally better ductility and toughness characteristics [12].

For alpha alloys in particular, typically primary and secondary alpha, or transformed beta, are present in the microstructure. Primary alpha stems from the alpha + beta phase region present during hot working while secondary alpha develops from either the transformation of beta to alpha during cooling below the beta transus temperature or

through aging of either alpha or beta. Secondary alpha developed through aging is too fine to be observed via light optical microscope. Equiaxed alpha grains are generally present in annealed structures while elongated grains result from unidirectional metal working [17].

### **2.3 Tribological Behaviour of Titanium Alloys**

While there are many beneficial material properties of titanium and its alloys which appeal to designers during material selection, their largest drawbacks in use remain their poor tribological behaviour [18]–[21]. Generally, titanium's poor tribological behaviour is attributed to its inferior resistance to plastic shearing and work hardening, low thermal conductivity, as well as low protection exerted by surface oxides, which are quickly removed by spalling or microfragmentation [18]–[20]. The wear behaviour of titanium and its alloys generally include severe adhesion and low abrasion resistance accompanied by high coefficients of friction [19], [21]. Compared to other metals, alpha titanium has a low elastic modulus and low theoretical shear and tensile strength values due to its hcp structure [22], [23]. Moreover, lower strength materials tend to experience more material transfer leading to adhesion wear and titanium's reactivity to oxygen tends to lead to the formation of oxides, which results in oxidation wear as well as adhesion wear from the transfer of oxides between surfaces [23].

In the work of Wang et al. [24], they highlight the poor wear behaviour of CP grade 2 Ti. They attributed the titanium's low hardness to its poor carrying capacity and large contact area formed during subsequent unlubricated, room temperature ball-on-disk wear testing using silicon nitride balls. From wear testing, they noted that the coefficient of friction (COF) was unstable, averaging 0.57. They found that wear testing was dominated

by abrasion wear, with some adhesion wear noted, which led to the formation of abrasive particles. Moreover, they noted that higher transient temperatures at the surface was achieved due to titanium's low coefficient of thermal conductivity, which likely helped contribute to the higher amount of friction during testing as well as led to the substrate and the ball materials to strongly adhere to one another.

In the works of Farokhzadeh and Edrissy [21], the load-induced, dry sliding wear behaviour of Ti-6Al-4V and Ti-10V-2Fe-3Al was explored. Their works highlighted transitional wear behaviour from mild to severe for both alloys, with that of Ti-6Al-4V found to be 3.5 N and for Ti-10V-2Fe-3Al being 9 N. In their study, they showed higher COF values achieved for the two alloys, with values ranging between 0.50 and 0.72, with Ti-10V-2Fe-3Al having had slightly higher COF values. They note that with these alloys similar wear track morphologies are seen in the mild and severe regions, with abraded regions shown with continuous grooves along the sliding direction and wear debris present on the outside of the wear tracks, and highlight that wear was dominated by oxidation as well as the formation and spallation of mechanically mixed layers (MMLs).

## **2.4 Fatigue Behaviour of Titanium Alloys**

Fatigue refers to loading scenarios where cyclic or varying stresses are applied over a period of time at multiple instances [25]. Generally, in service fatigue failure occur after a relatively long period and can be particularly dangerous as it occurs quickly without obvious warning signs and brittle nature [26]. Typically, engineering fatigue data is presented in form of an S-N curve, which highlights the relationship between the life of a sample represented by number of cycles versus applied loads [26]. Similar to ferrous

metals, titanium and its alloys exhibit a fatigue endurance limit, at which below this applied stress limit a sample would not break and would have infinite fatigue life [25], [27]. As the focus of this research is on a near-CP Ti material, this section will focus more specifically on the fatigue behavior of alpha titanium alloys.

For CP Ti alloys, the main influencers of fatigue life are grain size, interstitial contents, and degree of cold work. Grain size particularly can have a significant influence on the fatigue endurance of samples, as grain boundaries act as obstacles in crack propagation. Decreasing grain size from 110 to 6  $\mu\text{m}$  for instance can result in a fatigue endurance increase of 180 to 240 MPa for CP Ti. Furthermore, increasing oxygen and interstitial contents can lead to higher yield stresses in CP alpha Ti, which consequentially results in improved fatigue behaviour. Generally, in room-temperature applications, the ratio between the yield strength and fatigue endurance is constant despite these effects, though this ratio show temperature dependent behaviour [27].

The research produced by Bathini et al. [28] summarized the mechanisms governing fatigue, damage, and fracture of CP grade 2 Ti. Their works highlight that this material's elastic modulus may vary between 105-115 GPa, have a UTS between 344-561 MPa, and a percent elongation between 14.7-20 %, depending on rolling direction of produced parts. They found that the fatigue stress values of parts varied between 330 and 360 MPa at the  $10^6$  cycle life. They noted in their work that in the crack initiation and stable crack growth regions, fracture surfaces were flat and transgranular with fine microscopic and macroscopic cracks with regions of well-defined striations, showing microplasticity. Characteristically they found that the overload or fast fracture regions were covered by dimples of varying shape and size as well as had microscopic voids. They also noted that

the voids were likely local failure and that these would tend to grow during loading and eventually coalesce to form macroscopic cracks in the structure.

In the early works of Takao and Kusukawa [29], low-cycle fatigue behaviour of annealed CP Ti is presented under strain-controlled conditions. They summarize from their work that CP Ti exhibits neither fatigue softening or fatigue hardening, but that the material follows the Manson-Coffin rule. They observed that fatigue crack initiations occurred along grain boundaries in samples, summarizing that irreversible damage occurred in that region owed to slip constraint between grain boundaries.

In fatigue loading, existing features in samples such as voids, notches, scratches, inclusions and other irregularities, can act as stress concentrators and can lead to crack initiation as well as accelerate fatigue failure. These are known as stress concentration factors and are usually considered in design, described by the stress concentration factor  $K_t$ . While it is theoretically possible to manufacture a sample with an ideal fatigue stress concentration factor of  $K_t = 1$ , that of an unnotched specimen, due to clamping at the ends of fatigue specimens during testing stress-concentrators at the ends cannot be avoided, only reduced through design. It is also near-impossible to perfectly remove all irregularities present in the surface of a sample. Thus typically the sample surface has a tendency to carry slightly higher stress than nominal and surface roughness can influence the fatigue behavior of samples [30].

## 2.5 Shot-peening of Titanium Alloys

### 2.5.1 Shot-peening Treatment

Shot-peening is an effective and commonly used surface treatment which involves a surface being impacted by high velocity shots, typically being round metal or ceramic particles. Shot-peening is a type of cold working process which raises the dislocation density of the surface layer that is treated, resulting in inhomogeneous plastic deformation, a rougher surface finish, and induction of residual stresses in the subsurface [31]–[33]. As illustrated in the schematic featured in Fig. 2.3 from the works of Petit-Renaud [34], shot-peening a surface introduces high amounts of compressive residual stress at or just below the shot-peened surface, which is balanced by smaller amounts of tensile stress below this compressive stress layer. The process is a cost-effective and time saving method to result in improved fatigue properties. For some applications, the rougher surface finish obtained from shot-peening can be beneficial, such as for the fabrication of Ti orthopedic parts, which can help improve the adhesion strength of hydroxyapatite coatings and improve osseointegration behaviour [35].

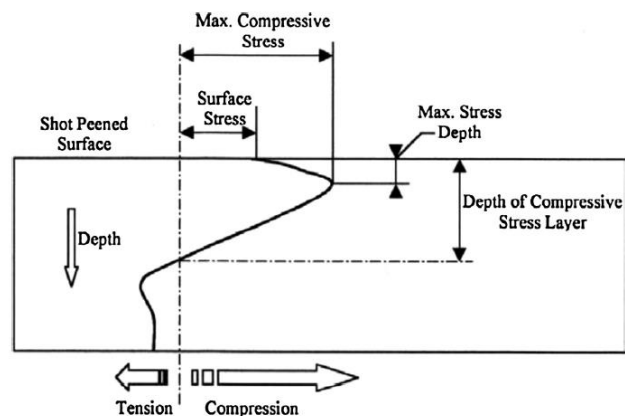


**Fig. 2.3.** Influence of shot-peening surface treatment [34]

As shown in the works produced by Ganesh et al. in [35] & [36], where Ti-6Al-4V and Ti-6Al-7Nb were subjected to shot-peening treatments at pressures of 3.5 and 4.5 bar for 60 seconds for 100% coverage, the introduction of compressive stresses led to increased surface hardness in both Ti alloys. In their tensile testing for the Ti-6Al-4V and Ti-6Al-7Nb, shot-peening treatments led to improvements in ultimate tensile strength (UTS) of up to 15% in comparison to untreated alloys. Of the two treatment pressures, the higher shot-peened pressure intensity of 4.5 bar was found to lead to greater UTS in comparison to while the 3.5 bar treatment. They speculate in their work that increasing shot-peening intensities can lead to better tensile and thus mechanical properties. In contrast, in the work of Wagner and Luetjering [33] using shot-peening on Ti-6Al-4V, they found shot-peening could have a negative influence on tensile behaviour as well. They highlight a decreasing yield stress behaviour with increasing shot-peening pressure can be obtained, explained due to the increased tensile residual stresses of samples with increasing peening pressure.

### **2.5.2 Shot-peening Influence on Tribological Behaviour of Titanium Alloys**

From the famous work of Archard [37] in regards to how materials behave in rubbing contact or sliding wear scenarios, volumetric wear is inversely proportional to the hardness of material, as shown in Archard's derived equation as follows:

$$v = \frac{kPd}{H} \quad (1)$$

Where  $v$  is the total wear volume,  $P$  is the applied normal load,  $d$  is the total sliding distance,  $H$  is the hardness of the material and  $k$  is the wear coefficient. Having discussed how shot-peening increases the hardness of treated surfaces, consequentially from



Archard's equation, it would be esteemed that shot-peening would result in improved wear resistance of Ti materials.

As previously mentioned, in the works of Ganesh et al. in [35] & [36], Ti-6Al-4V and Ti-6Al-7Nb subjected to shotpeening treatments at pressures of 4.5 and 3.5 bar exhibited increased surface hardness due to induced residual compressive stress. By consequence to this treatment, in their work they found that these samples experienced showed improved wear resistance, despite higher surface roughness induced in these samples.

In the works produced by Unal et al. [38], the mechanical behaviour of severe shot-peened CP Grade 2 Ti was studied at different intensities and time exposures. They found that nano hardness of the surface was increased to a maximum 9.5 GPa and grains were reduced to a size within the 25-30 nm range in their testing, and that locally the reduced modulus from nano indentation testing was found to increase up to approximate 265 GPa at the surface and then decrease and stabilize at approximately 120 GPa past a depth of 80  $\mu\text{m}$ . In other works produced by the same group where Unal is featured as the first author in [39], studied CP Ti grade 2 samples that were subjected to shot-peening treatment underwent free ball micro-abrasion wear testing and had significantly decreased volumetric wear values compared to untreated samples, highlighting positive wear influence on samples.

In the works of Yang et al. [40], they studied the fretting wear behaviour of Ti-6Al-4V on as-received untreated and shot-peened samples Ti-6Al-4V, using a cylinder-on-flat test set-up at the applied load of 100N and frequency of 10 Hz for varying time periods.

They found that with increasing shot-peening intensity, both the surface roughness and hardness of their samples increased. One key observation made in their testing scheme was that in early fretting wear periods below 75 minutes, shot-peened samples showed higher material loss than untreated samples. However, they noted that past 75 minutes, for long-term applications the shot-peened samples had lower mass loss values than untreated samples and improved fretting wear behaviour. They noted that in early fretting, dominant wear mechanisms present included adhesion and asperity peeling, while for longer duration fretting scenarios surface delamination was further observed paired with severe plastic deformation.

### **2.5.3 Shot-peening Influence on Fatigue Behaviour of Titanium Alloys**

The surface treatment of titanium parts through shot-peening is known to have a strong influence on fatigue life and commonly used in practice for manufactured aerospace components. In the works of Wagner and Luetjering from the first international conference on shot-peening in [33], they highlight key details to consider in regards to fatigue testing shot-peened titanium samples and elaborate characteristic behaviour of samples of this nature. In their fundamental work, they investigated the effect of shot-peening on the change in surface properties and their influence on the fatigue behaviour of titanium alloys in standard room conditions, vacuum and aggressive environments. They identified that three major influences of fatigue of shot-peened samples included: residual stress, dislocation density, and surface roughness. While shot-peening introduces compressive residual stresses into samples, they found that the residual stresses could either increase or decrease the fatigue life, dependent on the residual stress stability which depends on material cyclic hardening or softening behaviour. They noted with longer shot-peening

times, past 4 minutes, dislocation density remained nearly unchanged, however, found that a reduction in material strength occurred shown through microhardness decrease.

In Wagner and Luetjering's study [33], fatigue behaviour was shown to improve significantly from shot-peening, as shown in Fig. 2.4 from their work in comparing curves A & B, where curve A was shot-peened and curve B was stressed relieved but still possessed similar dislocation densities. Furthermore, in Fig. 2.4, they highlight the difference that adding a step of electropolishing to remove 20  $\mu\text{m}$  to A & B, shown with curves C & D, with curve C that is shot-peened and polished showing the best fatigue results. They noted that the high dislocation density obtained from shot-peening delayed crack nucleation and propagation, whereas an increasing surface roughness had the opposite effect as cracks could form more easily at lower stress amplitudes. In a separate testing case conducted, they further showed that better results are achieved with mechanical polishing over electrolytic polishing, though highlight that the improvement results depends on grain size.

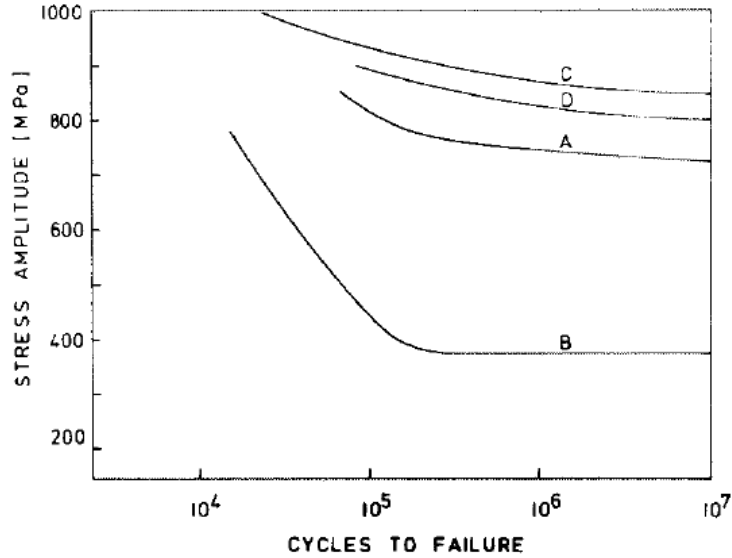


**Fig. 2.4.** Room temp, in air rotating beam fatigue results from Wagner and Luetjering, highlighting S-N curves of rounded Ti-6Al-4V samples with loading axis parallel to rolling direction (done prior to testing at 800°C) for conditions: A: Shot-peened, B: A + annealed 1h 500 °C in vacuum, C: A + 20µm surface removal, D: B + 20µm surface removal [33].

As described in the works of Burck et al. in [41], shot-peening is a fatigue process to the surface layer of fatigue samples, where the peening pressure is the stress amplitude applied and the exposure time is the number of cycles. They highlight in their work that the residual stresses in surface layers is directly associated with improved fatigue performance.

## 2.6 TiB Particle Reinforcement in Titanium Alloys

Titanium matrix composites (TMCs) are materials which feature a titanium matrix with continuous or discontinuous reinforcing fibers. These reinforcement fibers are generally considered for improvement in overall strength, wear, and hardness, with a related consequential degree of ductility loss. This concept was first applied to titanium alloys over 30 years ago with boron reinforcement [3], though since then other typical reinforcement composites explored, both with continuous and discontinuous fibers, in the

literature include TiB, TiB<sub>2</sub>, B<sub>4</sub>C, SiC, TiC, Ti<sub>5</sub>Si<sub>3</sub>, CrB, Co<sub>4</sub>2, CrB, Al<sub>2</sub>O<sub>3</sub>, and more [3], [9], [42]–[47].

In Ti alloys, TiB acts as a stiffener/strengthening additive, leading to increases in strength, hardening and consequentially wear improvement, with decreased elongation, exhibited with only small concentration additions [7]–[9], [48]. With less than 2 wt%, titanium-boron alloys are considered as modified, while with more than 2 wt% boron generally more improvement in strength is exhibited but detrimental effects on ductility with increasing concentration is noted [49]. While there are many different reinforcements for titanium alloys, TiB is usually a popular choice for its similar density to titanium (Ti 4.51g/cm<sup>3</sup> vs TiB 4.54g/cm<sup>3</sup>) as well as similar coefficients of thermal expansion [9]. Also, for cost-effective and ease of fabrication discontinuous reinforcement, TiB is often preferred as it has a smooth interface within a Ti matrix, leading to minimal residual stress and lattice strain. This is related to the crystallographic interface of TiB particles with the Ti matrix, which have excellent crystallographic compatibility because of the hexagonal TiB and Ti matrix with the TiB having sharp interface features [7], [8]. TiB is also known to restrict grain growth and act as a stabilizer of fine-grained microstructure [8], [43], [45], [48].

Shown in the work of Dubey et al. [50], varying low amounts of added boron (0-8 wt% boron) has very limited influence on the microstructure of various Ti alloys. However, they did find that the size of TiB particles formed in situ depended strongly on boron content, how the boron is incorporated into the structure, and processing temperatures. Moreover, they found that sample strength and ductility of samples strongly depended on

TiB particle geometry, finding that coarser TiB particles had lower strength and greater ductility in comparison to finer TiB reinforced structures.

TiB additions have further been found to improve creep resistance [51] and increase the modulus of elasticity of a Ti matrix [45], [48], [52]. In the works of Soboyejo et al. [53], they showed that TiB additions could increase the modulus of elasticity between 5-20% without showing significant loss of ductility. However, many researchers [7], [54], [55] have found that there is a tendency for TiB whisker clusters and large agglomerations to form in localized areas, which may impact mechanical properties of samples and act as stress concentrators as well as crack nucleation sites. Tabrizi et al. [54] found clusters of TiB formed at in-situ nucleation sites, which they highlighted was formed likely due to inhomogeneous dispersion of B<sub>4</sub>C additives, the precursor component used to form TiB and TiC in the Ti-6Al-4V composite material studied.

Processes involving in-situ TiB reinforcement have recently been explored in various newer manufacturing applications in an attempt to ensure a homogenous distribution of these particles, avoiding cluster nucleation and embrittlement [45]. Literature explored have shown recent research endeavors as a reinforcement agent in powder metallurgy (PM) processes such as plasma pulse sintering [47], selective laser/plasma surface alloying [56]–[60] plasma spark sintering [54], [61], [62], hot isostatic pressing [9], and other processing methods involving *in-situ* formation of TiB [7], [42], [44], [46], [49], [51], [55], [63]–[66]. Even more recently are novel research endeavors involving additive manufacturing (AM) in either the full build or surface treatment applications with TiB reinforcements through both powder bed fusion and directed energy deposition processes. Available literature involving this type of reinforcement through AM

is somewhat limited, showcasing AM techniques such as powder bed fusion and directed energy deposition, for example given laser cladding [43], [67], selective or direct laser metal deposition [8], [45], [68], as well as laser powder forming such as laser engineered net shaping (LENS<sup>®</sup>) [69]. However, no known research showcasing TiB reinforcement in a process such as plasma transferred arc solid free form fabrication (PTA-SFFF) could be found as that studied in this research.

As shown in the boron-titanium binary phase diagram in Fig. 2.5 boron has very limited solubility in both the  $\alpha$  &  $\beta$  phases of titanium (less than 0.02 wt%), with three stable phases exist with increasing weight percentage of titanium:  $Ti_3B_4$ ,  $TiB_2$ , and  $TiB$ , and two eutectic reactions. Boron is observed to have a somewhat neutral effect on the beta transus, acting as neither an alpha or beta stabilizer [3], [70]. The potential of  $TiB_2$  and  $Ti_3B_4$  could form in the reactions described, however the formation of  $Ti_3B_4$  is usually ruled out as with limited boron alloyed in these reinforcement processes. Shufeng et al. [7] explain that  $TiB_2$  is also less likely to form due to a larger negative Gibbs free energy in its formation versus the formation of  $TiB$ . They further validated this after producing  $TiB$  reinforcements formed through powder metallurgy combined with hot extrusion. This is also in agreement to the boron-titanium phase diagram (Fig. 2.5) as  $TiB$  is the more stable compound than  $TiB_2$  phase when excess moles of titanium are present.

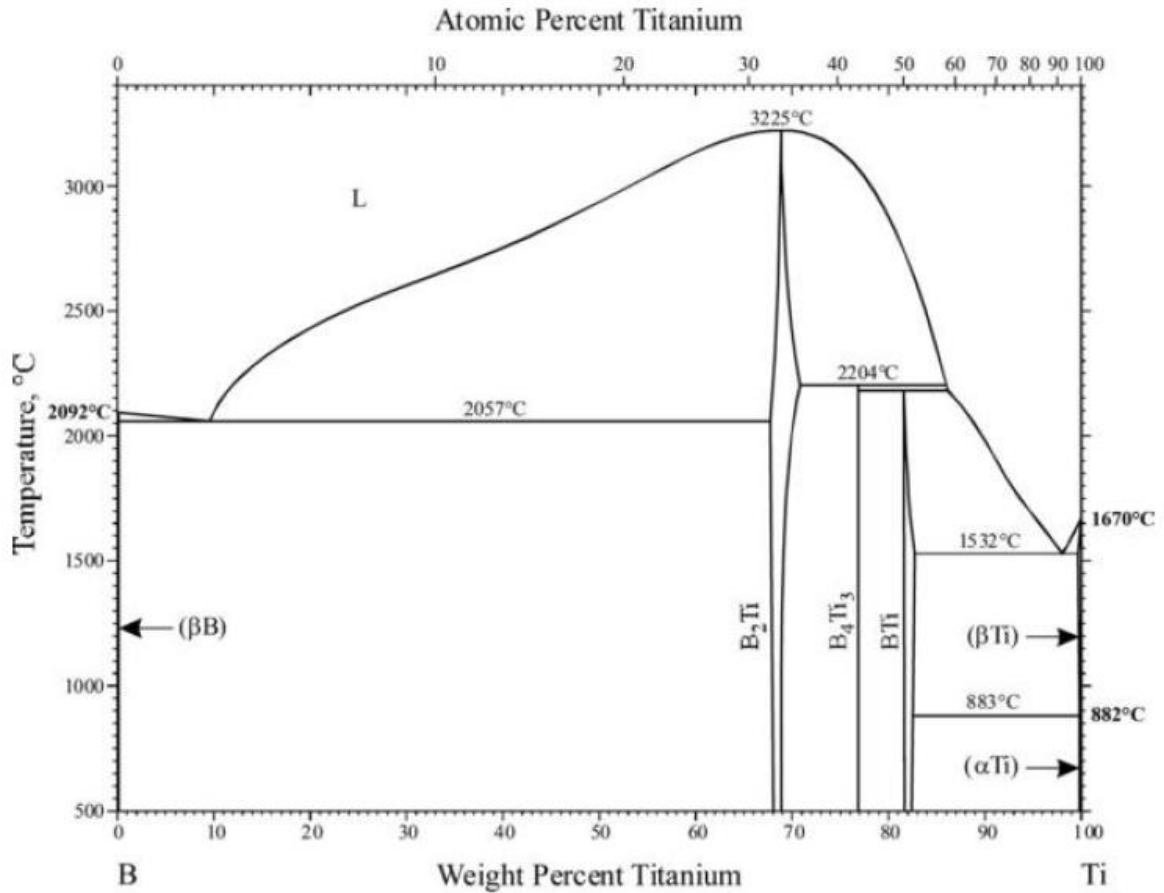


Fig. 2.5. Boron-titanium equilibrium phase diagram [70]

### 2.6.1 Morphology and Crystallography of TiB

Different TiB crystals can be formed in dependent on the natural of formation, generally occurring as single crystals in a structure from the literature. Kooi et al. [67] developed a fundamental paper covering the evolution of microstructure in a laser clad TiB-Ti composite coating, where the properties of TiB is covered in detail for laser-cladded treated Ti64 samples. Two main types of TiB were identified, composed of stable B27 and metastable B<sub>f</sub> crystal structures. These two crystal types were found to intermix closely due to crystallographic compatibility of the B27(200) plane fitting well on the B<sub>f</sub>(110) or ( $\bar{1}\bar{1}0$ )



planes (with B27[010]/ B<sub>f</sub>[001]) that caused stacking disorder. Three occurring morphology types of TiB identified to have appeared in the microstructure were: fine needles, plates, and course needles which have a tendency of being hollow or with titanium cores. Intermediate morphologies between these three are also seen. Noteworthy, extensive stacking faults are observed in this research for the fine needle structure, while the coarse needles consist of mostly defect-free B27 TiB. Similar work was done by Sahay et al. [65] before Kooi.

Ma et al. [44] overviewed the mechanical behavior dependence on the TiB whisker realignment from hot working studying a TiB ceramic reinforced Ti-1100 matrix (Ti-6Al-2.75Sn-4Zr-0.4Mo-0.45Si, in wt%). The resulted manufactured samples, which went through extensive homogenization through melting stages and finally hot working, featured the growth of needle-line TiB whiskers with hexagonal transverse section grown along the [010] plane due to the B27 crystal structure. Usually, anisotropic growth along the [010] direction is a dominate growth direction within a Ti matrix, with a hexagonal cross-section between the (100), (101) and (10 $\bar{1}$ ) planes. A high density of stacking faults has been experimentally observed on the (100) plane with a lower fault spacing in single atomic layers leading to interfaces between B27 and B<sub>f</sub> of TiB found in their work, as similarly described by Kooi et al. [67].

Shufeng et al. [7] briefly presented a similar orientation relationship of TiB and  $\alpha$ -Ti as [7]:

$$(100)_{TiB} \parallel (0001)_{\alpha-Ti} ; [010]_{TiB} \parallel [11\bar{2}0]_{\alpha-Ti}$$

With the  $[010]_{TiB}$  direction parallel to the axis of the whiskers, being the direction of the highest one-way diffusion and thus the direction whisker growth.

Nandwana [63] covered the topic of titanium boride formation and its subsequent influence on morphology and crystallography of alpha precipitates in titanium alloys extensively in their doctoral dissertation at the University of North Texas in 2013. One significant conclusion that Nandwana made was regarding the related morphology of  $\alpha$  structures in modifying the morphology of the  $\alpha$ -Ti structure, described as a complex crystallographic relationship dependent on alloying agents. The research concluded that limited boron additions lead to the development of lath or equiaxed  $\alpha$  structure around TiB particles depending on the crystallography, in Ti-Al-Mo type alloys, e.g. Ti-5Al-10Mo and Ti-5Al-5Mo-5V-3Cr-0.5Fe. In comparison, Nandwana noted that for Ti-V and Ti-V-Al alloy types, boron alloying led to a more overall change in morphology, resulting in a lath structure with aspect ratios not depending on the proximity to TiB particles. While the exact mechanism was unclear in the research, it is suspected to be possibly from the interaction of the present boron additive and other alloying elements.

Pouzet et al. [45] looked closely at the microstructures found through direct metal deposition laser processing. They found that with a wt% of approximately 1.5% of  $B_4C$ , shorter TiB tended to form seeming to be located at former  $\beta$ -Ti grain boundaries, while increasing the wt% to 3%, the needles seemed to have crystallized in former  $\beta$ -Ti grains leading to longer whiskers.

### 2.6.2 TiB Influence on Tribological Behaviour of Titanium Alloys

Both Attar et al. [68] and Cai et al. [9] in their work highlight that little to no research has been done focusing on the investigation of surface properties of Ti alloy composites with Ti boride network structure such as hardness, friction, and wear properties, which highlights further the need to characterize the tribological and material properties of samples of this nature, as conducted in this work.

In the works of Attar et al. [68], CP Ti as well as Ti with 1.5 wt% of boron materials were produced using additive manufacturing through selective laser melting (SLM). He evaluated their nano hardness using a standard Berkovich pyramidal-indenter, employing the Oliver and Pharr analysis method, and summarised that the CP Ti SLM samples had a nano hardness of 2.95 GPa while the Ti-TiB material drastically improved with a hardness of 4.49 GPa. From wear testing, he highlights in his results that ploughing grooves and delamination is observed in both samples during wear testing, however that in the Ti-TiB composite material reduced amounts of delamination, experienced less severe wear scars, and had lower wear rates found with TiB additions.

In the works produced by Cai et al. [9], Ti-6Al-4V composites were produced using hot isostatic pressing (HIP) with low amounts of TiB, formed through the addition of between 0-8 wt% of TiB<sub>2</sub>. In their work, they highlighted that the micro-hardness of the material increased with increasing amounts of TiB and nano hardness measurements showed that the TiB network structure had a higher nano hardness than the surrounding matrix. The 8 wt% added TiB<sub>2</sub> sample had double the value of micro hardness of the TiB-free sample tested, which is attributed to the hardening effect of the harder TiB particles as

well as grain refinement in the microstructure experience with these additions. Moreover, from wear testing using  $\text{Si}_3\text{N}_4$  ceramic balls, they found that the COF as well as wear mass loss measurements decreased with increasing additions of  $\text{TiB}_2$  in produced materials. The COF was observed to become much more stable with increasing  $\text{TiB}_2$  additions and a decrease of 33.8% of average COF was observed with the 8 wt% added  $\text{TiB}_2$  sample compared to the TiB-free sample tested. Main wearing mechanisms identified from wear scar analysis showed mild to severe plastic deformation, oxidation wear, as well as adhesion wear with Ti material transfer to the ceramic balls but no  $\text{Si}_3\text{N}_4$  identified on the wear tracks.

Popoola et al. [8] looked at microhardness and wear resistance of Ti-6Al-4V-TiB composite coatings deposited through laser metal deposition on a Ti-6Al-4V substrate using the additions of Ti-6Al-4V with varying amounts between 5-20 vol.% of  $\text{TiB}_2$ . They summarised finding a metal-matrix composite with improved properties with the final structure containing TiB, with an optimal increase of micro-hardness of 33% with this treatment, with samples that had 15 and 20 wt.% of TiB with 10 and 20 layers of coatings. With this, they found that the increase of  $\text{TiB}_2$  additions lead to wear improvement with the formation of TiB. They also found a higher amount of energy is absorbed in samples containing more TiB, which is attributed to its finer grain structure. TiB is known to interferes with nucleation growth and promotes a finer grain structure. Miklaszewski et al. [58] also found evidence of increased microhardness with their microplasma surface alloying of titanium testing with TiB while Pouzet et al. [45] also noted the nucleation of TiB in Ti whiskers through direct metal deposition which lead to substantial grain refinement and increase in hardness.

In the paper written by Prakash et al. [71], the wear performance at different loading and speed configurations as well as microstructure and hardness were evaluated for a vacuum sintered Ti-6Al-4V with B<sub>4</sub>C additions, the precursor addition used to form TiB and TiC during powder metallurgy processing. They noted higher micro hardness values achieved with increased B<sub>4</sub>C precursor content up to 10 vol%. Abrasion and delamination were identified as the main wearing mechanism in this study. The presence of crushed debris was indicative of delamination occurring in this study, with delamination occurring in severe wearing with microcracks which were also noted. Abrasion wear is noted in instances of mild wear, with shallow grooves and scratches parallel to the sliding direction indicating this.

Similarly, in the works of I.Y. Kim et al. [72], they studied the wear characteristics of a CP Ti Grade 2 alloy with increasing additions of the precursor B<sub>4</sub>C. They performed wear tests using ball-on-disk analysis with an applied load of 0.35 N and sliding speed of 120 rpm (125mm/s) for 30 mins under unlubricated conditions. Their research highlighted samples alloyed with higher amounts of B<sub>4</sub>C showed increase in hardness and wear resistance of the metals. The highest alloyed sample type, with 3.46 wt% B<sub>4</sub>C, had a wear resistance that was about four times higher than that of the CP Ti Grade 2 alloy looking to be improved. They found that the wear debris consisted primarily of fine particles pulled from the TMCs and counterface ball specimens, consisting of a mix of the titanium matrix, reinforcement particles, and oxidation. They conclude that abrasion, adhesion, and oxidation wear formed this debris and a transfer layer on the counterface balls, with abrasion wear acting as the dominant wear mechanism. Plastic deformation is also additionally noted to have occurred in their CP titanium sample. While cracks were

observed in their CP Ti samples, no craters formed by crack propagation were observed in their reinforced structures, which suggests that the 2<sup>nd</sup> phase particles helped in preventing crack propagation. In the papers written by the same group where Choi appears and J.S. Kim as the first author, similar analysis on the microstructure and friction/wear behavior of (TiB + TiC) particulate-reinforced TMCs is presented in greater volume and is more thoroughly documented in papers referenced as [73]–[75].

### **2.6.3 TiB Influence on Fatigue Behaviour of Titanium Alloys**

Limited literature is available which discusses the fatigue behaviour of near CP Ti-TiB materials, with no literature found for AM materials of this nature produced from the PTA-SFFF process studied in this research group.

From the works of Dubey et al. [50] in studying the fatigue failure of various Ti alloys containing low amounts of boron (0-0.8 wt% boron), TiB particle whiskers were found to crack during testing. They describe that they tended to debond or fracture within the plastic zone before significant bridging occurred in samples, though also showed that in some alloys the TiB particles appeared to be embrittled from fractography observations. They also describe a key shielding effect that uncracked TiB particles were observed to have which they make a claim to have led to slower fatigue crack growth rates in samples. They also found in some instances, fractured TiB whiskers tended to cause the nucleation of microcracks which propagated into larger, secondary cracks within samples. Their study summarizes and claims that increasing amounts of boron past an optimal 0.6 wt% can have negative impacts on fatigue, though at 0.6 wt% boron samples had the best fatigue performance and below this threshold fatigue improvements were observed.

Saito et al. [76] report in their work investigating the thermomechanical properties of PM beta titanium metal matrix TiB composites that tensile strength, fatigue strength, and wear resistance had been found to increase with added 10 wt% & 20 wt% TiB volume fraction for Ti-6Al-4V and in Ti-6.8Mo-4.2Ge-1.4Al-1.4V.

In comparison, Shufeng Li et al. [7] found that additions of TiC and TiB particles in a PM and hot extrusion pure Ti matrix had synergistic beneficial strengthening influence on the TMC. They found that increasing additions of TiC and TiB with a 13.6 theoretical vol% led to increasing UTS of 654 MPa to 1138 MPa, but decreased elongation from 32.4% to 2.6%, highlighting increased brittleness with more additions. Moreover, in their work they found that no TiB particle pull-out was noted in their fractography observations, which highlights the strong interfacial bond between Ti-TiB. Shufeng et al. also discussed that due to the intrinsic stiff and large aspect ratio of longer TiB whiskers, up to 100 nm in width and 5  $\mu\text{m}$  in length, the TiB particles can act as stress concentrators by obstructing the migration of matrix grains during plastic deformation. This leads to the formation of voids at Ti-TiB interfaces and eventually rupture of the particles. They note that the TiB whisker segments would retain their interfacial bond to the Ti matrix and still act as reinforcement agents within the composite, which is suggested based on the three-stage tensile mechanical behaviour observed in their testing.

In the early works of Emura et al. [77] with Ti-22Al-27Nb, finely distributed TiB particles of similar sizes of those studied in this research were added to samples, which ranged from up to 1  $\mu\text{m}$  in width and 5  $\mu\text{m}$  in length. They found that these fine TiB reinforcements improved fatigue strength and obstructed dislocation movement. Overall, they summarized that while coarser TiB particles would have the classically observed

composite strengthening effects, finer TiB particles also exhibited other influences such as grain refinement and dislocation movement blocking.

In later works produced by Dubey et al. [78], they investigated the fatigue crack growth of in-situ formed TiB in Ti-6Al-4V-0.5B. Their samples made from a more traditional ingot powder metallurgy procedure produced longer TiB needles of 7 to 23  $\mu\text{m}$  in length and widths of 1 to 1.3  $\mu\text{m}$ . They identified that elastic bridging by TiB reinforcements occurred, with instances of debonding along with the bridging TiB whisker/matrix interface, though noted that crack bridging did not appear to have a strong influence on fatigue crack growth resistance. They also found that TiB whiskers did not undergo plastic deformation in the matrix, observed from lack of dislocations in the whiskers through TEM. However, in contrast Majumdar et al. [79] found with 0.5 wt% boron added to a beta Ti-35Nb-5.7Ta-7.2Zr alloy, which formed in-situ TiB particles, they found that the particles in the matrix led to no substantial effect on yield strength and fatigue strength.

Gorsse and Miracle in their work [80] with discontinuously reinforced Ti-6Al-4V with TiB, produced through PM route then sealed through hot isostatic pressing (HIP), found that the 10% and 20% composites exhibited poor ductility and only moderate strength improvements relative to the unreinforced matrix, which influenced the mechanical properties of samples. Observations made highlighted that damage of large-sized or clustered whiskers occurred at low strain levels and altered the deformation properties of the composites, leading to premature cracking at TiB aggregates. Moreover, they observed that crack propagation through TiB whiskers appears to be easier parallel rather than transverse to the whisker axis, increasing premature damage during testing.



They propose that modified powder processing and thermomechanical treatments should be implemented to eliminate TiB clusters and reducing the size of TiB whiskers to lead to improved strength and ductility of discontinuously reinforced Ti.

## **2.7 Additive Manufacturing Fundamentals**

Additive manufacturing (AM), commonly referred to as 3D printing, digital or layered manufacturing, or rapid prototyping, is defined by the ASTM International Committee F42 on AM as the “...process of joining materials to make objects from 3D model data, usually layer by layer, as opposed to subtractive manufacturing methodologies [81].” The F42 committee, formed in 2009, focuses on the promotion of knowledge, stimulation of research and implementation of technology through the development of standards for additive manufacturing technologies, and is the main body within ASTM to develop standards for this process. For grouping current and future AM technologies, the F42 committee has separated AM processes into seven key process categories [81].

For metal-based additive manufacturing specifically, Fig. 2.6 summarizes the four commonly used processes and sub-processes of the AM family used to build parts. In this research work, the PTA-SFFF would be considered a powder directed energy deposition (DED) AM process technology, which is discussed in greater detail in the following section.

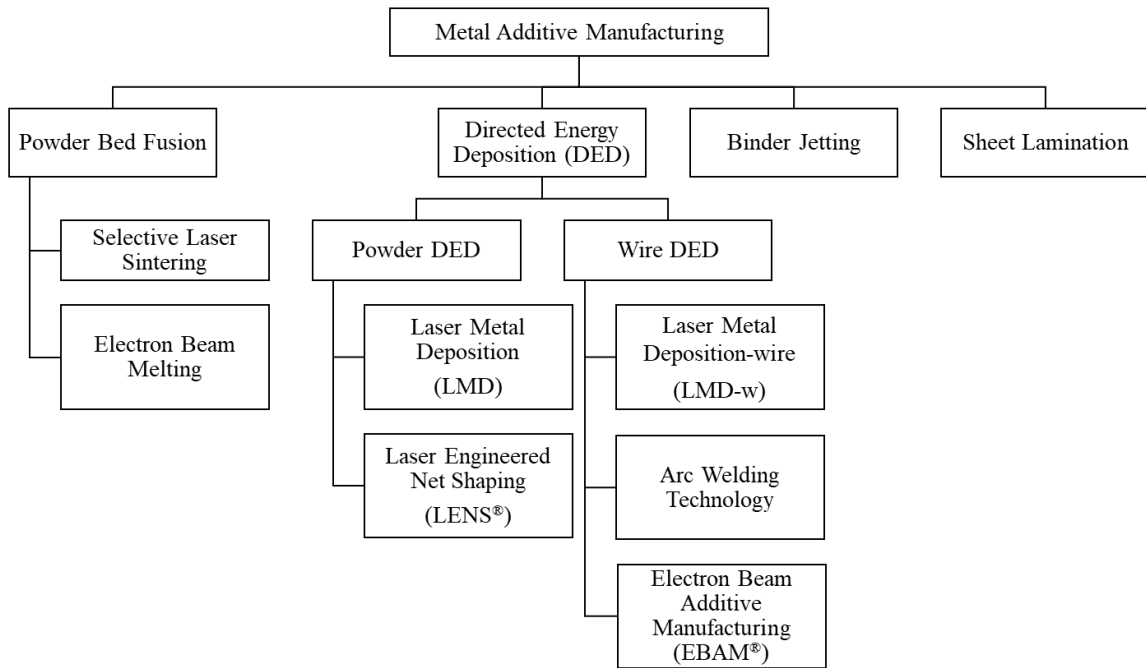


**Fig. 2.6.** Common metal additive manufacturing methods. Chart created based on information found in Ref. [82]

In most AM processes, 3D computer-aided design (CAD) models are separated into 2D slices for fabrication, where within each of these cross-sections material is laid in a certain pattern referred to as the tool path. Figure 2.7 shows the general process flow to build metal AM DED parts, where a 3D model is typically converted to a stereolithography or ‘.stl’ file format for easier manipulation in the processing stage when build parameters are configured. Then typically a part would be built once the user is satisfied with their build parameters and then, depending on the process, post-processing may be required for example to remove support material or to smoothen a rough surface finish. AM options have a diverse set of applications, from automotive part builds to aerospace repair, surface treatment options, biomedical customized implants, etc.

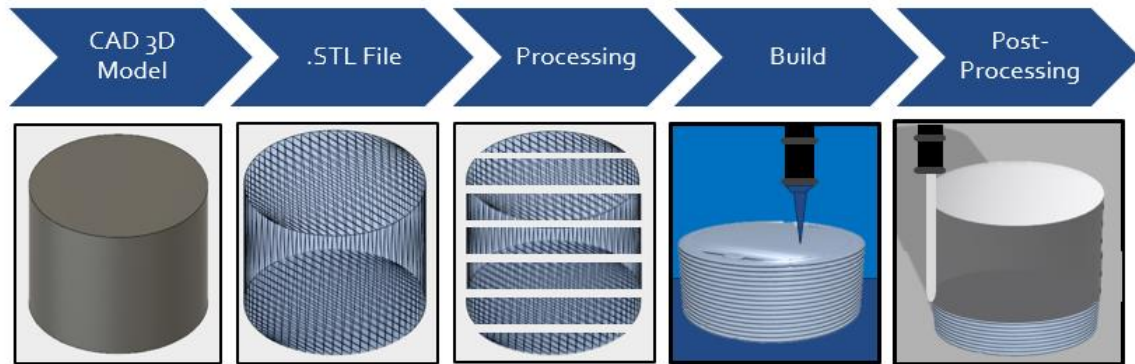


**Fig. 2.7.** AM general process flow used to build metal parts through DED

While past the novelty stage of development, metal-based AM is far from being understood at the materials science level, though offers particular advantages for manufacturing parts such as product customizability, near net-shape product capabilities, complex geometry fabrication, fast production on the smaller manufacturing scale, and more [83]–[85].

Considering AM from a materials engineering point of view, there are still many presentable challenges related to using AM processes to build service parts. Unique microstructures are obtained using AM processes, which remain somewhat far from being understood at a materials-by-design standpoint of view. The dependency of microstructures relies heavily on process control in production and can change depending on factors such as bead sized, overlap, process-dependent heat source intensity, as well as other parameters. For most AM processes, users also have a rigid choice of processing materials and often built parts require post-processing treatment for surface quality improvement [85], [86].

Moreover, there is no standard material characteristics database within the AM industry to provide mechanical properties fabricated by different AM processes to

designers, such as specifications of the mechanical properties of available materials and more detail on how parts made from these materials perform. While the ASTM F42 committee is making strides towards developing standards related to various AM processes and material processing, crucial development is still needed.

### **2.7.1 Titanium Additive Manufactured Parts Made Through Directed Energy Deposition**

In comparison to other AM processes which may be used to produce Ti parts, a benefit to DED based AM technologies, such as the PTA-SFFF process, is its ability to use multi-axis deposition as well as multi-material deposition e.g. multipowder hoppers. More commonly, DED processes are easily integrated or can be added into traditional subtractive manufacturing systems, which helps users in understanding how these processes work as well as may help decrease investment costs related to these systems [87]. As limited literature is available on the specific PTA-SFFF process, this subsection aims to summarize relevant literature to better understand the results obtained in this research works through materials testing, focusing on DED-based AM processes where Ti alloys are studied.

From the review paper of Dutta and Froes [88] on the AM of titanium alloys, when discussing the mechanical properties of AM Ti, they highlight that laser-based processes with Ti-6Al-4V they have higher UTS values but exhibit less ductility due to martensitic formation. While in comparison, arc-based and electron beam-based processes had better ductility. They note that using HIP-based post-treatment options, ductility can be improved, though generally as built Ti-6Al-4V products produced using AM options have been found to offer similar or improved fatigue resistance as compared to cast and wrought

materials. They also mention that DED-based processes are optimally used for repair processes and that repairs which have been done using direct metal deposition (DMD) and laser cladding have shown equal or improved mechanical properties.

Between the works produced by Clark et al. [89] studying laser melting of Ti-6Al-4V as well as the works Kobryn and Semiatin [90] with direct laser fabrication with Ti-6Al-4V, there is significant evidence that shows microstructurally there are anisotropic tendencies in AM Ti components. This is explained by the layer-by-layer build of AM parts, which introduces unique thermal histories throughout a part with cooling and reheating cycles as each new layer is added.

However, as pointed out in the works of Carroll et al. [91], minimal research has been conducted to understand how the microstructural properties influence the macroscopic mechanical properties such as tensile strength. In the works of Carroll et al., they studied the anisotropic behaviour of Ti-6Al-4V using a laser-based, argon-purged build cell DED process. Performing tensile testing in the longitudinal and lateral directions, they found that the UTS matched approximately that of 1060 MPa in both directions. The samples experienced enhanced ductility due to the lack of pores present, with a density of 99.99%, and had similar properties of wrought Ti-6Al-4V, however the percent elongation experienced in samples differed from 11% in the longitudinal direction versus 14% in the lateral. They explain that this is likely due to the columnar prior- $\beta$  grain morphology and the presence of alpha grain boundaries, which is a preferential path for fracture. They also experimented with the influence of oxygen impurities on the build, which is common in AM processes, and found that impurities of 0.0124 wt.% oxygen improved strength of the component and had negligible influence on ductility.

In considering the performance of AM parts, particularly fatigue performance, Chan et al. [92] highlight that AM density and build quality is a key influencer to mechanical success. In their comparison study evaluating electron beam melting (EBM) and laser beam melting (LBM) using Ti-6Al-4V compared to rolled and cast Ti-6Al-4V, they found that surface finish and build quality influenced results substantially. They summarized that the EBM in comparison to the LBM process created rougher surface finished parts with voids and partially melted powder regions, which served as stress concentrators leading to their worse fatigue. They found that both AM methods performed better when samples were EDM cut from larger blocks versus fabricated to exact test size. Ultimately, they found that the rolled Ti-6Al-4V performed the greatest, followed by LBM-EDM cut samples, LBM as fabricated samples, EBM-EDM samples, cast material, and then the EBM as fabricated samples. They also highlighted in their work that the maximum surface roughness of AM parts was related to the layer thickness parameters specified, where thinner layers led to smaller surface roughness values.

### **2.7.2 Applications of Additive Manufactured Titanium Parts**

As discussed previously in this literature review, a deterrent to using titanium remains its relative high cost to other materials, related to its poor manufacturability [2]–[5]. For this reason, titanium makes a worth-while material candidate to consider for AM applications for cost saving opportunities. The capabilities of neat-net shape production through AM processes for titanium parts offers opportunities for machining and part design lead time to reduce as well as offers more design freedom than conventional subtractive machining, which can lead to cost savings [93].

One of the current, most popular applications of titanium AM is for aerospace parts. Using AM to manufacture titanium parts has been proven through various case studies to reduce the “Buy-to-Fly” ratio, which is the ratio between the raw material used to manufacture a part versus the weight of the part actually being made [93]. For traditional titanium-based milled aerospace parts, the Fly-to-Buy ratio is very high, upwards to 40:1; leading companies to accept that the machining costs alone will be double that of the cost of the component itself and resulting in a substantial amount of wasted material to be reprocessed [88]. Moreover, AM is more cost-effective when used for smaller production runs, which is often required for aerospace parts, and offers quick lead times for manufacturing especially for parts such as air foils which intricate internal configurations [87].

One example of a successful application of Ti AM described in [94] is the production of GE’s AM fuel nozzles for the LEAP engine model. To fabricate over 30,000 of these fuel nozzles, GE uses over 40 AM printers which use Ti substrate powders to produce these parts. In older models, the original part was made from 20 separate pieces that were welded to create the whole nozzle piece, however now the part is produced as one piece using AM which requires no post welding assembly, leading to further cost savings in manufacturing and design. Moreover, the nozzle’s tip’s weight was able to be cut by approximately 25% because of this AM initiative. Another aerospace Ti AM example [87] is the production of a titanium bracket connector on board the Airbus A350 XWB by Concept Laser using their LaserCUSING system. Using AM to produce this bracket enabled designers to produce a more porous but structurally sound structure, which

reduced the bracket's weight by 30% and reduced development time by up to 75%, from 6 months to 1 month.

Another potential application of titanium AM is for the development of customizable, patient-specific biomedical implants, prosthetics, and devices, namely for orthopedic implants such as hip and knee replacements as well as dental implants. Titanium is popularly used in biomedical applications versus other alloys such as stainless steels, CoCr-alloys, CP niobium and tantalum, for its superior corrosion resistance, high strength-to-weight ratio, chemical stability, biocompatibility, bioadhesion or osseointegration/bone-growth properties, fatigue strength, good joining capability, and close modulus of elasticity to bone. Particularly its excellent corrosion resistance and biocompatibility make it an outstanding biomaterial candidate [95]–[98].

One example of an AM process being explored for biomedical applications from [99] is through Laser Engineered Net Shaping (LENS<sup>TM</sup>), a form of DED which uses laser and metal powders for fabrication. The process has been used to create Ti-6Al-4V samples with pore sizes of 0.89, 1.5, and 2.0 mm in width, which has been shown to help influence bone integration, cell response, and elastic moduli of samples. The precision of the induced porosity adds more control to the manufacturing process which facilitates osseointegration. Moreover, highlighted in the review made by Manivasagam et al. [97], laser-based AM processes involving titanium and the use of CO<sub>2</sub> have further resulted in higher corrosion resistant microstructures while laser nitriding with nitrogen and argon in presence also yielded higher corrosion results. Both the improvement of osseointegration and corrosion resistance of titanium would further benefit biomedical implants in application, helping prevent corrosion thus resulting in implant amelioration. Pilot studies such as the ones



conducted by Tedesco et al. [100] and Tunchel et al. [101] have shown clinical success in implementation of additive manufactured dental implants, highlighting bone growth and even formation in pores of the implants. However, more research is required to validate the usage of AM for implant usage to ensure their safe and long-term usage for human applications.

Last of all, as prices are driven down for the manufacturing of titanium parts using AM, titanium AM parts may be considered in other, more conventional applications, such as to replace traditional steel components in automotive applications for lightweighting opportunities. Other applications of AM for titanium could be for surface treatment options, to build conventional parts with enhanced properties, as well as for automotive and aerospace restoration and repair. One impactful international initiative is the Additive Manufacturing and Simulation (AMOS) project, which aims to address the issue of aging aircraft fleets and develop a number of suitable additive materials and processes specifically tailored towards the repair of aircraft parts [102].

## CHAPTER 3: MATERIALS AND EXPERIMENTAL METHODS

### 3.1 Material: Additive Manufactured Titanium Featuring TiB Reinforcement

This research explores the potential of a new proprietary AM method termed Plasma Transferred Arc Solid Free Form Fabrication (PTA-SFFF). As-received additive manufactured PTA-SFFF Ti blocks featuring TiB reinforcement were received for this study. Through prior work using Inductively Coupled Plasma Optical Emission Spectroscopy (ICP-OES), the PTA-SFFF sample elemental mass percent was found to be 97.3% Ti, 0.82% Al, 0.63% B, 0.37% Si, and 0.20% Fe [10].

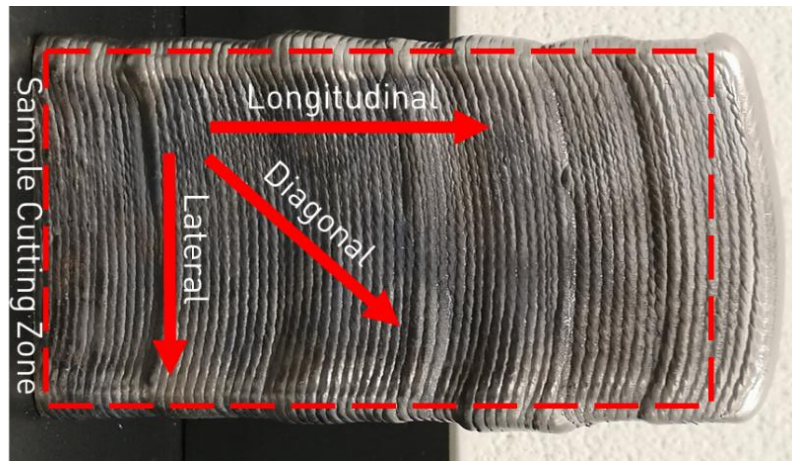


**Fig. 3.1.** PTA-SFFF Ti-TiB block highlighting directions considered during mechanical testing. Enclosed in the red dashed square (not to scale) highlights the approximate area in which samples were cut from using wire electrical discharge machining (EDM). This is to show that blocks were squared off to remove any scaling from the AM process and roughness on the outside surface, which may have an influence on testing.

Figure 3.1 highlights the longitudinal, diagonal, and lateral directions referred to in the following subsections during sample preparation. The enclosed region in the red dashed square of Fig. 3.1 shows the approximate area in which samples were cut from using wire electrical discharge machining (EDM). This is shown to highlight that these AM blocks were first squared off and cut within the center to blocks, with its outer casing removed, in

order to remove any scaling from the AM process and roughness on the outside surface, which could have an influence on testing as samples are prepared.

## **3.2 Metallography Characterization Methods**

### **3.2.1 Sample Preparation for Cross-Sectional Analysis**

In preparing all samples for microstructural review and testing, the ASM Handbook Volume 9: Metallography and Microstructures section ‘Metallography and Microstructures of Titanium and Its Alloys’ [17] was consulted heavily as a reliable, descriptive resource for developing preparation methods for samples. Two key schemes were used to prepare polished samples, depending on the nature of the samples purpose. Both schemes used a revolution speeds of 150 rpm throughout both grinding and polishing stages.

For mounted and un-mounted samples intended strictly for microstructural review, an incremental grit scheme going from 320P, 400P, and then 600P, was used to mechanically grind samples. Samples were then polished using a 9 µm poly-crystalline polishing solution and then polished with a diluted colloidal silica suspension until a mirror finish was achieved. In between every preparation stage, samples were rinsed with water and then cleaned with ethanol then dried to ensure no transfer of grinding particles from one stage to another. To ensure that residual colloidal silica polishing debris did not adhere to the surface, samples had to be rinsed with high pressure water for one minute, ultrasonically cleaned in ethanol, and then lightly polished again using a 1 µm mono-crystalline polishing solution as the final polishing step.

As colloidal silica is considered a chemical-mechanical polishing action final stage for sample preparation, prolonged exposure causing over-polishing can do damage to sample surfaces over long periods of time and may lead to corrosion. Thus, for samples where surface properties were of the utmost priority, such as for samples prepared for wear, fatigue, and hardness testing scenarios, samples were only treated to mechanically based grinding and polishing schemes as a precautionary measure to this. In such cases, typically samples were mechanically polished up using an incremental grit scheme going from 320P, 400P, 600P, 800P, and 1000P to grind samples. Following this, a 3  $\mu\text{m}$  mono-crystalline polish and then a 1  $\mu\text{m}$  poly-crystalline diamond polish was used until samples achieved mirror-finish quality. In between every preparation stage, samples were rinsed with water and then cleaned with ethanol then dried to ensure no transfer of grinding particles from one stage to another. For tensile and compression testing samples specifically, samples were only ground up until 600P, which was done simply to remove any impurities and oxide debris introduced through the wire EDM process.

To etch samples for microstructural review, ASTM E407 [103] was consulted paired along with the Volume 9 of the ASM Handbooks [17]. Kroll's reagent (192 per ASTM E407) was used to etch titanium throughout this work, prepared to the following concentrations: 50 mL of ultra-pure distilled water, 2 mL of nitric acid ( $\text{HNO}_3$ ), and 1 mL of hydrofluoric acid (HF).

While titanium itself is conductive enough to be viewed in scanning electron microscopy (SEM) with minimal charging issues, any mounted samples intended to be observed using SEM were gold sputter coated using the Quorum Q150R Plus Rotary Pumped Coater. This was done to improve surface conductivity as well as avoid charging

during imaging, as the cold epoxy mounting isolated the sample and reduced surface conductivity. Moreover, mounted Ti samples for SEM observations were wrapped at the sides and bottom with aluminum foil and copper tape was placed at the edge of the surface observed to the base of the SEM stand to act as a conduction line and ensure charging would not occur during SEM observation.

### **3.2.2 X-Ray Spectroscopy**

X-Ray Diffraction (XRD) analysis is a useful materials investigation technique which can be used to identify present crystalline structures, quantify phases present, and identify if any amorphous material is present in a sample. XRD patterns represent a sum of the diffraction patterns of all phases in the sample [104].

XRD analysis using the Proto AXRD General Purpose Powder Diffractometer was further employed in this study to confirm the presence of TiB in the structure with the target  $\text{CuK}\alpha$  radiation and target power 30 kV and current of 20 mA. Analysis from obtained XRD patterns was conducted with reference to works cited from the Inorganic Material Database known as AtomWork [104]. SEM paired with EDS analysis is utilized to confirm phase and microstructures present of the samples.

### **3.2.3 TiB Image Analysis**

The distribution of TiB particles was evaluated through particle analysis methods using the ImageJ software in both the longitudinal and lateral directions of the samples. To do this, three SEM micrographs of the same magnification (200X) showing the polished and etched typical TiB particle distribution observed were selected from different oriented samples.

Using the Image J software, a threshold value is adjusted in order to distinguish particles from the matrix while converting the image to a binary mask, i.e. a black and white image which features the particles of interest in black and the metal titanium matrix in white. To do this, the initial image must already be grayscale, if it is not, the image can be processed and converted to an 8-bit grayscale image within the program. Further processing to the image is accomplished to isolate and fill particles which were indistinguishable in the binary conversion. Using the 'Analyze Particles' function within ImageJ, with a selected particle area size range of 0.5-200  $\mu\text{m}$  to avoid smaller background features still featured in the micrograph after the binary conversion, a new micro image is created outlining the distinguishable particles. Figure 3.2 illustrates this process using a higher magnification image of 500X for demonstrative purposes.

A summary from this function also provides quantitative values from the particle analysis, including the area taken up by each particle, their height and width obtained through elliptical fitting, as well as other perimeters related to their characterization including their aspect ratio (AR). AR values are calculated based on the ratio of the particle's fitted ellipse by taking the maximum length dimension as the height and dividing that by its perpendicular width dimension [105]–[107].

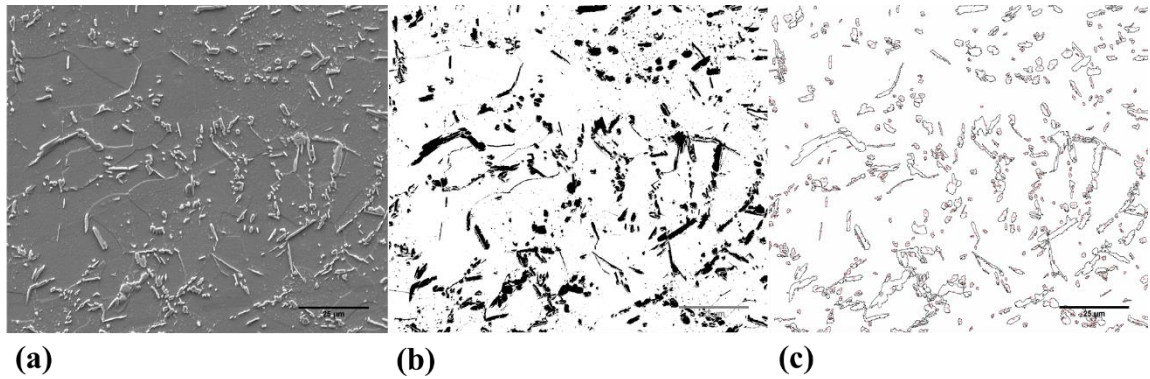


**Fig. 3.2.** (a) Secondary electron SEM image showing the typical cross-section microstructure of the PTA-SFFF Ti-TiB samples used in this investigation, etched in Kroll's etchant (500X). (b) Shows the same image, after processing through thresholding with the ImageJ software to isolate TiB particles (in black) from the Ti matrix (white). (c) Final processed image obtained after the 'Analyze Particles' function was employed using the ImageJ software. Contours show particles which are counted in the analysis and red dots appear in the image for every particle counted.

### 3.2.4 Focused Ion Beam and Transmission Electron Microscopy

Focused ion beam (FIB) and transmission electron microscopy (TEM) work was done at the Canadian Centre for Electron Microscopy (CCEM) in Hamilton. The images presented in Fig. 3.3 are featured to explain the procedure steps undertaken to prepare a sample for TEM observation through FIB milling. First an area of interest is selected for analysis, which for the TEM analysis conducted was the line shown in Fig. 3.3 (a). The sample area was chosen to intersect various TiB particles along their length while also intersecting some of these unidentified lighter phases present on the surface of the sample. Before beginning the FIB process to cut a TEM sample out, the interested area was first coated with carbon, shown in Fig. 3.3 (b), to protect its top surface during the FIB process. Then the section of interest was slowly milled out using FIB, working from the outside in to avoid damaging the selected area, as shown by Fig. 3.3 (c). Through a process referred to as the 'lift out' stage, the TEM sample was then micro-welded to the tip of a needle and milled at the bottom to be removed from the coupon, Fig. 3.3 (d), to be transferred to a

more appropriate stage for the rest of the sample preparation. After being transferred and mounted to a separate operation stage, shown in Fig. 3.3 (e), the sample area of interest for TEM observation was slowly reduced using FIB to create a very thin wafer-like section, Fig. 3.3 (f). This section was thinned until a light could be shone behind the sample and the light could be visibly observed to be shining through the thinned section, making it close to transparency and signalling that the sample could be observed using TEM. In TEM, the FIB milled section was able to be observed and line scans between the Ti and TiB interface were conducted to look at the coherency between the two phases. Moreover, in TEM electron energy loss spectroscopy (EELS) was employed to further confirm the presence of boron in the microstructure. High-resolution TEM (HR-TEM) was employed to observe the interface of the Ti-TiB and also used in selected area electron diffraction (SAED) patterning to identify and confirm crystal structures of Ti and TiB through interplanar distance or 'd-spacing' analysis.



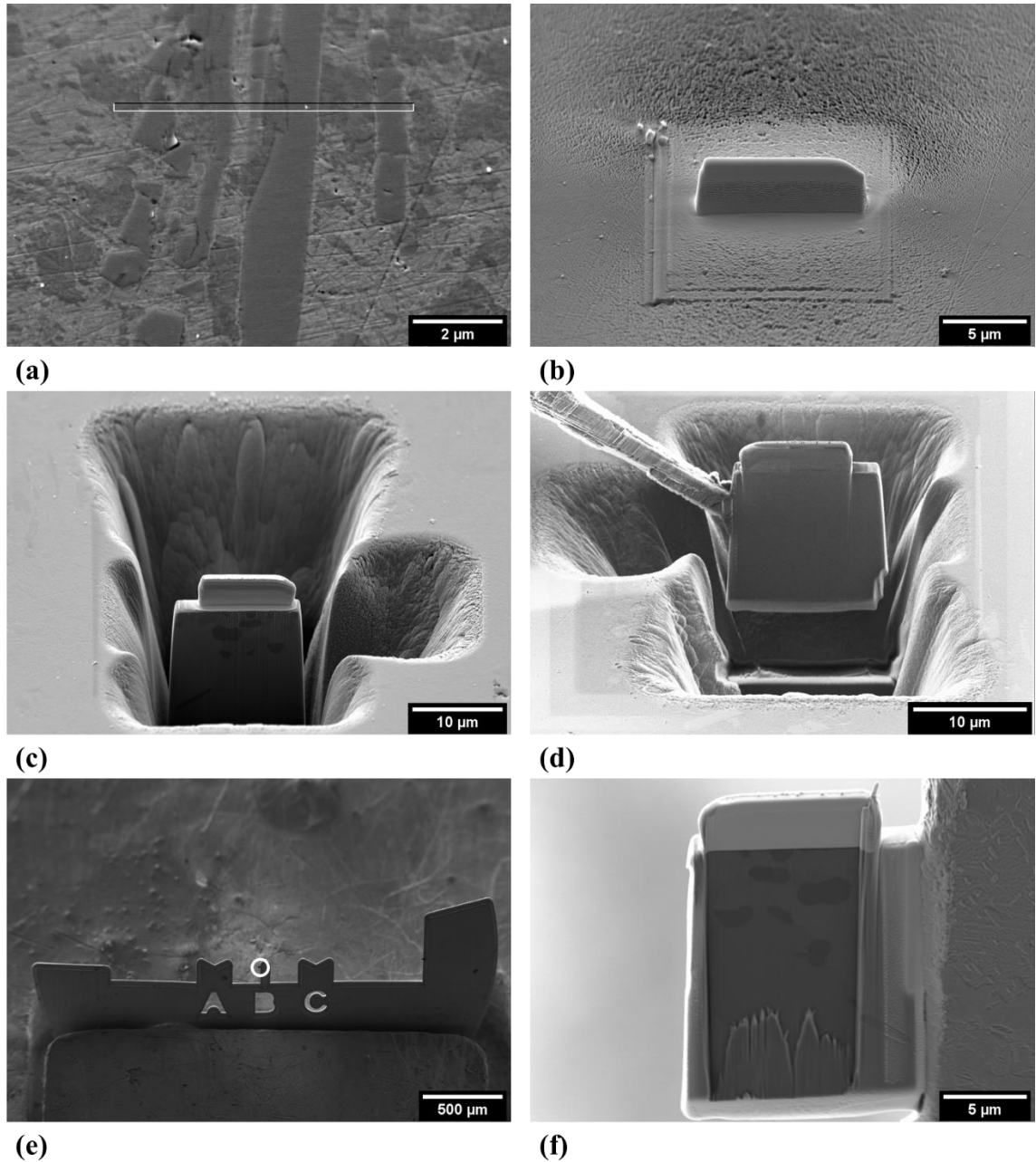


**Fig. 3.3.** SE SEM images procedure steps taken to prepare a sample for TEM observation through FIB milling. (a) Highlighted by the black and white line is the area of interest chosen for TEM observation to be milled out, which intersects TiB particles. (b) Shows the carbon coating process to protect the surface during milling while (c) shows the sections that were milled out through FIB around the area of interest. (d) Shows the lift-out process where the area of interest is micro-welded onto the tip of a needle and transferred to a separate stage seen in (e). (f) Shows the final preparation step, where the sample area of interest for TEM observation was slowly reduced using FIB to create a very thin wafer-like section.

### 3.3 Shot-peening Process

This section outlines the procedure which was followed to shot-peen wear coupons and the total circumference of fatigue samples. Shot-peening treatment was conducted at an industrial shot-peening facility, South Western Manufacturing. The top surfaces of the AM PTA-SFFF Ti-TiB wear coupons and the total circumference of fatigue samples were shot-peened for 100% coverage, from a ground surface condition of 600P. The samples were blasted for 2 minutes in an air powered system at 90 psi (approximately 621 Pa or 6.2 bar) with S-550 grade steel shots with an average diameter size of 1.05 mm. The severe plastic deformation induced to the surface of samples led to a change in surface roughness, which was evaluated before and after shot-peening at three different area locations (area size of  $1000 \times 1393.7 \mu\text{m}^2$ ) using the Keyence VK-X100 Series 3D Laser Scanning Microscope. The arithmetic mean height surface roughness ( $R_a$ ) and the root mean square surface roughness ( $R_q$ ) increased from  $R_a = 2.75 \pm 0.64 \mu\text{m}$  and  $R_q = 3.46 \pm 0.81 \mu\text{m}$  at the 600P, untreated condition to  $R_a = 6.03 \pm 0.71 \mu\text{m}$  and  $R_q = 6.21 \pm 1.06 \mu\text{m}$  at the shot-peened condition.

Following the shot-peening treatment, to prepare wear and fatigue samples, the surfaces were further ground up at 600P and 800P and polished with  $3 \mu\text{m}$  and then  $1 \mu\text{m}$  diamond polishing suspension. From this preparation, the roughness was found to decrease to  $R_a = 1.87 \pm 2.02 \mu\text{m}$  and  $R_q = 3.24 \pm 1.54 \mu\text{m}$  for Ti coupons, which based on the mean arithmetic height  $R_a$ , an approximate  $4 \mu\text{m}$  layer was removed through mechanical grinding. This step was done to help improve surface roughness for wear and fatigue testing as well as to remove any oxides and contaminants from the peening process.

## **3.4 Mechanical Testing Methods**

### **3.4.1 Rockwell Hardness Testing**

This section outlines the procedure which was followed to evaluate the bulk hardness of the AM PTA-SFFF Ti-TiB polished surfaces. Macro, micro and nano indentation hardness testing, as outlined in these subsections, was conducted to have correlative basis the various between hardness scales. Moreover, these methods are particularly useful mechanical evaluation methods for when a non-destructive evaluation approach is needed to conserve samples.

To study the bulk hardness, the testing standard outlined in ASTM E18 was followed. The Mitutoyo HR-400 Rockwell hardness tester set to the C scale as per ASTM E18 for Ti was used in testing. A Wilson C Brale diamond indenter was used with an indentation force of 150 kgf. Prior to testing, an HRC gauge block was used to verify the accuracy of the hardness tester where three measurements were performed to ensure its accuracy. Ten indentations were taken from a polished PTA-SFFF Ti-TiB unworn wear coupon surface, where each indentation was far enough from the other that influences of strain hardening from other indentations would not influence reading values. Following the testing, the average HRC hardness value is reported with the sample standard deviation from testing.

### 3.4.2 Microhardness Testing

This section outlines the procedure which was followed to evaluate the microhardness of segments of the AM PTA-SFFF Ti-TiB polished samples.

To study the bulk properties of the samples, microhardness testing was conducted following ASTM E384 [108] to determine the Vickers Hardness (HV) of samples. The average microhardness of the polished Ti coupons was evaluated using a 200 g load and a 12 second loading period taken from over 15 measurement points per sample using the Buehler Micromet II microhardness tester. Three columns of indentations were made with a spacing between rows taken as 150  $\mu\text{m}$  and a spacing between columns of 250  $\mu\text{m}$ . When hardness testing was conducted across a profile, the hardness from the three columns of indentations was averaged to give a hardness profile across a length of rows.

After all the microhardness indentations were made, each indent is observed using light-optical microscopy and micrographs are recorded for each one. Following this, each micrograph was analyzed using the ImageJ software to measure the two diagonal lengths of each indentation. From these measurements, the HV hardness is calculated as follows:

$$HV = 1.000 \times 10^3 \times P/A = 2.000 \times 10^3 P \sin(\alpha/2)/d^2 \quad (2)$$

Simplified further as:

$$HV = 1854.4 \times P/d^2 \quad (3)$$

Where P is the force (gf), A is the surface area of the indentation ( $\mu\text{m}^2$ ), d is the mean diagonal length of the indentation ( $\mu\text{m}$ ), and  $\alpha$  is the face angle of the indenter (equal to

136°0'). The average diagonal length is entered into Equation 3 and used to calculate the microhardness of the indentations, considering a 200 gf load.

### **3.4.3 Nanohardness Testing**

This section outlines the procedure which was followed to evaluate the nanohardness of the AM PTA-SFFF Ti-TiB polished samples.

The nanohardness of the untreated PTA-SFFF Ti-TiB material was evaluated through nanoindentation testing using the HYSITRON UBI 1 nano mechanical tester, which was calibrated by fused quartz prior to nanoindentation. To ensure consistency with results, samples were evaluated at different loading conditions in nanoindentation analysis to determine nanohardness and the reduced modulus of elasticity. This is a precautionary measure due to the indentation size effects (ISE) phenomenon, where samples experience load-based sensitivity based on loading conditions due to varying degrees of dislocation activity, which can influence measured nanohardness and reduced elastic modulus values [68], [109]. Thus, testing was done at loading conditions of 1, 2 and 3mN, with a standard Berkovich pyramidal-indenter at a constant loading rate of 15 $\mu$ N/s, held for 2.5 seconds at the peak load. A total of five nanoindentations were performed per loading condition at randomly distributed areas on the polished coupon surface.

The UBI 1 nano mechanical tester employs the Oliver and Pharr analysis method described in the works of [110], [111] to determine the nanohardness and reduced modulus of elasticity of samples from indentation unloading curves. In this method, the nanohardness  $H$  is defined as the ratio of the maximum load,  $P_{max}$ , to the projected area of the indentation,  $A_c$ , as follows:

$$H = \frac{P_{max}}{A_c} \quad (4)$$

Where for a Berkovich pyramidal-indenter as used in this testing,  $A_c = 24.5h_c^2$  and  $h_c$  is the contact depth at the peak load,  $P_{max}$ , calculated as follows:

$$h_c = h_{max} - \varepsilon \frac{P_{max}}{S} \quad (5)$$

With  $S$  being the unloading stiffness at the peak load and  $\varepsilon$  is the geometric constant to take into account for edge effects, which is taken as  $\varepsilon = 0.75$  in analysis.

The initial unloading contact stiffness,  $S$ , is calculated from the initial portion of the unloading curve obtained through nanoindentation testing, can be related to the reduced modulus of elasticity and the projected area of the indentation as follows:

$$S = \frac{dP}{dh} = \frac{2}{\sqrt{\pi}} E_r \sqrt{A_c} \quad (6)$$

The reduced modulus of elasticity,  $E_r$ , is defined from the following equation, where  $\nu$  is poisson's ratio and  $E$  is the modulus of elasticity:

$$\frac{1}{E_r} = \left( \frac{1 - \nu^2}{E} \right)_{sample} + \left( \frac{1 - \nu^2}{E} \right)_{indenter} \quad (7)$$

More commonly, researchers [68], [112], [113]. are using nanoindentation techniques to obtain ratios  $H/E_r$  and  $H^3/E_r^2$  (also known as the yield pressure ratio) between the nanohardness and reduced modulus of elasticity of a material as an indication of wear. With the non-destructive characteristics of nanoindentation testing, using these ratios as a rough indication of wear resistance can provide a quick and conservative method of

determining the resistance of a material to wear. The use of the ratio  $H/E_r$  can be justified as it is fundamentally known from the tribological behaviour of materials that wear and hardness are related parameters, and that a combination of high hardness and low elastic modulus gives generally good wear properties [112]–[114]. While the yield pressure ratio  $H^3/E_r^2$  can be further justified in use as a measure of a material's resistance to plastic deformation, which is seen characteristically in wearing of titanium alloys [115]. These ratios as well as the results from nanoindentation testing are presented in the result section of this thesis and further discussed.

#### **3.4.4 Uniaxial Compression Testing**

This section outlines the procedure which was undertaken to evaluate the compressive properties of the AM PTA-SFFF Ti-TiB blocks through axially compressive loading. Limited standards are available which are specific to metal AM samples, however the ASTM F3122 Standard Guide for Evaluating Mechanical Properties of Metal Materials Made via Additive Manufacturing Processes [116] outlines that the ASTM Test Method E9 is applicable and may be used to evaluate the compressive yield strength and compression strength of metal AM parts.

Three cylindrical samples were wire EDM cut for testing in the lateral, 45° diagonal, and longitudinal directions, directions as highlighted in Fig. 3.1. Samples were cut from the lower half of the same block. Dimensionally, samples were made to height of 15 mm and a diameter of 10 mm, which gave samples a 1.5 length/diameter ratio used as suggested for high strength materials per Note 4 in ASTM E9 [117]. Sample test faces and sides were ground to an 600P grit to remove all surface impurities and oxides obtained

from the wire EDM process, as described in section 3.2.1. Gauge cross-sectional areas were verified using a digital caliper at three distinct locations by measuring the diagonal of the cross-section, which was averaged for stress analysis. The height of the sample was also verified three times using a digital caliper and averaged for analysis.

Prior to testing, samples were cleaned using ethanol and sample ends were coated with the lubricant Nikal (pure nickel extreme-temperature anti-seize lubricant) to minimize influence of barrelling and buckling during testing. Samples were carefully loaded into the center of the compression plates of the machine and the top plate was lowered until contact was almost reached, then the safety door of the machine was secured shut for the duration of the test. A loading rate of 0.075 mm/min was chosen based on the size of the samples prepared to ensure a strain rate of 0.005 mm/mm-min per ASTM E9 [117]. Samples were strained up to 25% their original lengths and from each test, the data collected paired with the average measurements taken was analyzed to determine the engineering stress-strain diagram. From this, young's modulus, the 0.2% offset yield point, and the compression stress of samples at 5, 10, and 25% was determined and reported.

### **3.4.5 Uniaxial Tensile Testing**

This section outlines the procedure which was undertaken to evaluate the tensile properties of the AM PTA-SFFF Ti-TiB blocks through axially tensile loading.

With no tensile-specific standard for AM parts, the ASTM Standard Guide F3122 [116] outlines that the ASTM Test Method E8/E8M is applicable and may be used to evaluate the tensile properties of metal AM parts. Thus, tensile testing is conducted following ASTM E8 [118]. Due to the lateral dimensional restrictions of the AM PTA-



SFFF blocks, subsize tensile samples were produced with shortened grip ends, as shown in Fig. 3.4, which was found to be suitable given the gripping section capabilities of the testing machine and the success of a preliminary testing trial. Four samples per direction were wire EDM cut from the lower half and center of the same PTA-SFFF AM block for testing. All samples were grinded up until an 600P grit scheme to remove all surface impurities and oxides obtained from the wire EDM process, as described in section 3.2.1. Gauge cross-sectional areas were verified using a digital caliper at three distinct locations by measuring the width and length of the cross-section, which was averaged for stress analysis.

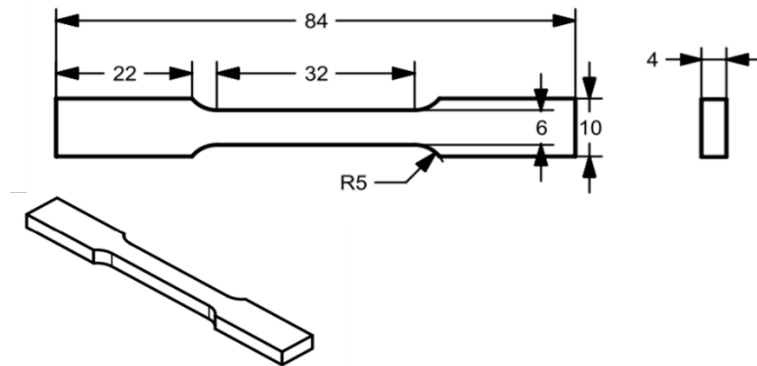


**Fig. 3.4.** Tensile sample dimensions used in testing (in mm)

Tensile testing was done using an 150kN maximum load MTS Criterion Series Universal Testing Machine with a grip clamp attachment for which samples was loaded into. A 25 mm gage extensometer was used during tensile testing to measure displacement for strain calculations at a higher accuracy. One at a time, a specimen was placed into the machine clamps and carefully tightened into position to ensure samples were evenly placed within the grips. Following this, the extensometer was clipped onto the sample and the testing machine door closed as a safety precaution. Prior to testing, data signals on the

machine were zeroed and a cross-head speed of 0.05 mm/min was chosen. A computer was used to monitor the test and all tests were run until failure was detected.

From each test, the data collected paired with the average gauge cross-sectional area of the failed sample was analyzed to determine the engineering stress-strain diagram of each sample. From this, the young's modulus, the 0.2% offset yield point, the ultimate tensile strength, the fracture stress, as well as ductility measurements such as the engineering strain at fracture and the reduction area of fracture, can be determined and reported. Tensile fracture surfaces were also observed using the FEI Quanta 200 FEG SEM equipped with EDAX energy dispersive spectrometry (EDS) at the Great Lakes Institute for Environmental Research (GLIER).

#### **3.4.6 Rotation Bending Fatigue Testing**

This section outlines the procedure which was undertaken to evaluate the fatigue properties of the AM PTA-SFFF Ti-TiB blocks in the longitudinal direction through bending-rotating fatigue testing.

To prepare samples, square cross-sectional pieces were wire EDM cut from PTA-SFFF Ti-TiB blocks in the longitudinal direction and then milled to the specified dimensions featured in Fig. 3.5. The longitudinal direction was considered to fabricate samples due to the better average performance observed in both rounds of tensile testing versus the lateral and diagonal directions (presented later in the result section) as well as the longer available length of the blocks in this dimension. The longer length allowed for excess material at the ends which made milling easier, versus the lateral dimension which would have been problematic due to size restrictions of the AM blocks in that direction.

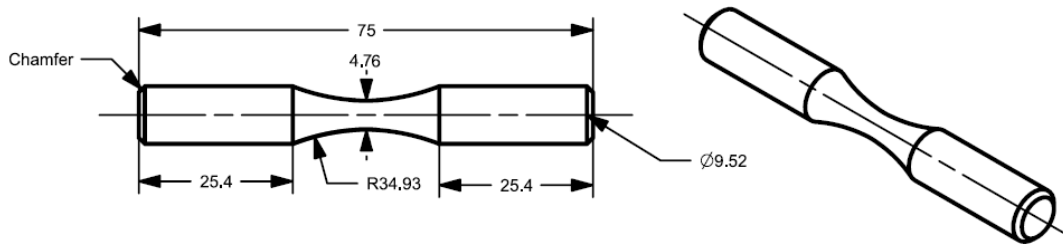


**Fig. 3.5** Fatigue sample dimensions used in testing (in mm)

For testing, untreated fatigue samples were ground and polished up until a 1  $\mu\text{m}$  poly-crystalline diamond solution, as described in section 3.2.1. Shot-peened fatigue samples were prepared as described in section 3.4. All samples were handled only with gloves to avoid contamination. In samples used in this testing scheme, the stress concentration factor of samples is reduced through polishing up to a 1-micron diamond suspension as well as the avoidance of sharp edges in the samples.

Rotating bending fatigue tests were performed using the rotating beam RBF-200 HT fatigue machine. Testing was carried out under fully reversed, pure bending condition ( $R = -1$ ) at a testing frequency of 8000 rpm. For both sample types, testing began at approximately 1/2 the UTS obtained from tensile testing of the longitudinal samples. Samples were tested where the applied stress was either increased or decreased in intervals of 25 MPa, ensuring that between 10-20 samples would fail between the  $10^4$  low cycle regime and the  $10^7$  high cycle regime. Testing stopped if a sample reached  $10^7$  cycles and did not fail, which is considered run-out and thus infinite life in this scheme. Once this occurred, stress intervals decreased to 12.5 MPa to get better insight on the fatigue endurance limit. Testing concluded once three samples were able to hit  $10^7$  cycles and not fail. Both the highest stress at run-out and a polynomial fitted endurance limit using Matlab is reported as an approximated to the fatigue endurance limit of the samples. Following

testing, the stress-life or S-N curves for both the untreated and treated samples were constructed and used to evaluate the fatigue behaviour of the samples and compare the two. Fracture surfaces of failed fatigue samples were observed using the FEI Quanta 200 FEG SEM equipped with EDAX EDS at the GLIER and used to identify patterns related to the fatigue behaviour of samples.

### **3.5 Evaluation of Tribological Properties**

#### **3.5.1 Ball-on-Disk Testing**

To evaluate the tribological properties of the PTA-SFFF Ti-TiB samples in the untreated and shot-peened treated conditions, ball-on-disk testing is considered as a wear testing method. To prepare Ti samples for wear testing, metal coupons were cut tangentially to the additive layering scheme of sample AM PTA-SFFF Ti-TiB blocks (shown in Fig. 3.6) using wire EDM to a thickness of 11 mm and a 25 mm diameter. Untreated wear samples were ground and polished up until a 1  $\mu\text{m}$  poly-crystalline diamond solution, as described in section 3.2.1, and then ultrasonically cleaned in ethanol and air-dried using an air blowing device. Shot-peened coupons were prepared as described in section 3.3, and then ultrasonically cleaned in ethanol and air-dried using a blowing device. All samples were handled with gloves on to avoid contamination on the tested surface, both in preparation, testing, and analysis. Sample roughness prior to each test was evaluated at three different area locations ( $1000 \times 1393.7 \mu\text{m}^2$ ) using the Keyence VK-X100 Series 3D Laser Scanning Microscope.

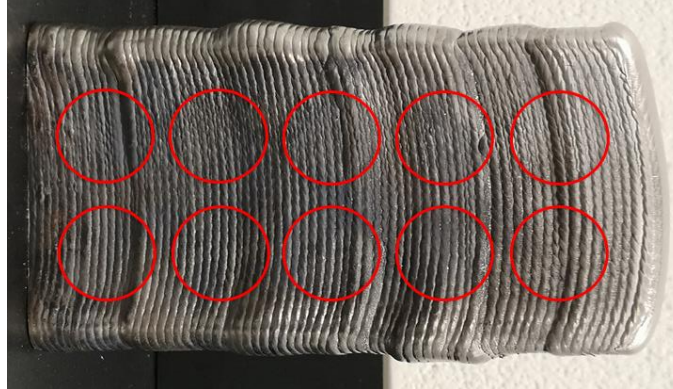


**Fig. 3.6.** Circles highlighting generally how wear coupons were cut from AM Ti-TiB PTA-SFFF blocks using wire EDM (note: circles are not to scale).

Dry-sliding wear tests were performed using a ball-on-disk tribometer (UMT CETR Bruker tribometer) following the outlined procedure of ASTM G99-17 to determine the influence on wear behaviour of the untreated and shot-peened treated material with loads varying from 1 N to 17.5 N. As shown in the early works of Archard and Hirst [114], dry-sliding load-varying wear tests for metallic materials are known for their repeatability in testing and fundamental wearing characteristics can be obtained from this evaluation, making them an essential component to understanding the tribological behaviour of these samples.

This set-up is schematically shown in Fig. 3.7 AISI 52100 balls (~800 HV) of 6 mm in diameter are chosen as the counterface sample as a common bearing material and for its significantly higher hardness than Ti, as the wear mechanisms of the Ti coupons are being investigated in this research. A constant rotational speed of 160 rpm or sliding speed of 0.1 m/s was chosen paired with a wear track diameter of 6.37 mm, giving a constant sliding distance of 300 m throughout testing. Both Ti coupons and AISI 52100 balls are weighed before wear testing, recorded to the nearest 0.0001 g measured using the high-precision Sartorius LE225D Symmetry Cole-Parmer scale, as well as after testing. Mass

wear rates are calculated from the change in mass of the samples after testing divided by the sliding distance. Tests were performed at ambient conditions of  $24 \pm 1$  °C with a relative humidity of 35 - 45%.

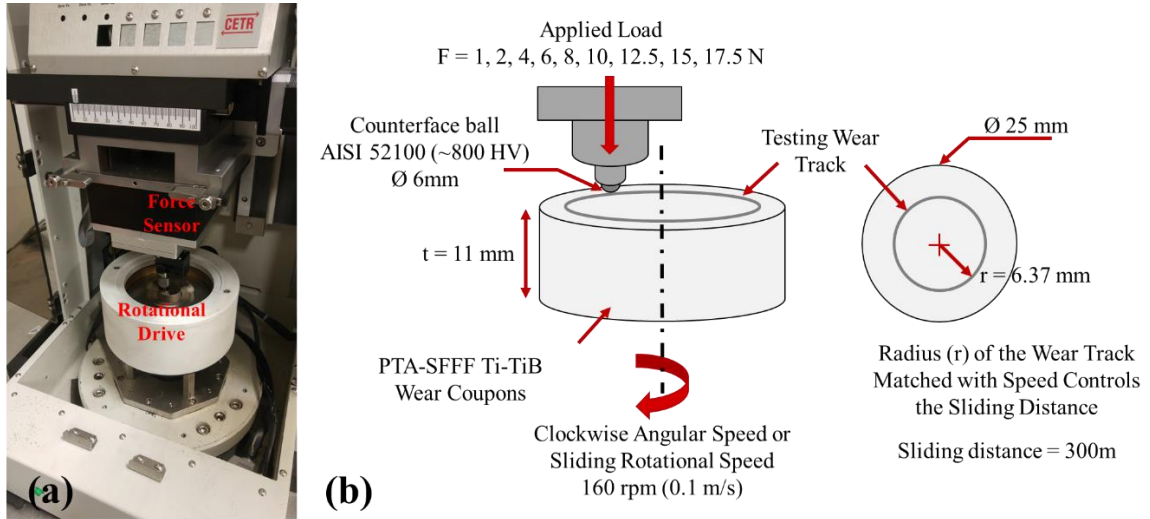


**Fig. 3.7.** (a) UMT CETR Bruker tribometer used to conduct pin-on-disk wear tests and (b) schematic illustrating the pin-on-disk testing configurations used for testing and sample specifications.

Normal and frictional forces were recorded during each test which were used to determine the COF throughout testing and the average COF. Wear debris was collected from the PTA-SFFF Ti-TiB samples for particle analysis and excess debris on all samples was blown away using compressed air before mass loss measurements and further investigations were performed. Laser optical profilometry (Keyence VK-X100), was employed to determine volumetric wear rates through line profiling from seven distinctive areas along the wear track of each PTA-SFFF Ti-TiB coupon after testing. Thirty-five line profiles were used to construct two-dimensional cross-sectional views of the wear track area, which are averaged for each sample. Knowing the radius of the wear track to calculate the circumference of the wear track and the total sliding distance, the volumetric wear rate was calculated from the average worn volume divided by the total sliding distance.

The morphology and composition of the wear tracks on both the PTA-SFFF Ti-TiB metal coupons and AISI 52100 balls were analyzed using the FEI Quanta 200 FEG SEM equipped with EDAX EDS at the GLIER. Using similar analysis techniques, debris from each test was collected and analyzed for particle size, distribution, and composition.

The subsurface of samples was further explored to observe the underlying surface damage. The highest tested load samples for each condition were chosen for observation, as they represented the maximum load scenario considered in this testing scheme. Samples were slowly cut tangentially to the wear track using a metallographic precision wafering saw with a thin diamond-coated blade, using standard cutting settings with Varsol used as a coolant. Cut samples were then cold mounted using Buehler Epothin 2 Epoxy Resin and Hardener mix with Buehler Flat Edge Filler used to retain good edge retention. Mounted samples were polished up to a 1 poly-crystalline diamond polishing step, using colloidal silica, and lightly etched with Kroll's reagent, as described in section 3.2.1. From these experiments, related results from wear testing are presented and tribological behaviour of the samples is discussed with wear mechanisms highlighted.

## CHAPTER 4: EXPERIMENTAL RESULTS

### 4.1 Metallography Characterization

#### 4.1.1 Microstructural Characterization

Figure 4.1 shows the typical equiaxed grain structure observed, etched in Kroll's reagent, which features a titanium alpha matrix with 2nd phase TiB particles found both at and within Ti grain boundaries. Cross-sections of the material were observed to have no porosity and appear fully dense. Occasional TiB clusters are observed within the structure, though generally, TiB particles appear to be distributed homogeneously across the microstructure. Observably, the AM bead interfaces were nearly undistinguishable in the etched microstructure. Microstructure grains are seen to cross bead interfaces, though it was observed that there were finer TiB particles such areas with fewer particles present in general along AM bead boundaries.

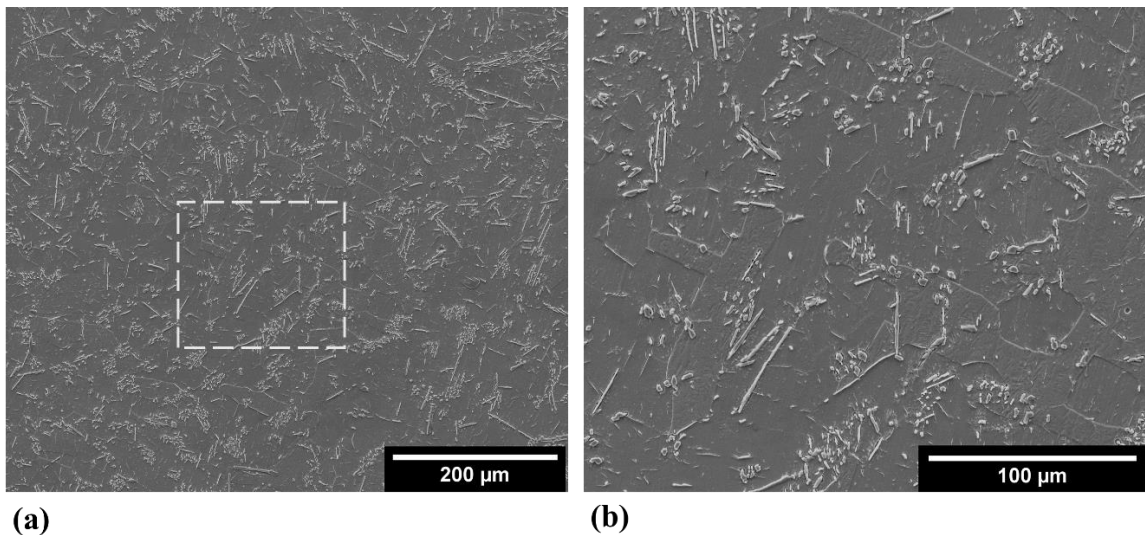


**Fig. 4.1.** Secondary electron (SE) SEM image showing (a) the typical cross-section microstructure of the PTA-SFFF Ti-TiB samples used in this investigation, etched in Kroll's etchant. (b) Highlights the higher magnification SEM image from the enclosed box region from (a), which helps show that the microstructure is comprised of an alpha grain Ti with TiB 2<sup>nd</sup> phase fibers appearing at and within Ti grain boundaries.



### 4.1.2 X-Ray Spectroscopy

Following the procedure outlined in Section 3.2.2 to obtain XRD patterns, Fig. 4.2 highlights the resulting diffraction patterns. XRD crystallography examination shows definite peaks that are consistent with the hexagonal structure of alpha Ti with a c/a ratio of 1.644. Peaks consistent with the TiB structure are further identified from XRD analysis, which are known to exist in the samples.

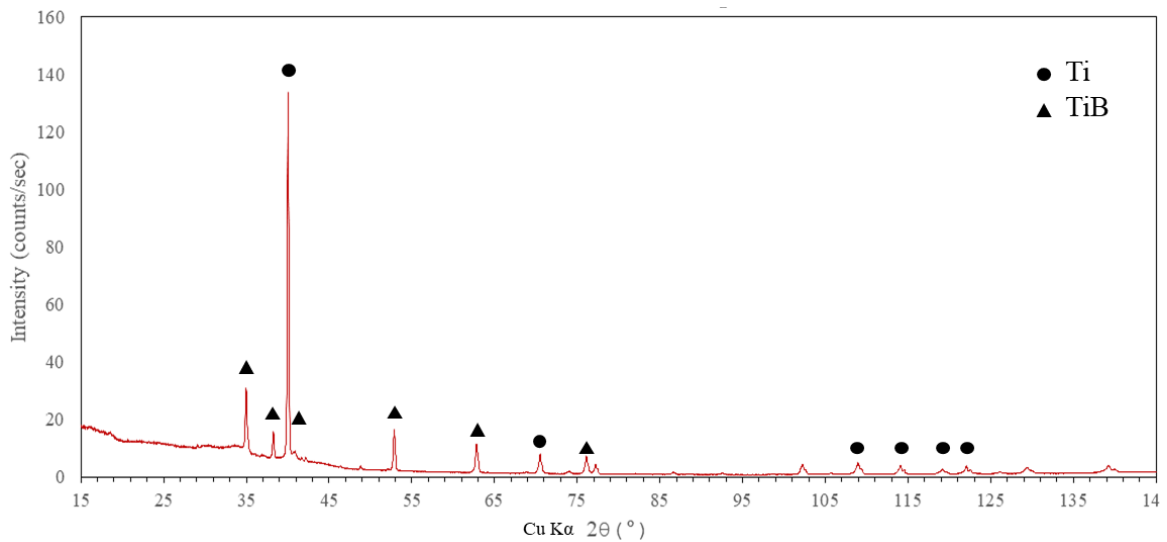


**Fig. 4.2.** XRD crystallographic patterns of PTA-SFFF Ti-TiB samples studied, showing definite peaks which are consistent with TiB and the hexagonal structure of alpha Ti.

### 4.1.3 TiB Image Analysis

From the methodology described in Section 3.2.3 for TiB particle analysis using the ImageJ software, Table 4.2 summarizes the average results obtained from analyzing the microstructures of longitudinal and lateral directed samples from three SEM micrographs at 200x magnification. Slight variations in summary distribution results is noted and can be explained due to the 2D observation of the needle-like TiB particles,

where many are shown at their cross-sectional area versus being presented along their longest length.

**Table 4.1.** Average TiB analysis distribution summary obtained from three SEM micrographs at 200x magnification, with presented sample standard deviation values

Sample microstructure orientation	Percent area covered by TiB particles (%)	Aspect ratio (height/width)	TiB width ( $\mu\text{m}$ )	TiB height ( $\mu\text{m}$ )	TiB Size ( $\mu\text{m}^2$ )
Longitudinal	$9.2 \pm 0.7$	$3.3 \pm 1.4$	$1.6 \pm 0.7$	$4.6 \pm 2.2$	$6.2 \pm 1.6$
Lateral	$9.2 \pm 1.4$	$3.3 \pm 1.5$	$1.5 \pm 0.9$	$4.5 \pm 1.7$	$6.6 \pm 1.2$

For the longitudinal and lateral sample, respectively, Fig. 4.3 and Fig. 4.4 illustrates (a) the size distribution of the 2<sup>nd</sup> phase TiB particles in terms of aspect ratio versus frequency, (b) the width distribution of the TiB particles versus frequency, and (c) the height distribution of the TiB particles versus frequency. A bimodal fitting for the aspect ratios and heights distribution patterns was found to most suitably highlight the trendline of the data presented while a normal curve fitting was applied for the distribution of the sample widths.

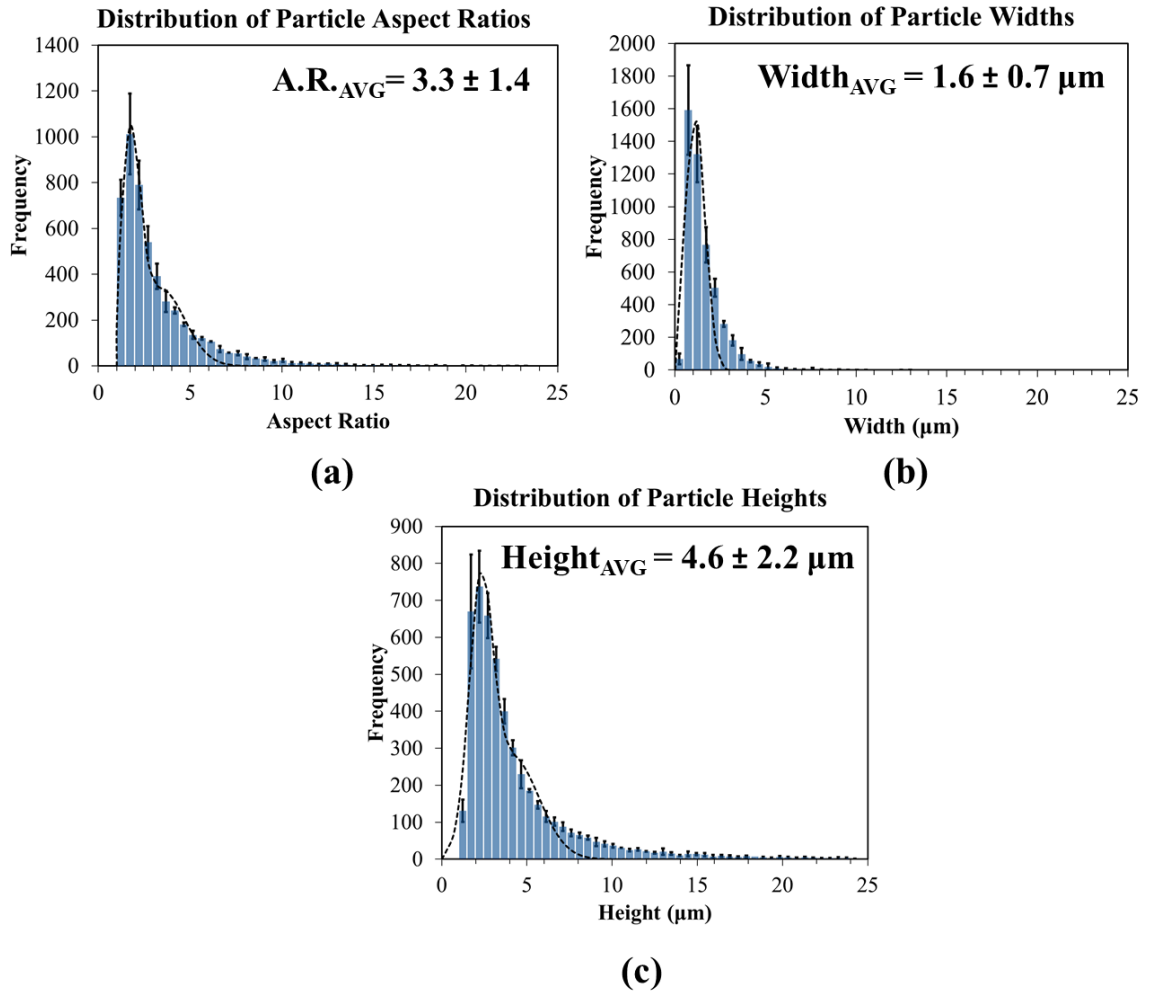


**Fig. 4.3.** Average distribution patterns for the TiB particles featured in the longitudinal PTA-SFFF Ti-TiB microstructures calculated from three SEM micrographs at 200x magnification. (a) Distribution of TiB aspect ratios (height/width) versus frequency, (b) distribution of TiB particle widths versus frequency, and (c) distribution of TiB particle heights versus frequency.

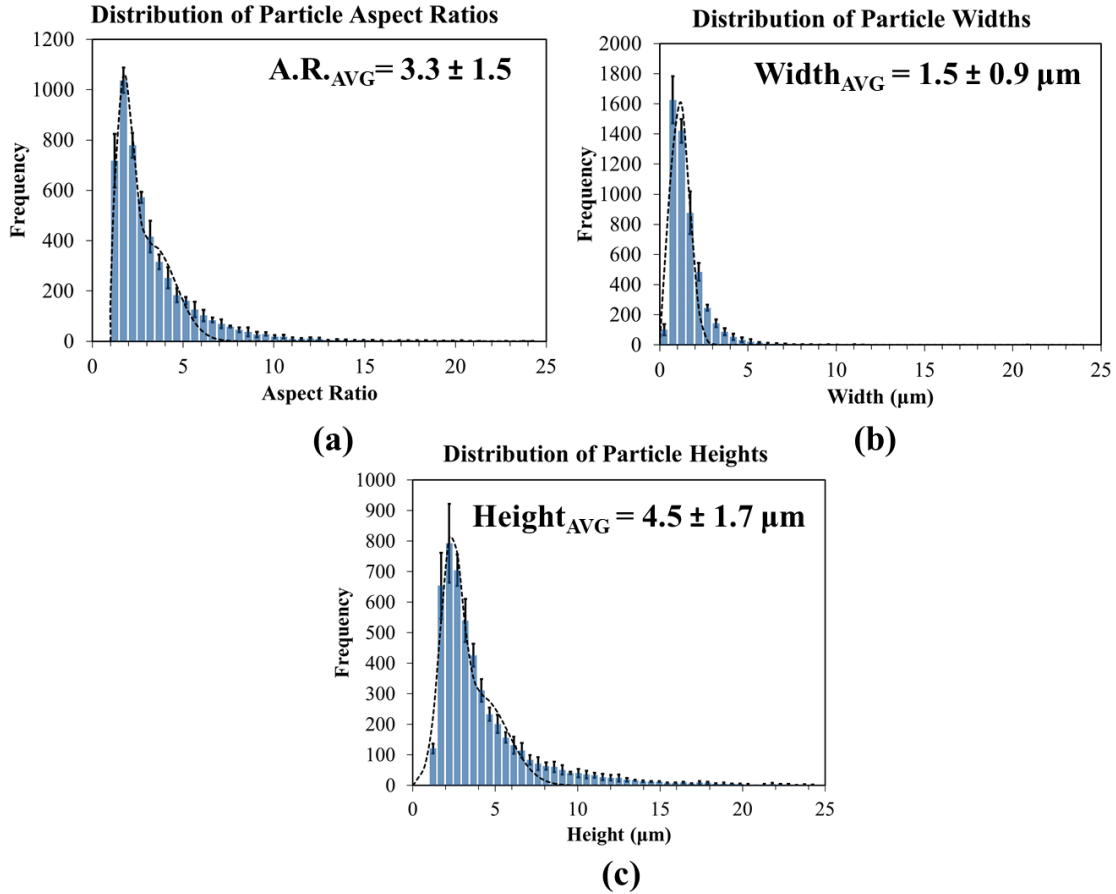


**Fig. 4.4.** Average distribution patterns for the TiB particles featured in the lateral PTA-SFFF Ti-TiB microstructures calculated from three SEM micrographs at 200X magnification. (a) Distribution of TiB aspect ratios (height/width) versus frequency, (b) distribution of TiB particle widths versus frequency, and (c) distribution of TiB particle heights versus frequency.

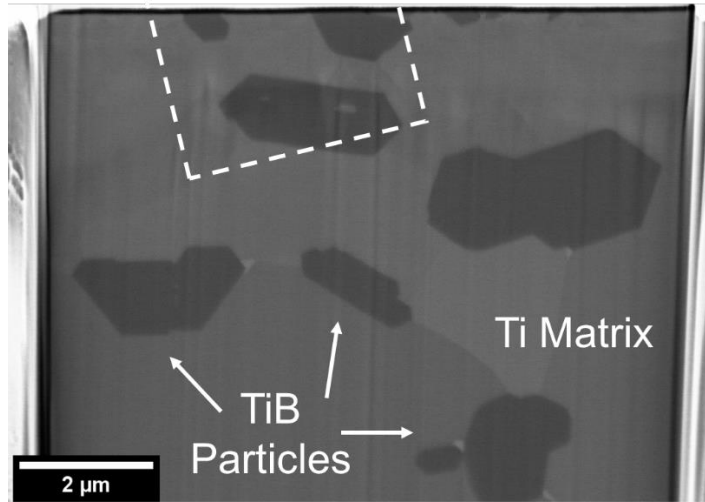
#### 4.1.4 Focused Ion Beam and Transmission Electron Microscopy

Following the procedure outlined in Section 3.2.4 for FIB and TEM analysis, Figures 4.5-4.8 feature key observations found, observable throughout the structure. Figure 4.5 shows the overall section in SEM that was prepared from FIB for TEM, which intersects a few TiB particles along their widths, as shown in Fig. 3.3 (a). Figure 4.6 (a) shows a TEM area where the analysis presented was conducted, which is taken from enclosed dashed region shown in Fig. 4.5. Figure 4.6 (b) features HR-TEM taken from Fig.

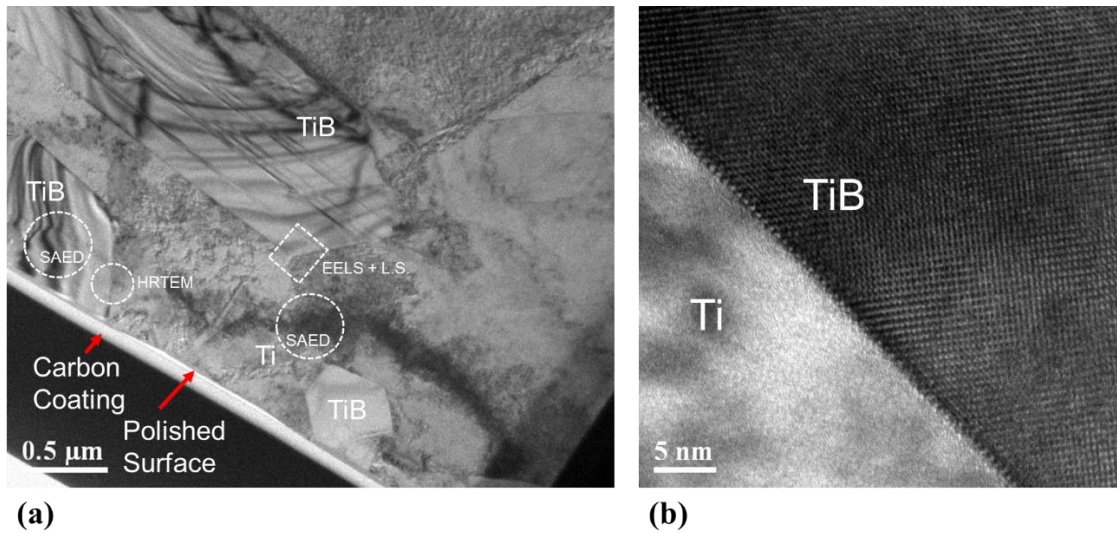
4.5 (a) which shows the interface of the Ti matrix and a TiB particle, highlighting a coherent transition from one phase to the next.

Figure 4.7 (a) and (b) presents SAED patterns obtained for TiB and for the Ti matrix, respectively. These SAED patterns were taken from the enclosed dashed circles marked in Fig. 4.8. The TiB particles were observed to be crystalline and from the SAED presented in Fig. 4.7 (a) its interplanar d-spacing was calculate to be  $d = 0.360$  nm, which corresponds to the orthorhombic (*Pnma*) crystal structure of TiB {101} planes [119]. Moreover, the Ti matrix was confirmed to be of hcp structure, expected of alpha Ti, with a confirmed d-spacing of  $d=0.262$  nm calculated from Fig. 4.7 (b) [104].

EELS mapping was done as an additional step to confirm the presence of boron in where the TiB particles were observed. The presented EELS map featured in Fig. 4.8 was taken from a separate area in Fig. 4.6 (a), highlighted by the enclosed dashed square region. The region enclosed in Fig. 4.8 (a) was analyzed though EELS and the associated map is featured in Fig 4.8 (b), where green shows the presence of boron where the particle was situated and yellow is associated to Ti. Moreover, in the TEM region pictured in 4.8 (a), a line scan was done between the TiB and Ti interface, where results of the scan are presented in Fig. 4.8 (c). In the line scan, no interfacial gap is noted between the alpha Ti and TiB as well as no drastic spikes are noted at the interface. The interface smoothly transitions from one phase to the other, exemplifying that the two phases are coherent.



**Fig. 4.5.** FIB cross-section of the AM Ti-TiB sample observed using SEM



**Fig. 4.6.** (a) TEM image taken from the enclosed region highlighted in Fig. 4.5. (b) HR-TEM image featuring a Ti-TiB interface in the material, taken from the enclosed dashed circular region as highlighted in (a).

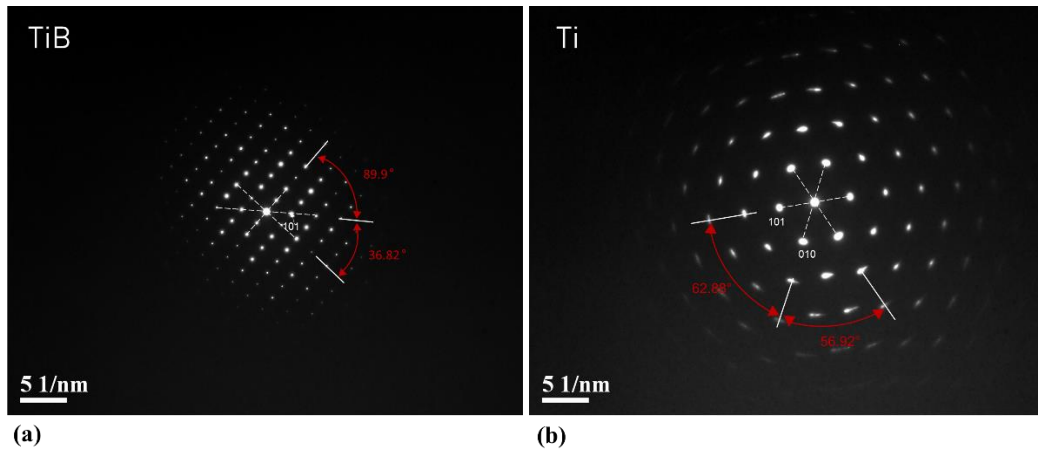


**Fig. 4.7.** SAED crystal patterns obtained from Fig 4.6 of (a) TiB and (b) Ti.

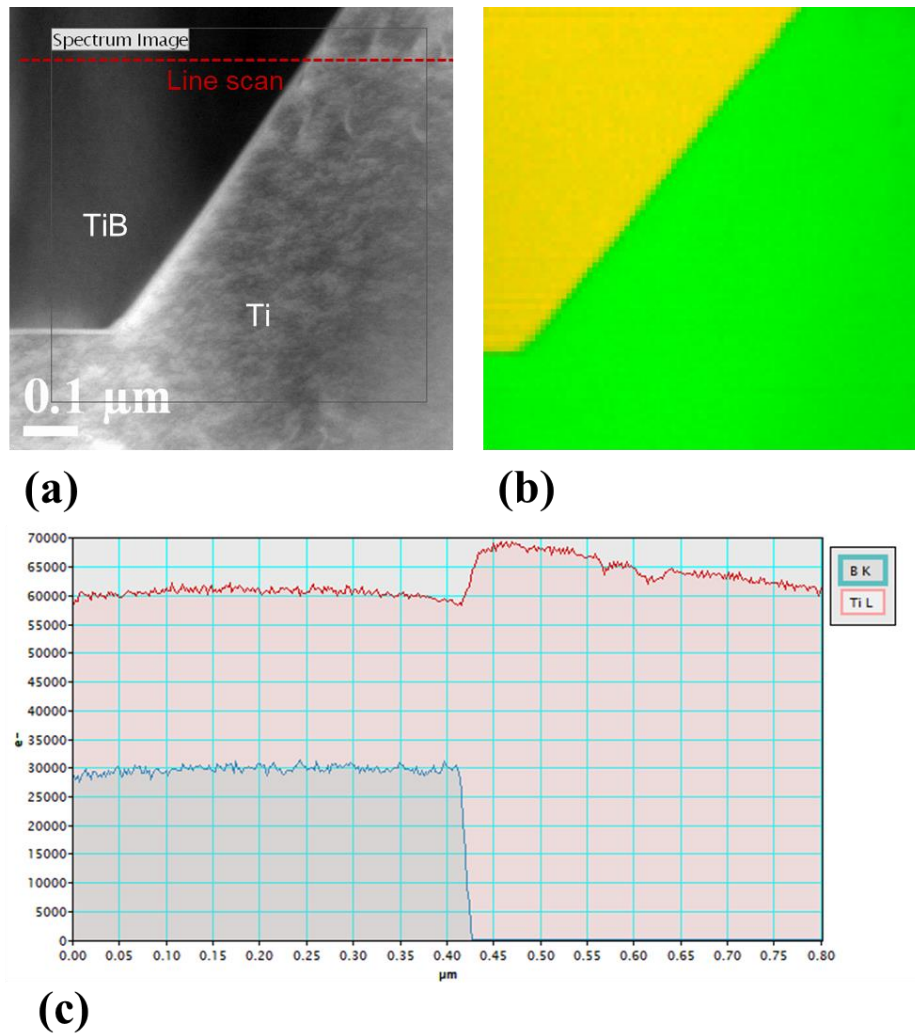


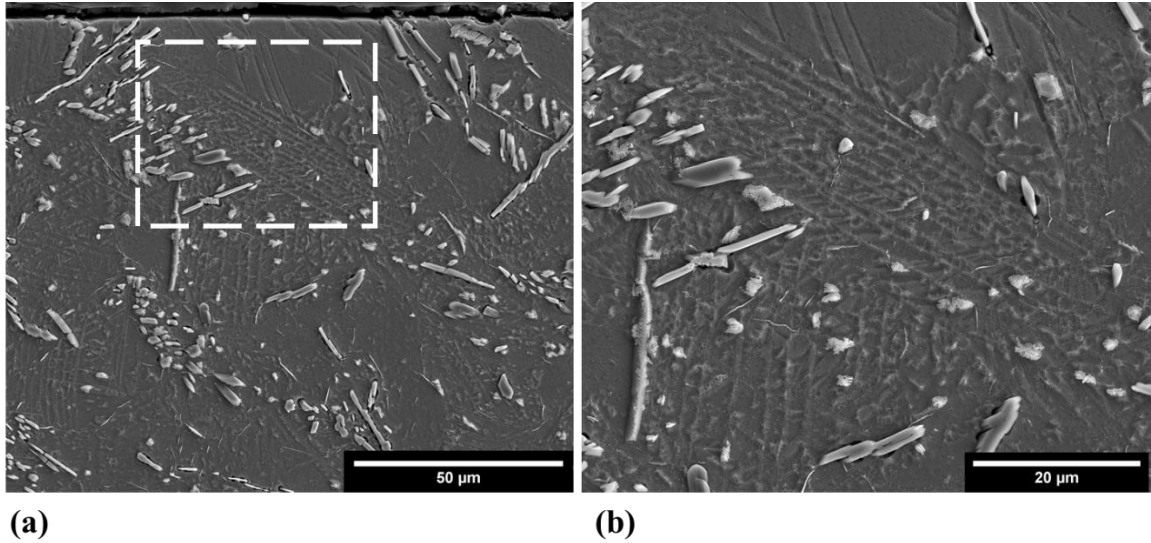
**Fig. 4.8.** (a) TEM region taken from the enclosed dash square area featured in Fig. 4.6. (b) EELS map of the area in (a), highlighting the presence of boron in yellow and titanium in green. (c) TEM line scan figure highlighting the interface of the TiB to the Ti matrix, from the dashed line featured in (a).

## 4.2 Shot-peening Microstructure Analysis

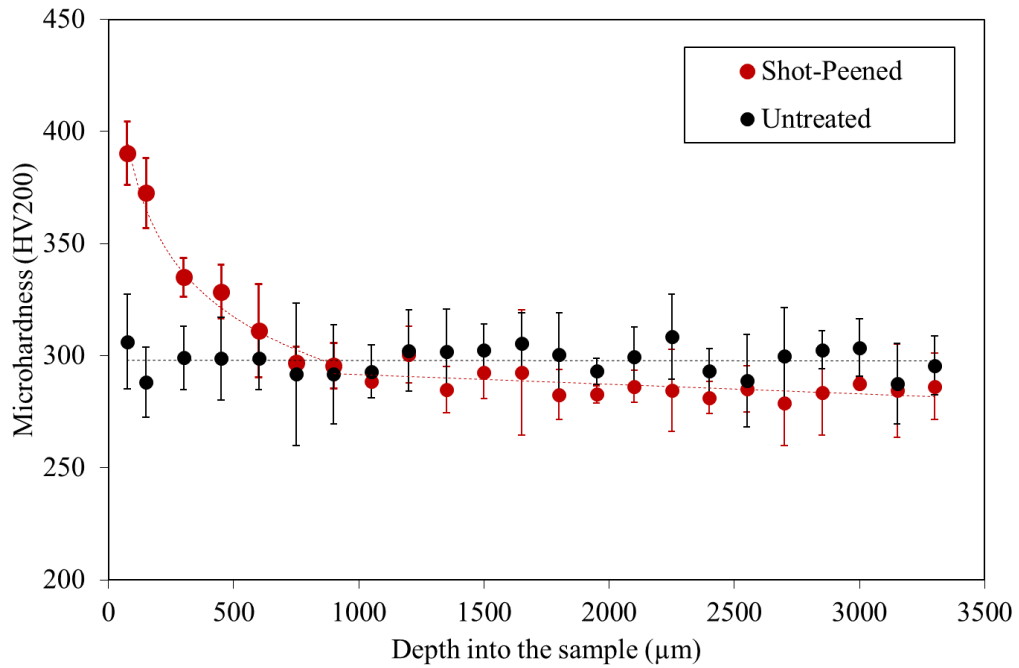
To study the influence of shot-peening on samples, a PTA-SFFF Ti-TiB coupon subjected to the shot-peening and polishing process described in section 3.3 was cut and mounted. The sample was brought to a mirror finish and etched with Kroll's etchant, per the preparation described in section 3.2.1, to observe the influence of shot-peening on the subsurface of samples. Figure 4.9 is shown representatively to highlight features observed in the subsurface of the shot-peened sample. Notably, microstructural twinning was observed as well as cross-hatched microstructural features in the subsurface, highlighting signs of shear deformation in the subsurface.

Figure 4.10 highlights the trend observed in the average microhardness profile versus depth into the sample of a polished, shot-peened PTA-SFFF Ti-TiB coupon in red in comparison to an untreated PTA-SFFF Ti-TiB coupon. Localized hardening as a result of shot-peening is observed at the shot-peened surface and the hardening effects are experienced up to 1 mm into the sample from the surface. At the surface, the average hardness of the polished shot-peened surface was found to be  $392.9 \pm 8.4$  HV, with a peak hardness measured at a point at the near-surface was found to be 400.4 HV. The hardness at the surface was observed to decrease parabolically until a depth of 1 mm was reached. From 1 mm onwards into the sample, the hardness plateaued and reached an average value of  $286.6 \pm 6.3$  HV. In comparison, untreated samples had an average hardness and higher standard deviation of  $303.1 \pm 22.5$  HV.





**Fig. 4.9.** Secondary electron SEM image showing (a) the typical sub-surface cross-section microstructure of a PTA-SFFF Ti-TiB coupon subjected to shot-peening and polished, treatment as described in section 3.3, etched in Kroll's etchant. (b) Highlights the higher magnification SEM image from the enclosed box region from (a), showing microstructural hatched features as a result of shot-peening.



**Fig. 4.10.** Average microhardness profile versus depth into the sample of a polished, shot-peened PTA-SFFF Ti-TiB coupon in red in comparison to an untreated PTA-SFFF Ti-TiB coupon.

### 4.3 Mechanical Testing

#### 4.3.1 Rockwell Hardness Testing

The HRC hardness of an AM PTA-SFFF Ti-TiB polished coupon, prepared and cut in the same manner as wear coupons described in section 3.5.1, is reported to be on average 23.7 with a low sample standard deviation 0.6 from the ten measurements taken. This hardness is superior to the HRC hardness of CP available grades of titanium, being slightly harder than grade 4 Ti, which is considered the strongest CP grade with the maximal allowable oxygen and iron content [12].

**Table 4.2.** Hardness results for AM PTA-SFFF Ti-TiB

<b>Test Number</b>	<b>Hardness (HRC)</b>
1	23.9
2	22.4
3	23.2
4	23.6
5	24.3
6	24.2
7	23.6
8	23.7
9	23.7
10	24.5
<b>Ave.</b>	<b>23.7</b>
<b>Std.</b>	<b>0.6</b>

#### 4.3.2 Microhardness Testing

The average microhardness of the polished Ti coupons was evaluated using a 200gf load and a 12 second loading period taken from over 15 measurement points per sample using the Buehler Micromet II microhardness tester. Three columns of indentations were made with a spacing between rows taken as 150  $\mu\text{m}$  and a spacing between columns of 250

$\mu\text{m}$ . The average microhardness was found to be 303.1 with a standard deviation of 22.5 HV.

### 4.3.3 Nanohardness Testing

From nanoindentation testing, Fig. 4.11 features representative unloading curves obtained from the 1, 2, and 3 mN loading conditions, highlighting the loading and unloading of the samples. A flat plateau at the top of the curve is featured from the 2.5 second hold period at the peak load. As seen in Fig. 4.12, curves obtained were smooth, not highlighting any pop-in effects, and showed consistency within the structure. Outlier curves are noted in Fig. 4.12 and some variation was observed in the loading/unloading section of curves thus why a higher standard deviation was obtained in the reduced modulus of elasticity and nanohardness from the data set. Furthermore, minimal indenter drift was recorded in testing. Table 4.4 summarizes the results obtained from the nanoindentation testing from this work and includes the HV hardness obtained as a reference. On average, the reduced modulus of elasticity and nanohardness are reported to be  $124.58 \pm 7.90$  GPa and  $4.49 \pm 0.32$  GPa, respectively. Additionally, obtained ratios of  $H/E_r$  and  $H^3/E_r^2$  from the average values obtained are 0.036 and 0.006 GPa, respectively.

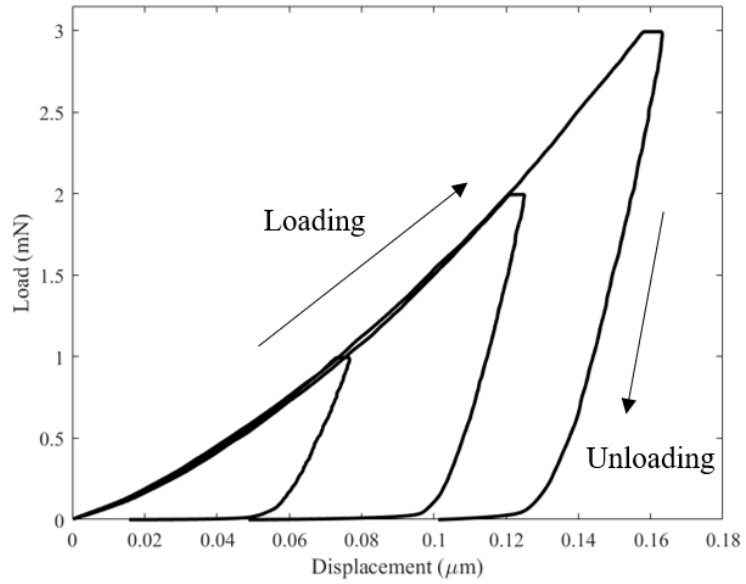


**Fig. 4.11.** Representative nanoindentation load-displacement curves of the PTA-SFFF Ti-TiB material at the loading conditions of 1, 2 and 3 mN

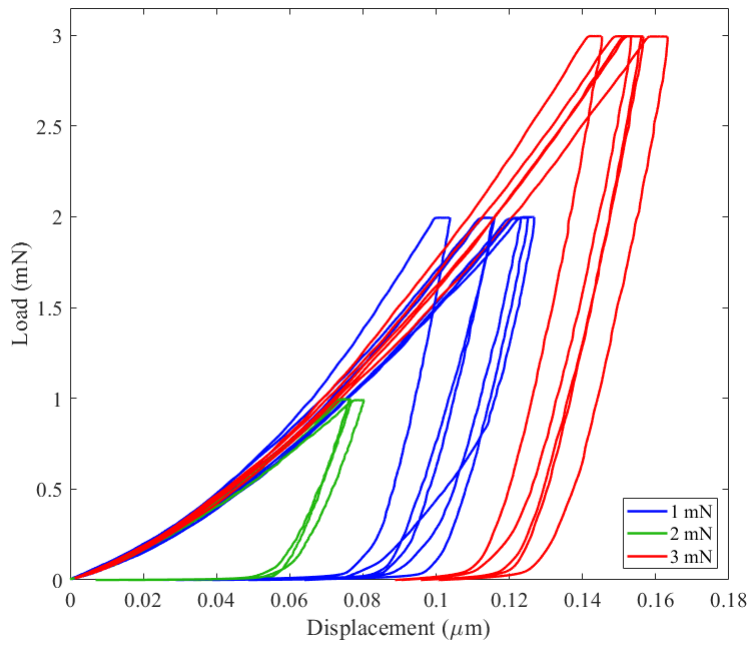


**Fig. 4.12.** Overall results of nano-indentation testing showing load-displacement curves of the PTA-SFFF Ti-TiB material at the loading conditions of 1, 2, and 3 mN

**Table 4.3.** Result summary of the mechanical properties achieved through the fabrication of PTA-SFFF Ti-TiB samples obtained by nanoindentation.

Material	Nanoindentation Load (mN)	Reduced Modulus of Elasticity, $E_r$ (GPa)	Nanohardness (GPa)	Vickers Microhardness (HV)	$H/E_r$ Ratio	$H^3/E_r^2$ Yield Pressure Ratio (GPa)
PTA-SFFF Ti-TiB (0.63 wt% B)	<b>Average</b>	124.58 ± 7.90	4.49 ± 0.32	303.1 +/- 22.5	0.036	0.006
	1	121.92 ± 9.54	4.50 ± 0.35			
	2	126.93 ± 8.05	4.45 ± 0.40			
	3	123.83 ± 8.00	4.51 ± 0.35			

### 4.3.4 Compression

The PTA-SFFF Ti-TiB samples cut from different orientations within the AM blocks, as detailed in Fig. 3.1 in section 3.1, were subjected to compression testing per the conditions described in section 3.4.4 of this thesis. Three samples were tested per direction considered. Table 4.5 reports key data findings from compression testing while the plot featured in Fig. 4.13 shows graphically the testing results plotted together.

**Table 4.4.** Compression result summary for longitudinal, lateral, and diagonally oriented AM Ti-TiB samples

Sample Orientation	Sample Number	0.2% Offset Yield Strength (MPa)	Compression Strength at 5% Strain	Compression Strength at 10% Strain	Compression Strength at 25% Strain
Longitudinal Samples	1	691.1	995.8	1213.5	1737.0
	2	576.1	819.2	1010.4	1451.0
	3	578.8	896.6	1104.6	1581.8
	<b>AVG.</b>	615.3	903.9	1109.5	1589.9
	<b>STD.</b>	65.6	88.5	101.6	143.2
	Lateral Samples	1	611.1	838.6	1027.9
2		570.8	825.7	1020.0	1463.7
3		604.4	856.5	1048.7	1486.0
<b>AVG.</b>		595.4	840.3	1032.2	1475.3
<b>STD.</b>		21.6	15.5	14.8	11.2
Diagonal Samples		1	707.3	950.1	1157.1
	2	682.5	930.0	1145.8	1627.1
	3	681.9	942.3	1155.7	1619.9
	<b>AVG.</b>	690.6	940.8	1152.9	1621.9
	<b>STD.</b>	14.5	10.1	6.2	4.5
	Overall Testing Summary	<b>AVG.</b>	<b>633.8</b>	<b>895.0</b>	<b>1098.2</b>
<b>STD.</b>		<b>56.0</b>	<b>63.1</b>	<b>73.8</b>	<b>98.1</b>

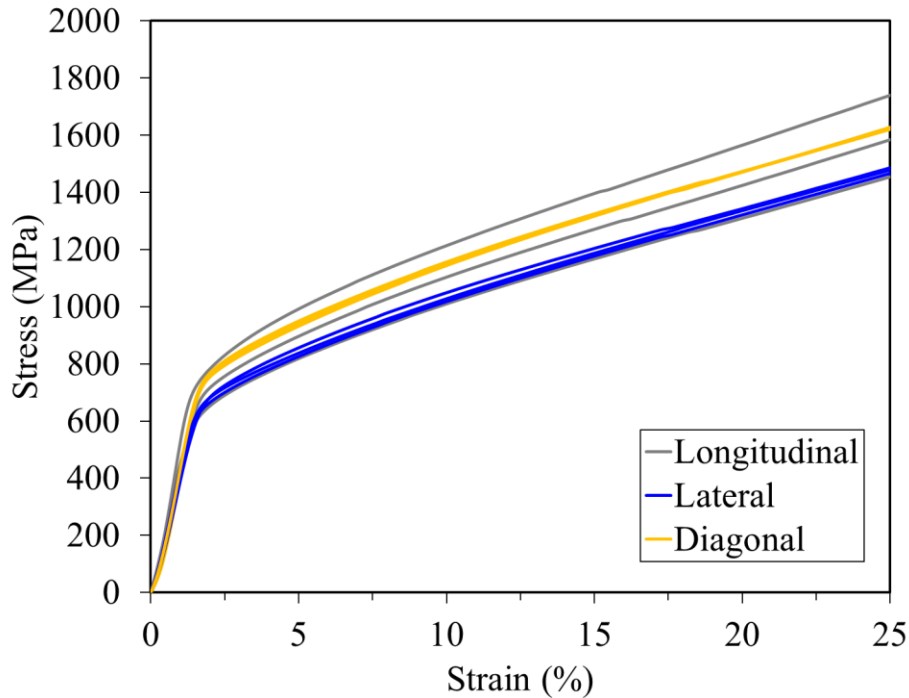


**Fig. 4.13.** Directionally oriented compression testing results for the AM Ti-TiB material, presented in the form of engineering stress versus percent strain.

Data from each test is observed to well overlap before the 0.2% offset yield point and then more divergence in testing is noted in the plastic region during compression testing.

#### 4.3.5 Tensile Testing

The PTA-SFFF Ti-TiB samples cut from different orientations within the AM blocks, as detailed in Fig. 3.1 in section 3.1, were subjected to tensile testing per the conditions described in section 3.4.5 of this thesis. Four samples were tested per direction considered. Table 4.6 reports key data findings from tensile testing while the plot featured in Fig. 4.14 shows graphically the testing results plotted together. All testing conducted showed consistency within the elastic region as well as within the plastic region, with two outlier tests seen in Fig. 4.14 for the longitudinal and diagonal directions.

**Table 4.5.** Tensile result summary for longitudinal, lateral, and diagonally oriented AM Ti-TiB samples

Sample Orientation	Sample Number	Ultimate Tensile Strength (MPa)	Elastic Modulus (GPa)	Percent Elongation (%)	Percent Reduced Area (%)	0.2% Offset Yield Strength (MPa)	Fracture Stress (MPa)
Longitudinal Samples	1	641.5	104.5	10.8	8.9	502.7	628.9
	2	602.8	103.6	8.0	10.2	472.8	594.3
	3	595.5	95.7	8.8	7.9	467.4	590.3
	4	616.3	89.3	10.2	8.7	480.0	607.7
	<b>AVG.</b>	614.1	98.3	9.5	8.9	480.7	605.3
	<b>STD.</b>	20.3	7.1	1.3	1.0	15.5	17.4
Lateral Samples	1	620.2	92.5	8.5	6.3	486.2	615.0
	2	605.6	99.9	7.0	6.2	481.1	599.9
	3	604.9	101.3	8.9	9.2	479.2	599.2
	4	606.1	96.1	8.0	6.6	473.4	599.7
	<b>AVG.</b>	609.2	97.4	8.1	7.1	480.0	603.4
	<b>STD.</b>	7.4	3.9	0.8	1.4	5.3	7.7
Diagonal Samples	1	588.8	102.4	8.9	7.7	454.2	578.3
	2	613.9	99.7	9.0	7.7	483.5	607.4
	3	600.2	101.4	10.1	8.6	468.0	588.6
	4	569.3	96.1	9.2	8.0	434.4	552.6
	<b>AVG.</b>	593.0	99.9	9.3	8.0	460.0	581.7
	<b>STD.</b>	18.8	2.8	0.5	0.4	20.9	22.8
Overall Testing Summary	<b>AVG.</b>	<b>605.4</b>	<b>98.5</b>	<b>8.9</b>	<b>8.0</b>	<b>473.6</b>	<b>596.8</b>
	<b>STD.</b>	<b>17.7</b>	<b>4.6</b>	<b>1.1</b>	<b>1.2</b>	<b>17.1</b>	<b>19.1</b>

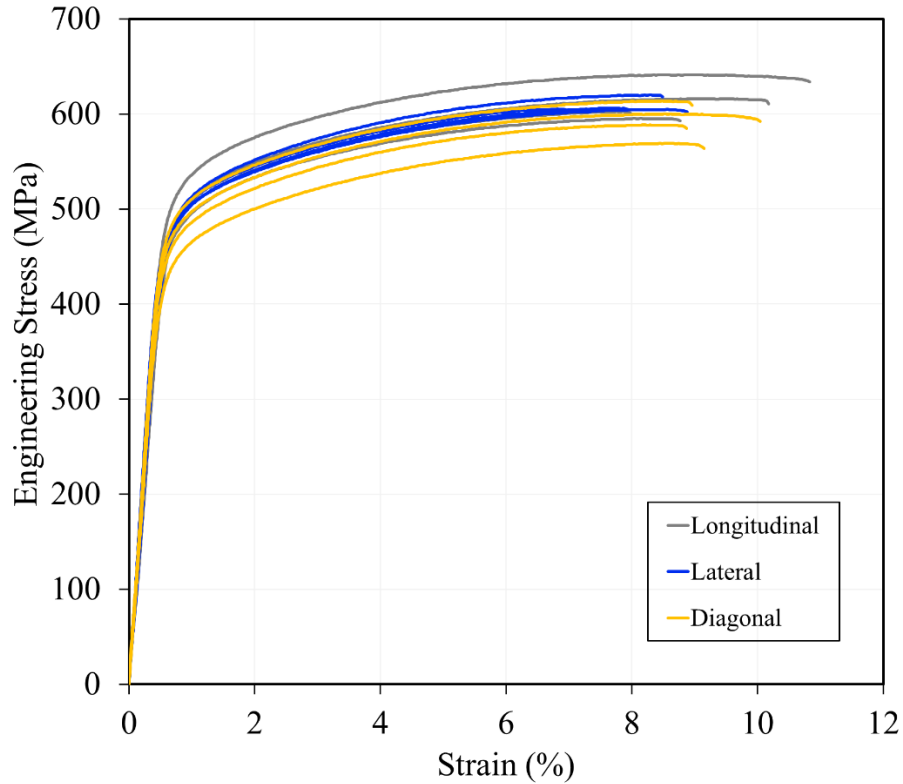


**Fig. 4.14.** Directionally oriented tensile testing results for the AM Ti-TiB material, presented in the form of engineering stress versus percent strain.

When observing the fracture surfaces of the different oriented samples using SEM, the same fracture behaviour was noted. Thus, representatively presented in Figures 4.15 & 4.16 are the SEM highlights obtained from the fracture surface analysis of the longitudinal sample 1. Figure 1 highlights the overall fracture surface of the sample through BSE and SE SEM imaging while Fig. 4.15 shows SE SEM images at higher magnification showing distinct fracture patterns observed throughout the structure. Overall, the fracture surfaces were found to have intermixed ductile-brittle fracture mechanisms, where ductile behaviour prevailed dominantly in behaviour. Figure 4.16 (a) shows an area which has two fracture patterns observed, featured in higher magnification in Fig. 4.16 (b) & (c). Figure 4.16 (b) highlights a dimpled morphology while Fig. 4.16 (c) features an area that is



observed to be more cleaved in pattern, thus more brittle, featuring needle-like fracture patterns.

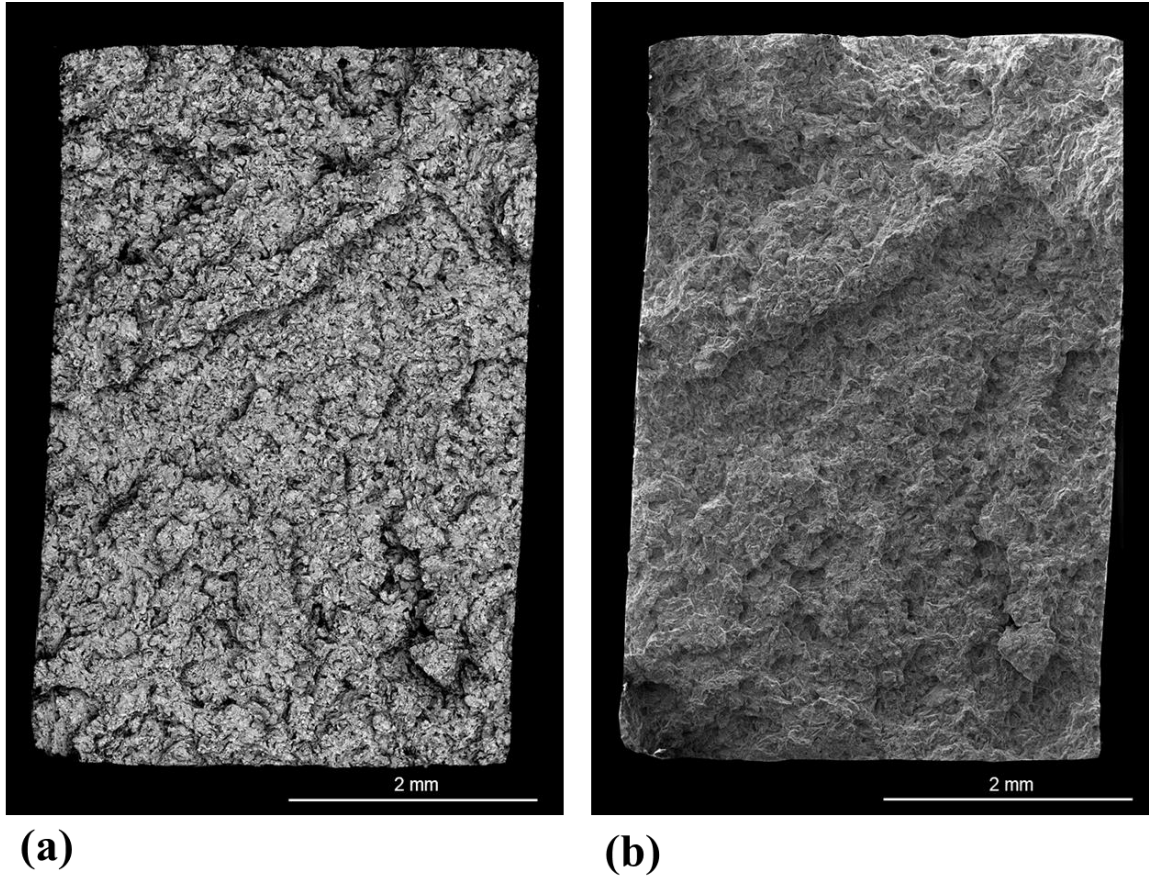


**Fig. 4.15.** SEM imaging of the tensile fracture surface of the longitudinal sample 1 through (a) BSE and (b) SE.

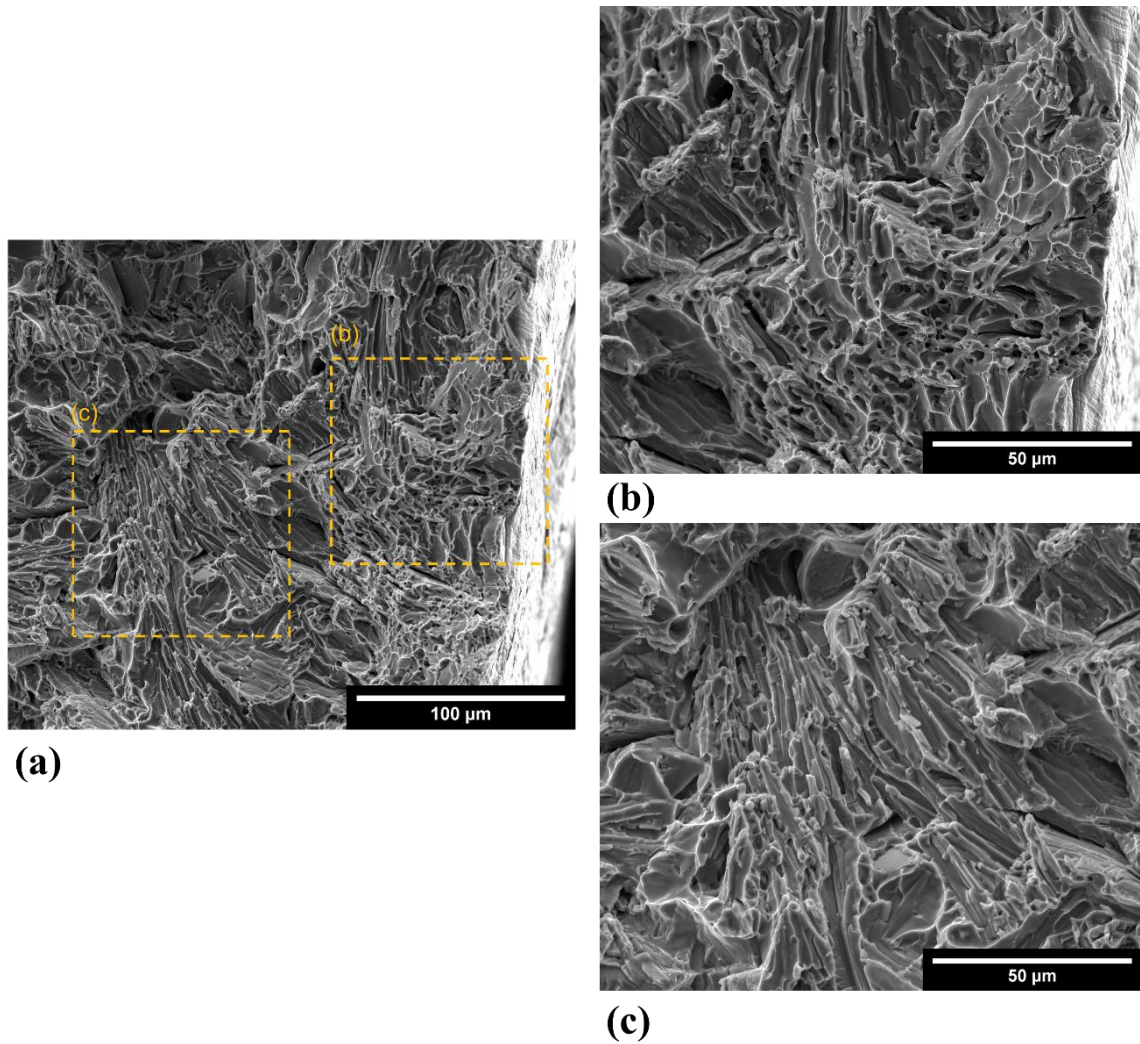


**Fig. 4.16.** (a) SE SEM image showing representative tensile fracture surface of the longitudinal sample 1, highlighting typical fracture features observed. (b) SE SEM higher magnification image taken from the enclosed area as highlighted in (a), exhibiting dimpled morphology. (c) SE SEM higher magnification image taken from the enclosed area as highlighted in (a), showing a less-ductile, more cleaved region in the same area.

### 4.3.6 Fatigue Testing

Rotating-bending Fatigue testing was conducted as described in section 3.4.6 using the RBF-200 HT fatigue machine at a revolution speed of 8000 rpm for AM PTA-SFFF Ti-TiB samples, untreated and treated through the shot-peening process described in section 3.3. From measurements of all samples, the untreated samples on average had surface roughness values of  $R_a = 2.55 \pm 0.39 \mu\text{m}$  and  $R_q = 3.11 \pm 0.45 \mu\text{m}$ . Due to small

dimples and asperities remaining that were not smoothed out from light grinding and polishing of shot-peened samples prior to testing, they were found to be slightly rougher with values of  $R_a = 3.20 \pm 1.11 \mu\text{m}$  and  $R_q = 4.85 \pm 1.60 \mu\text{m}$ .

In fatigue testing, all fatigue samples broke approximately in the middle of the thinned section of the thinnest diameter, indicating good sample preparation and a reliable testing scheme. Figure 4.17 features the fatigue life S-N diagram compiled from testing both untreated and shot-peened samples from the low to high cycle fatigue regimes. Overall, the shot-peened samples performed significantly better than untreated samples, being able to sustain higher stress amplitudes at similar sample life cycles in comparison to the untreated samples. For the untreated samples PTA-SFFF Ti-TiB samples, the highest stress at run-out was  $282.5 \pm 5.4 \text{ MPa}$  whereas the fitted endurance limit was  $247.8 \pm 5.4 \text{ MPa}$ . For shot-peened samples, the highest stress at run-out was  $332.5 \pm 5.4 \text{ MPa}$  and had a fitted endurance limit of  $318.3 \pm 5.4 \text{ MPa}$ , which is associated to an approximate 28% increase in fatigue resistance. The standard error of  $\pm 5.4 \text{ MPa}$  reported with these values is related to measurement error in the machine during loading.

SEM images appearing in Figures 4.18-4.21 are used to present key patterns observed in the fracture surfaces of samples. Overall in all fractured samples, three distinct fracture regions were identified as follows: Region I, Region II, and Final Rupture. Region I is defined as the area in which fatigue crack initiation and the initial, slower crack propagation occurred. For both untreated and shot-peened samples, Region I was found to be flat and, while striations were observed within Region I, cleavage steps and planes were observed in higher presence. Thus, Region I was observed to be dominated by brittle fracture mechanisms throughout all samples. The Final Rupture region is the largest region

by area for all samples studied and is the where fast fracture occurs. Generally, throughout all samples this area was rougher than Region I and featured a dimpled morphology, thus was ductile in nature. Last of all, Region II was considered the transitional region between Region I and Final Rupture and had both brittle and ductile dominating fracture behaviour patterns. Figures 4.18-4.21 show for each tested sample type selected SEM images which show key details of Region I and the Final Rupture region. For both untreated and shot-peened treated samples, two figures are depicted which are chosen from the low ( $<10^5$ ) and high cycle ( $>10^5$ ) fracture life regimes from testing.

For AM Ti-TiB untreated samples, fatigue cracks were found to originate at the surface of the tested samples, with the majority of cracks observed to start at localized surface defects for both the low and high cycle fatigue regimes. The fracture surface presented in Fig. 4.18 (a) features this behaviour, where Fig. 4.18 (b) shows in higher magnification the crack initiation area of a fatigue sample which was tested at a stress amplitude of 307.5 MPa and failed at 105,300 cycles. In Fig. 4.19 (b) in one fatigue sample, which was tested at a stress amplitude of 432.5 MPa and failed at 24,600 cycles, the initial crack propagation area was observed at the surface where localized TiB particles were somewhat agglomerated. In the Final Rupture zone of the untreated samples, dimples with some cleavage planes are noted, as shown in Figures 4.18 (c) and 4.19 (c). Figure 4.18 (c) has TiB particles situated around dimpled areas and shows TiB needles which either are seen to be whole and coherent within the Ti matrix despite fracture or have broken but remain coherent to the Ti matrix, with no particle pull-out observed. Figure 4.19 (c) further illustrates this in a non-dimpled area in the Final Rupture region, showing TiB particles within are intact or broken which both remain coherent in the Ti structure.

In contrast, all shot-peened AM Ti-TiB samples observed had crack initiation sites at the subsurface and exhibited void nucleation at these regions for both the low and higher cycle fatigue regimes. Both Figures 4.20 and 4.21 show this behaviour in samples, where typically the crack initiation site is roughly situated between 0.5 to 1.5 mm in the subsurface of samples, which no observable dependency of its location on applied load and cycle life. Similarly to the untreated samples, the shot-peened samples had TiB particles which were observed to stay intact or break but both remained coherent in the structure with no particle pull-out within the Final Rupture zone. Figure 4.21 (c) shows this for a shot-peened sample, where small TiB particles are seen to stay coherent to the structure and are observed within dimples which are present. One key distinguishing factor for the fracture surfaces of the shot-peened samples and the untreated samples was the presence of a cross-hatched fracture surface, showed in Fig. 4.20 (c). This cross-hatched fracture surface was observed in all shot-peened samples and was only found at the near-subsurface of the Final Fracture area.

Throughout testing of both sample types, it was noted that with decreasing stress amplitude and going from high to low cycle regimes, the size of Region I and II increased while the Final Rupture zone decreased. Apart from that observation, negligible differences in fracture behaviour and between the low and high cycle fatigue regimes were observed.

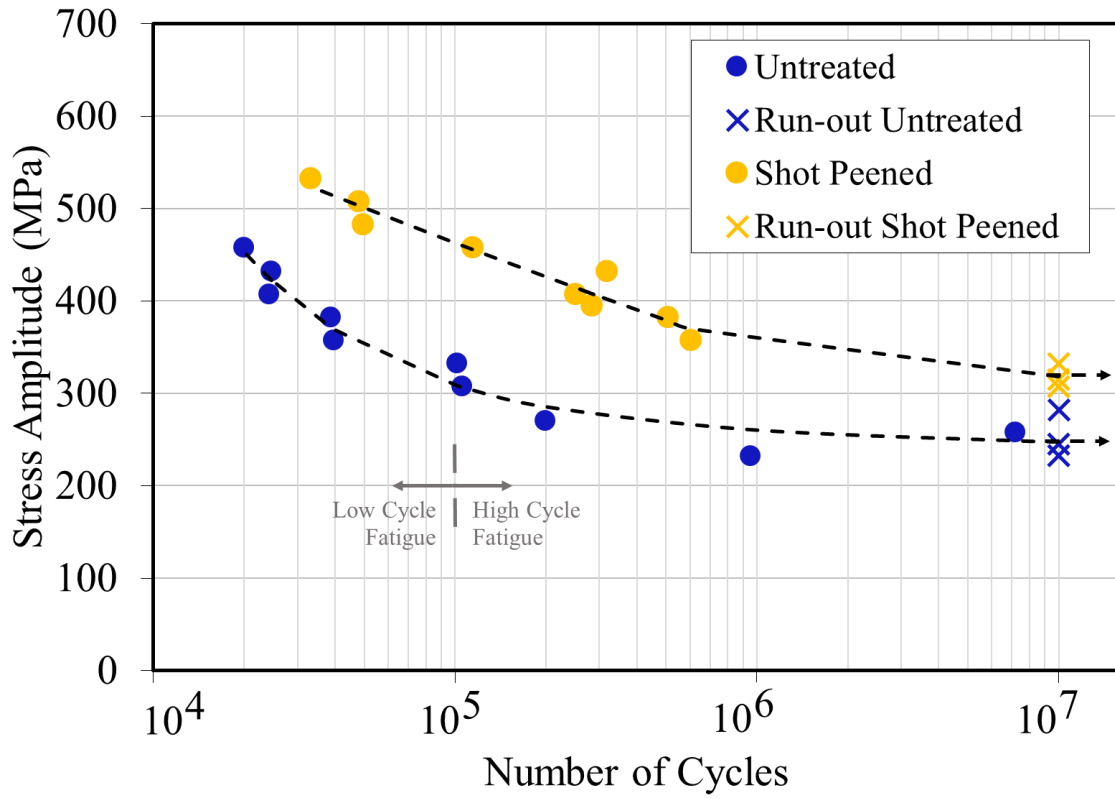


**Fig. 4.17.** Fatigue stress amplitude versus number of cycles, S-N diagram from the untreated and shot-peened PTA-SFFF Ti-TiB material

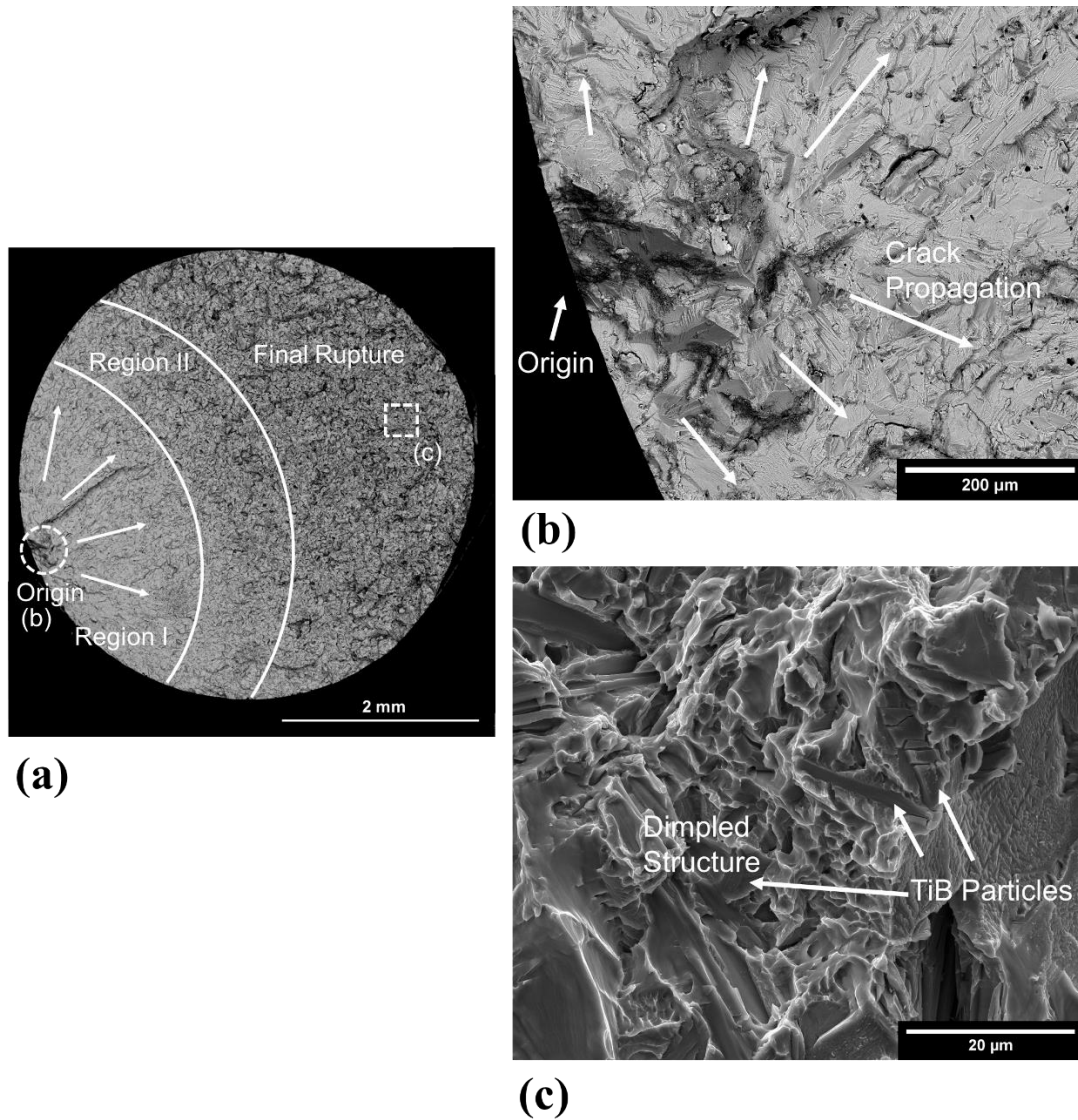


**Fig. 4.18.** (a) BSE SEM image highlighting the overall fracture surface of a PTA-SFFF Ti-TiB fatigue sample which was tested at a stress amplitude of 307.5 MPa and failed at 105,300 cycles. (b) BSE SEM image highlighting the fatigue crack origin and crack propagation, taken from the enclosed area in Region I highlighted in (a). (c) SE SEM image showing a dimpled fracture surface with TiB particles, taken from the enclosed area in the Final Rupture region highlighted in (a).

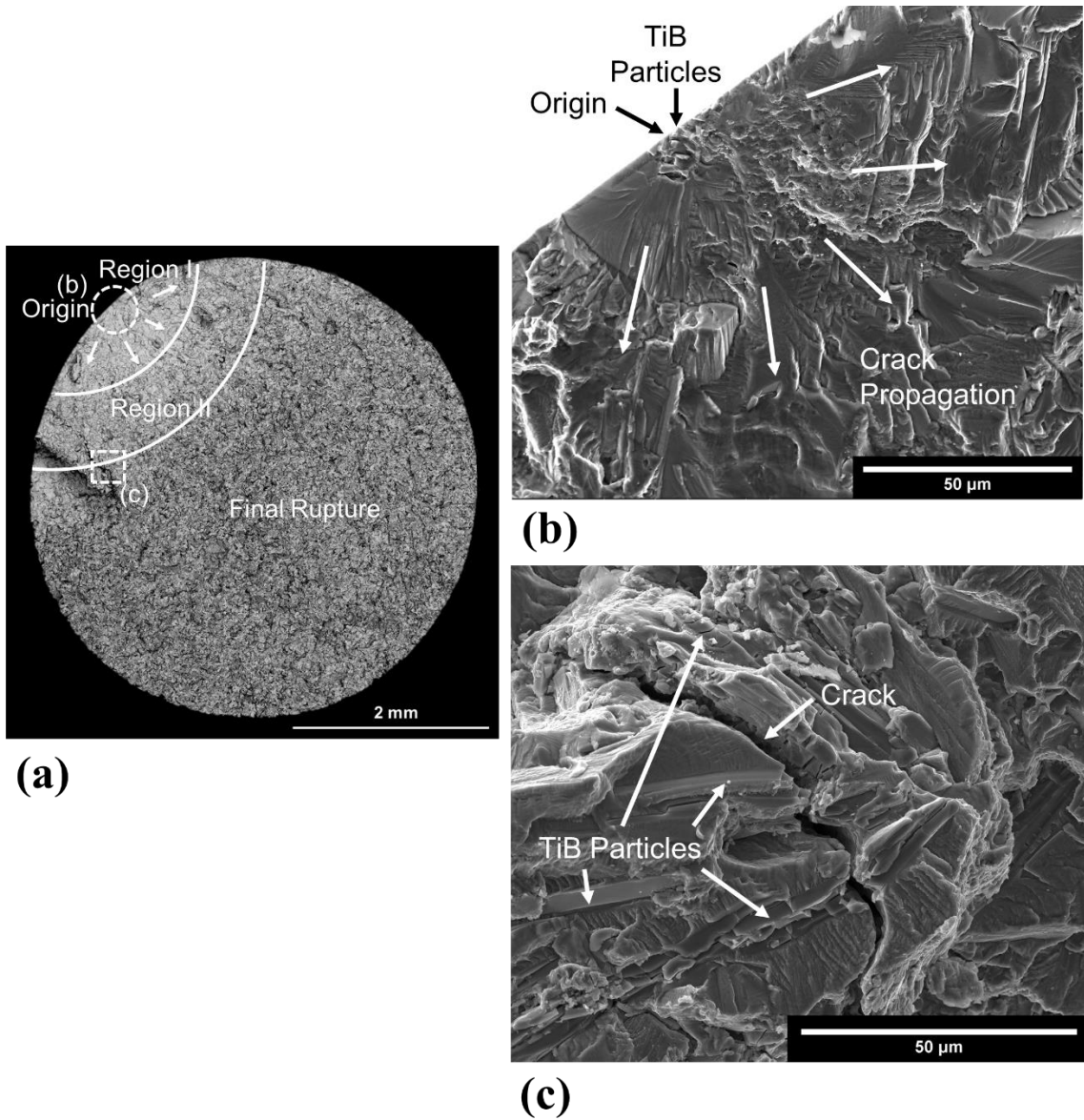


**Fig. 4.19.** (a) BSE SEM image highlighting the overall fracture surface of a PTA-SFFF Ti-TiB fatigue sample which was tested at a stress amplitude of 432.5 MPa and failed at 24,600 cycles. (b) SE SEM image highlighting the fatigue crack origin and crack propagation, taken from the enclosed area in Region I highlighted in (a). (c) SE SEM image showing a cracked fracture surface with TiB particles, taken from the enclosed area in the Final Rupture region highlighted in (a).



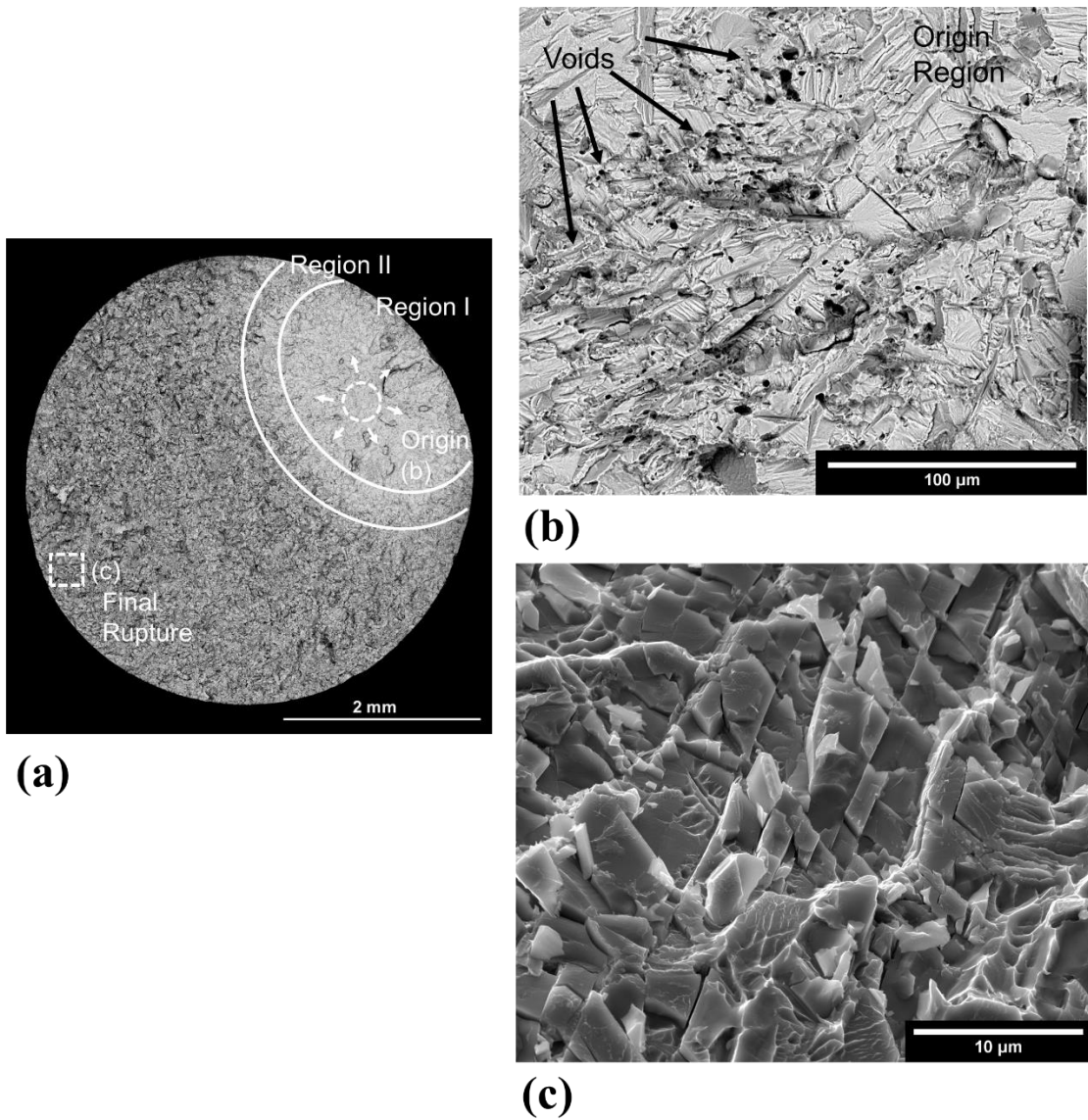


**Fig. 4.20.** (a) BSE SEM image highlighting the overall fracture surface of a shot-peened PTA-SFFF Ti-TiB fatigue sample which was tested at a stress amplitude of 382.5 MPa and failed at 506,700 cycles. (b) BSE SEM image highlighting the fatigue crack origin area, taken from the enclosed area in Region I highlighted in (a). (c) SE SEM image showing a cross-hatched, cracked fracture surface, taken from the enclosed area in the Final Rupture region highlighted in (a).

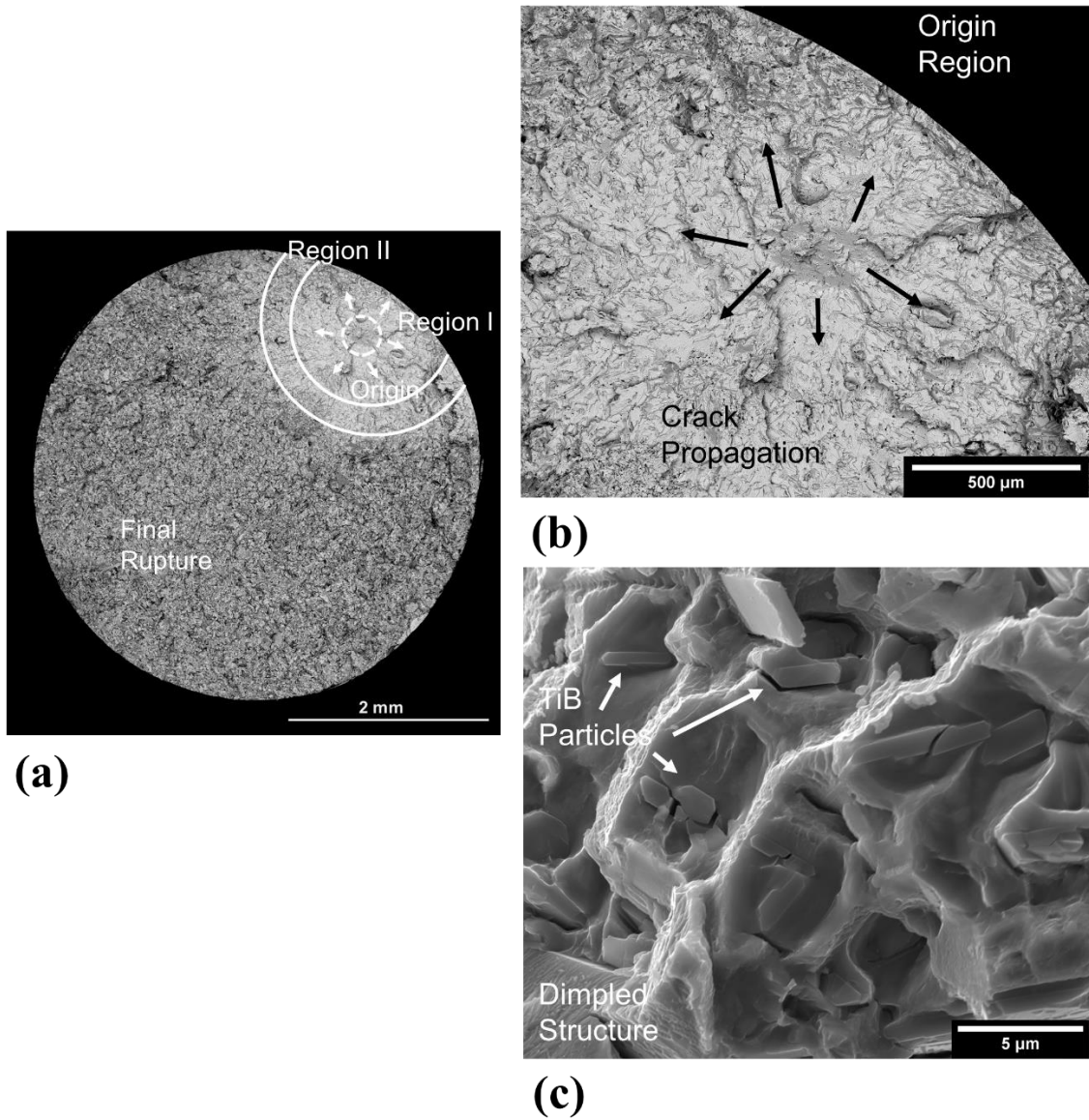


**Fig. 4.21.** (a) BSE SEM image highlighting the overall fracture surface of a shot-peened PTA-SFFF Ti-TiB fatigue sample which was tested at a stress amplitude of 507.5 MPa and failed at 48,000 cycles. (b) BSE SEM image highlighting the fatigue crack origin area, taken from the enclosed area in Region I highlighted in (a). (c) SE SEM image showing a dimpled structure with TiB particles within dimples, taken from the enclosed area in the Final Rupture region highlighted in (a).

## **4.4 Ball-on-disk Testing**

### **4.4.1 Coefficient of Friction and Wear Rates**

Dry sliding, load-varying ball-on-disk testing using AISI 52100 steel balls as a counterface was conducted with loads varying from 1-17.5N to understand the tribological properties of the untreated and shot-peened treated PTA-SFFF Ti-TiB sample conditions. For both conditions, the variation of the COF versus sliding distance was found in each test, which is show representatively in Fig. 4.22 for the 2, 6, 10, and 15N load testing schemes. An increasing trend in the length of the break-in region before steady-state is reached was observed and a decrease in the average COF with increasing applied normal loads for both tested conditions. While the results observed between the two sample conditions are very similar, shot-peened samples were observed to have slightly longer break-in areas as well as observed to have less steady, more noisy COF data trends. Figure 4.23 summarizes the average COF for the untreated (Fig. 4.23 (a)) and shot-peened (Fig. 4.23 (b)) sample conditions. For both samples, a decreasing trend in the average COF with increasing applied normal load is further observed from these results. Note, a 17.5 N test was unable to be conducted for a shot-peened sample as normal loads fluctuated in testing past the threshold 19N warning level of the machine, which has an upper testing limit of 20N. Thus for the safety of the apparatus, the 17.5N applied normal load shot-peened wear test was stopped and not continued.

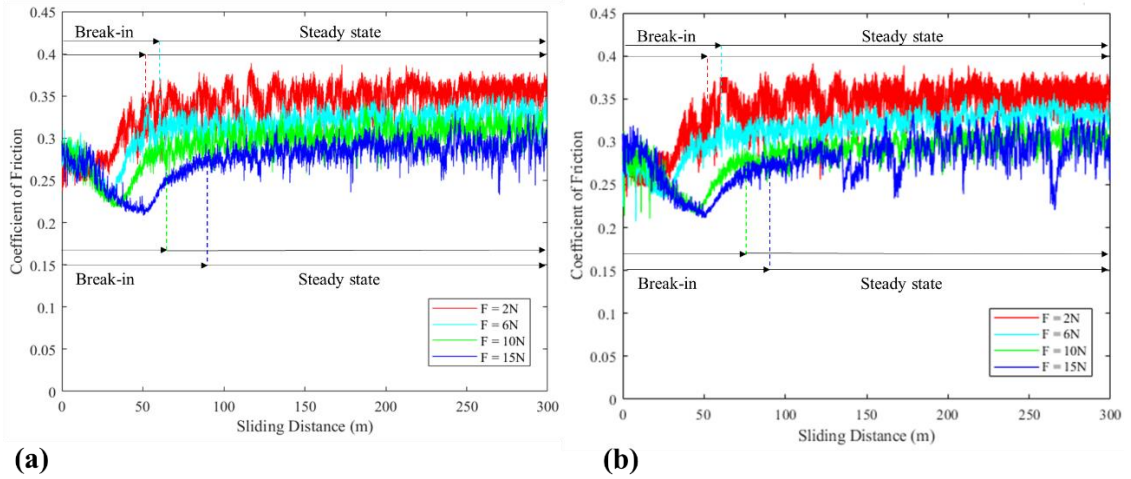


**Fig. 4.22.** Variation of the coefficient of friction (COF) with sliding distance for representative applied loading schemes of 2, 6, 10 and 15N, for the PTA-SFFF Ti-TiB samples in the (a) untreated and (b) shot-peen treated conditions.

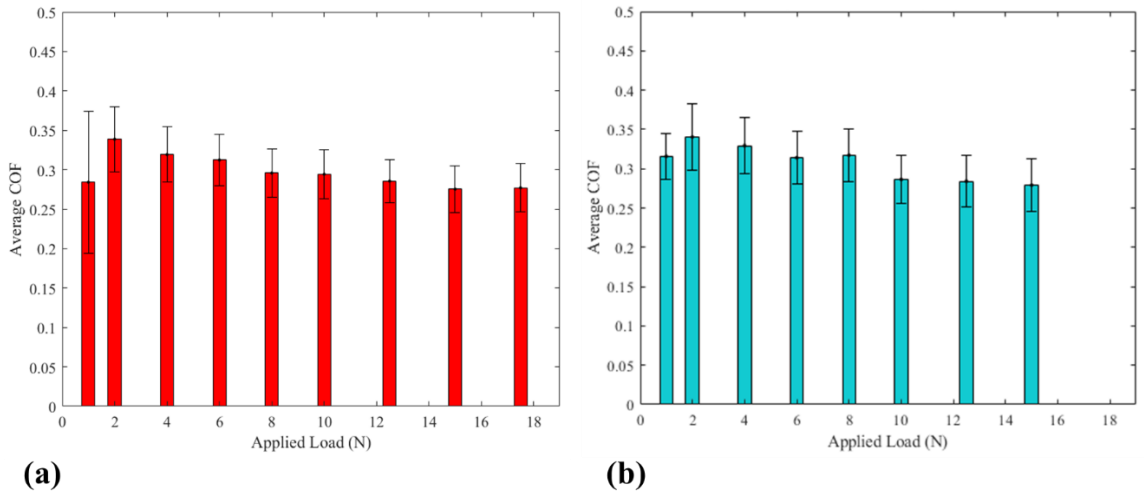


**Fig. 4.23.** Variation of the average COF as a function of applied load for PTA-SFFF Ti-TiB samples, showing an initial increase of average COF and then a gradual decrease with increasing load.

Volumetric and mass wear rates of the untreated PTA-SFFF Ti-TiB coupons are shown in Fig. 4.24 (a) and Fig. 4.25 (a), respectively. Mass wear rates are based on the change in mass of the coupons before and after testing while volumetric wear rates are based on the laser optical profilometry (Keyence VK-X100) wear track scans. A consistent linear trend in both wear rates is observed up until the 10 N applied loading condition. Past 10 N, a departure from the initial linearity is observed. This change in wear rate behaviour also corresponds to a change in the wear mechanisms being observed (presented later in this section) and is indicative of a transition in wear behaviour exhibited by the PTA-SFFF Ti-TiB coupons, with the transition point being the 10 N normal load condition.

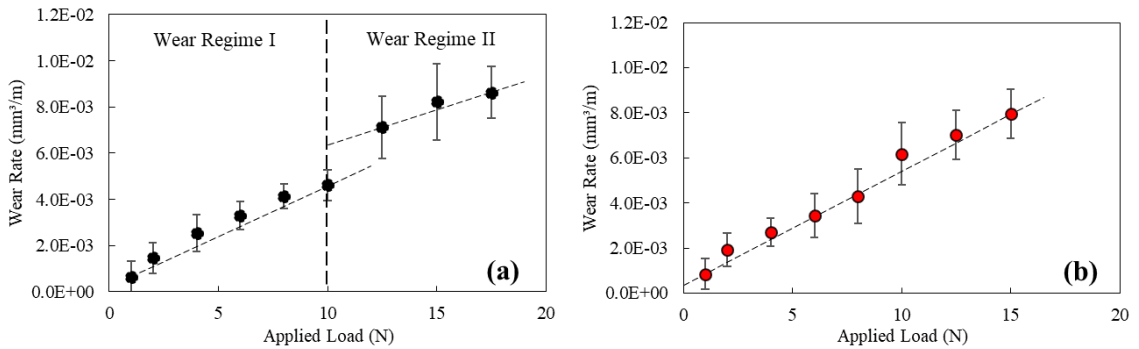


**Fig. 4.24.** Variation of volumetric wear rate as a function of applied load for the (a) untreated and (b) shot-peened PTA-SFFF Ti-TiB samples, collected from ball-on-disk style wear tests. Departure from linearity is observed at the 10N applied loading condition for the untreated samples while a consistent linear trend is observed in shot-peened samples.

For the shot-peened samples, volumetric and mass wear rates are shown in Fig. 4.24 (a) and Fig. 4.25 (b), respectively. For these samples, a linear trend is observed throughout both results. A slight departure from linearity is observed in the volumetric wear rate measurements past the 8N applied normal load in Fig. 4.24 (b) but is not considered with certainty an observed transitional wear behaviour point in the plot.

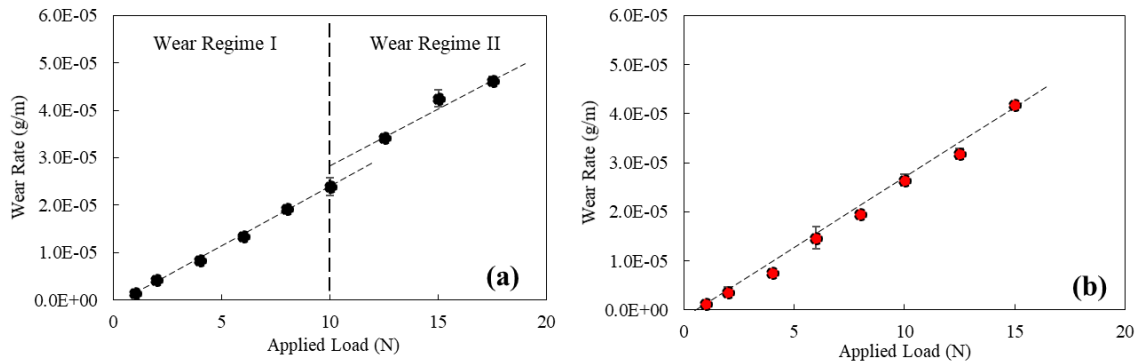


**Fig. 4.25.** Variation of mass wear rate as a function of applied load for the (a) untreated and (b) shot-peened PTA-SFFF Ti-TiB samples, collected from ball-on-disk style wear tests. Departure from linearity is observed at the 10N applied loading condition for the untreated samples while a consistent linear trend is observed in shot-peened samples.

Figure 4.26 shows the mass wear rates obtained from weighing the AISI 52100 counterface balls before and after testing for both testing schemes. Very low changes in mass were recorded from testing from the steel balls. A transition from mass gain to mass loss after the 10N applied normal load condition is observed from the untreated sample results in Fig. 4.26 (a) while this transition is observed to occur at a load of 6N from the shot-peened data set featured in Fig. 4.26 (b).

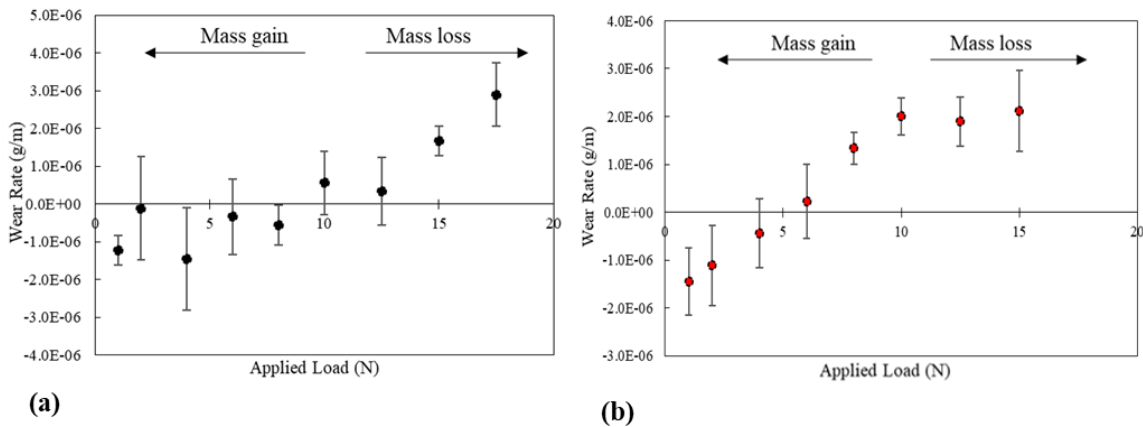


**Fig. 4.26.** Variation of mass wear rate as a function of applied load for the AISI 52100 counterface ball samples from the (a) untreated PTA-SFFF Ti-TiB wear testing and (b) the shot-peened PTA-SFFF Ti-TiB wear testing.

#### 4.4.2 SEM Observations of Worn Surfaces and Debris Particles

Figures 4.27-4.29 highlights the typical wear scar morphology and behaviour in the AISI 52100 counterface balls used against untreated PTA-SFFF Ti-TiB samples, exemplified through the 2, 10 and 17.5 N conditions. As noted in the previous subsection in Fig. 4.26(a), below the 10N applied normal force the steel balls were observed to have gain mass during wear testing. Below 10N, Ti material transfer to the wear balls was observed, with Ti oxides and small to coarse Ti platelets which piled-up at the rear of the wear scar along the sliding direction. This typical behaviour is shown in Fig. 4.27 for the 2 N condition. With increasing normal applied force in testing, detached and adhered Ti matrix platelets on the wear balls were observed to increase in size and number, comparatively shown in Fig. 4.28 for the 10 N condition ball. Furthermore, with increasing load, the wear scars exhibited a shift in circularity and became more oval shaped. Past the 10 N applied normal force, Fig. 4.26(a) highlighted mass loss during testing due to wear of the AISI 52100 balls. For these samples, as exemplified in Fig. 4.29 for the 17.5 N load, large Ti matrix platelets were found to have adhered to the surface and less oxidation debris adhered to the surface area was noted to have piled-up along the rear of the wear scar along the sliding direction. SEM equipped with EDS mapping (not shown) was used to analyze each of the wear scars and confirm the presence of Ti oxide and platelet on the steel balls.

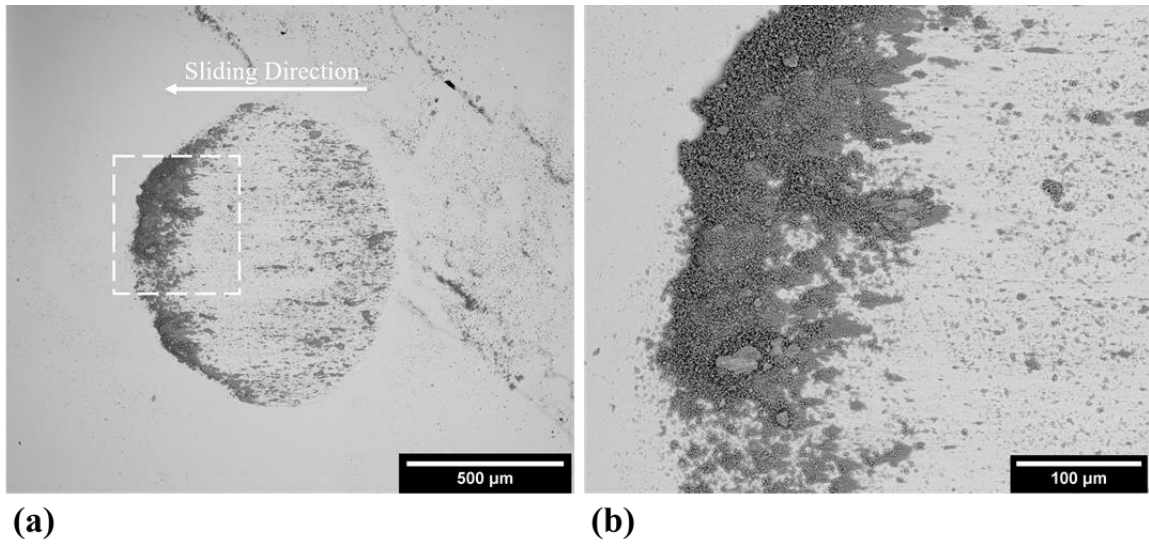


**Fig. 4.27.** BSE SEM images of (a) the wear scar of the AISI 52100 counterface ball for the 2N applied load untreated PTA-SFFF Ti-TiB sample, with an area size fitted to 0.634 mm<sup>2</sup>. (b) Shows Ti oxide and small platelet on the steel ball as a result of ball-on-disk wear testing against the untreated sample, taken from the area enclosed by the dashed white rectangle in (a).

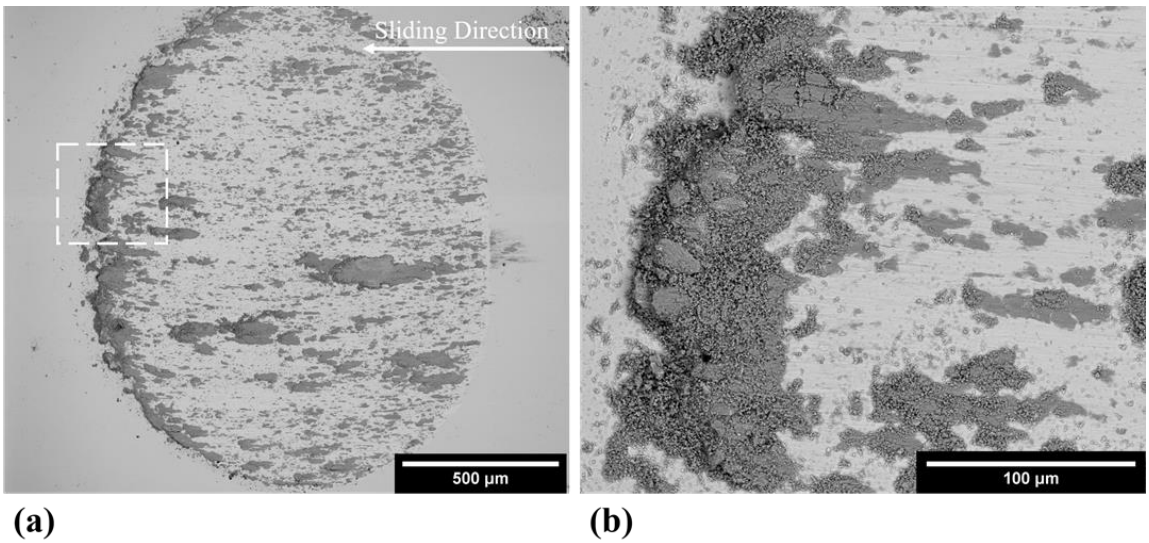


**Fig. 4.28.** BSE SEM images of (a) the wear scar of the AISI 52100 counterface ball for the 10N applied load untreated PTA-SFFF Ti-TiB sample, with an area size fitted to 1.629 mm<sup>2</sup>. (b) Shows Ti oxide and coarse platelet on the steel ball as a result of ball-on-disk wear testing against the untreated sample, taken from the area enclosed by the dashed white rectangle in (a).



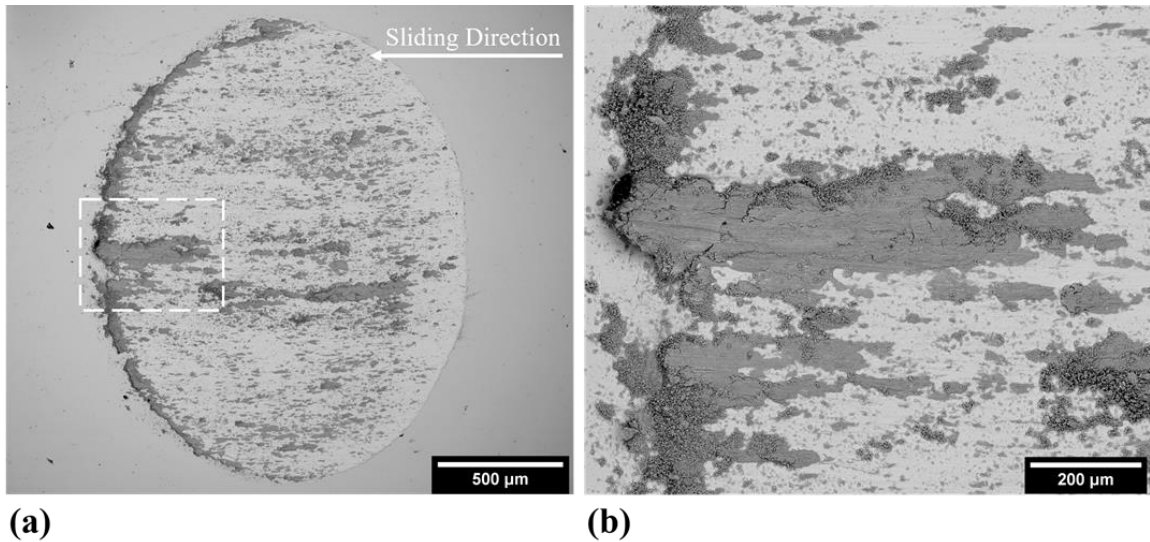


**Fig. 4.29.** BSE SEM images of (a) the wear scar of the AISI 52100 counterface ball for the 17.5N applied load untreated PTA-SFFF Ti-TiB sample, with an area size fitted to 2.149 mm<sup>2</sup>. (b) Shows Ti material transfer through large platelets, oxides, and Ti integration directly into the steel ball as a result of ball-on-disk wear testing against the untreated sample, taken from the area enclosed by the dashed white rectangle in (a).

Similar observations can be made with the AISI 52100 counterface balls used against the shot-peened PTA-SFFF Ti-TiB samples to the untreated samples. Figures 4.30-4.32 highlights the typical wear scar morphology and behaviour of the balls used for the shot-peened surfaces, exemplified also through the 2, 10 and 15 N conditions. As noted in the previous subsection in Fig. 4.26(b), below the 6N applied normal force the steel balls were observed to have gain mass during wear testing. Below 6N, Ti material transfer to the wear balls was observed, through the attachment of Ti oxide and small to coarse Ti platelets which piled-up at the rear of the wear scar along the sliding direction. This typical behaviour is shown in Fig. 4.30 for the 2 N condition. With increasing normal applied force in testing, larger detached Ti matrix platelets on the wear balls were observed to increase in size and number, comparatively shown in Fig. 4.31 for the 10 N condition ball. Furthermore, with increasing load, the wear scars exhibited a shift in circularity and became more oval shaped. Past the 6 N applied normal force, Fig. 4.26(b) highlighted mass loss during testing due to wear of the AISI 52100 balls. For these samples, as exemplified

in Fig. 4.32 for the 15 N load, large Ti matrix platelets were found to have adhered to the surface and less oxidation debris adhered to the surface area was noted to have piled-up along the rear of the wear scar along the sliding direction. SEM equipped with EDS mapping (not shown) was used to analyze each of the wear scars and confirm the presence Ti oxide and platelet on the balls. Overall, the shot-peened samples had slightly larger wear scar sizes on the steel balls as opposed to the untreated samples for the specific loading conditions tested.

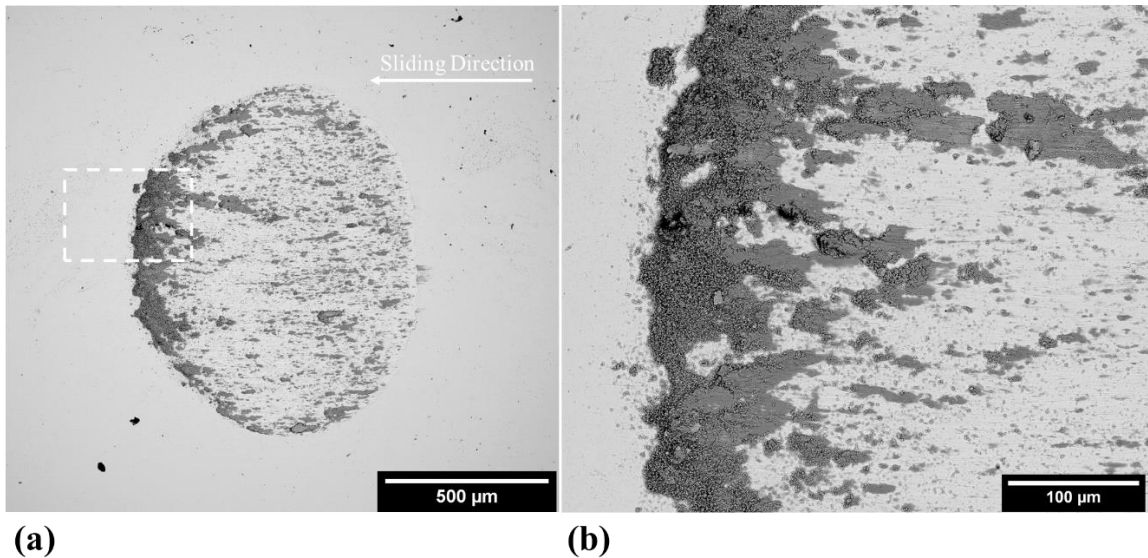


**Fig. 4.30.** BSE SEM images of (a) the wear scar of the AISI 52100 counterface ball for the 2N applied load shot-peened PTA-SFFF Ti-TiB sample, with an area size fitted to 0.716 mm<sup>2</sup>. (b) Shows Ti oxide and small platelet adhesion on the steel ball as a result of ball-on-disk wear testing against the sample, taken from the area enclosed by the dashed white rectangle in (a).

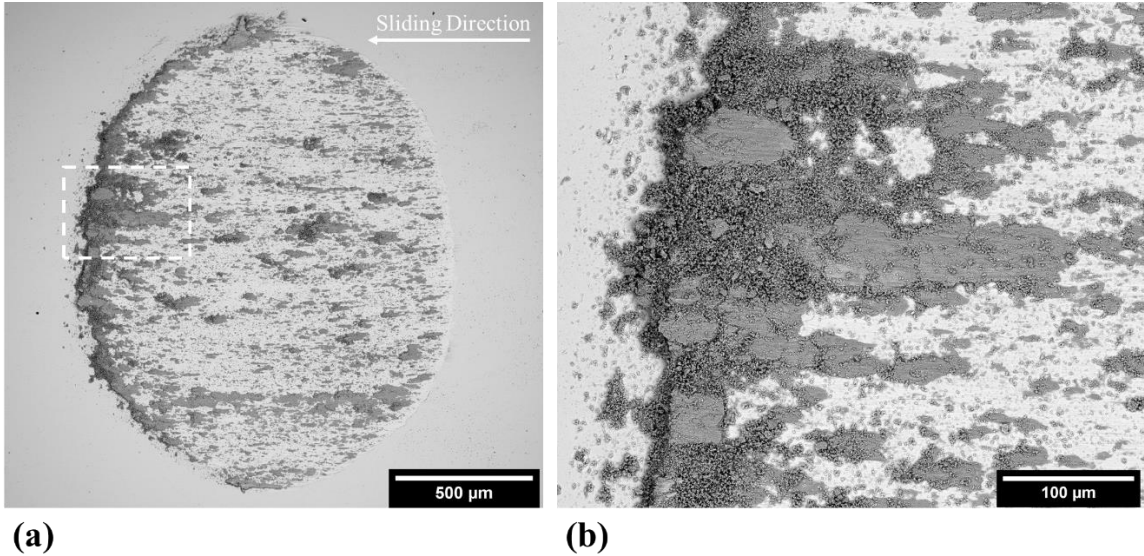


**Fig. 4.31.** BSE SEM images of (a) the wear scar of the AISI 52100 counterface ball for the 10N applied load shot-peened PTA-SFFF Ti-TiB sample, with an area size fitted to 1.855 mm<sup>2</sup>. (b) Shows Ti oxide and coarse platelet adhesion on the steel ball as a result of ball-on-disk wear testing against the shot-peened sample, taken from the area enclosed by the dashed white rectangle in (a).

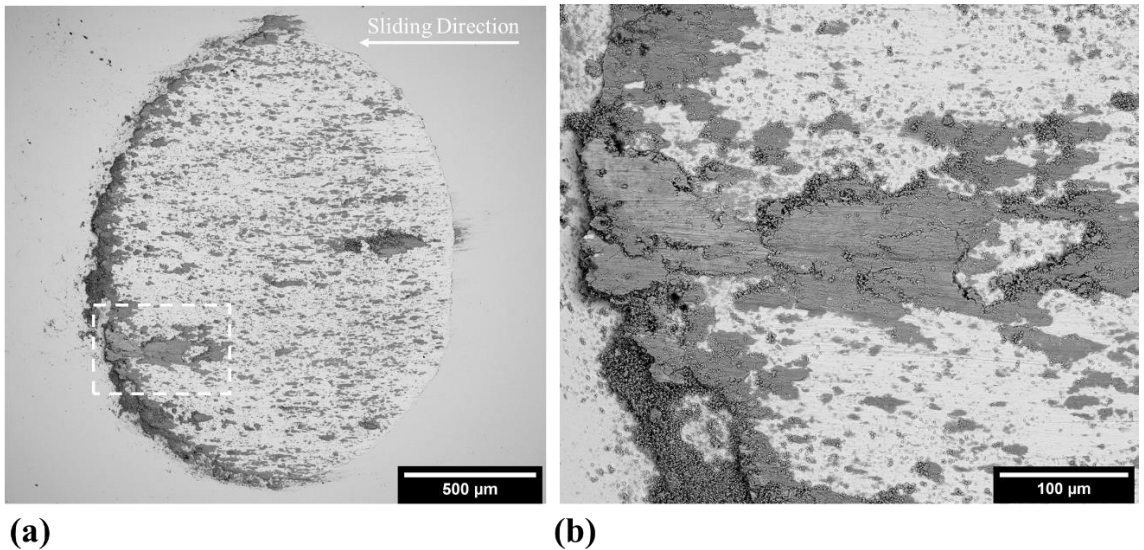


**Fig. 4.32.** BSE SEM images of (a) the wear scar of the AISI 52100 counterface ball for the 15N applied load shot-peened PTA-SFFF Ti-TiB sample, with an area size fitted to 2.057 mm<sup>2</sup>. (b) Shows Ti material transfer through large platelets, oxides, and Ti integration directly into the steel ball as a result of ball-on-disk wear testing against the shot-peened sample, taken from the area enclosed by the dashed white rectangle in (a).

The typical wear morphology of the worn surfaces of the untreated PTA-SFFF Ti-TiB samples in the identified Regime I ( $\leq 10$  N) and Regime II ( $> 10$  N) are shown in Figures 4.33-4.35. The wear tracks were formed by grooves parallel to the sliding direction made

by the AISI 52100 counterface balls and feature fine to large debris particles on the surface based on loading conditions. At low loading conditions ( $\leq 2$  N), such as the 1 N tested condition shown in Fig. 4.33, fine Ti oxide debris particles confirmed through EDS analysis were observed to have accumulated and adhered to the surface of the track while abraded regions were also noted, indicative of oxidation and abrasion wear mechanisms. With increased loading past 2 N, abrasion wear and oxidation wear were observed to dominate the wear mechanisms. Plastic deformation and material back-transfer wear mechanisms were also observed, as shown in Fig. 4.34 for the 8 N applied normal load condition. From observing the wear tracks exhibited past the 10 N applied normal loading condition, severe plastic deformation and the onset of delamination was observed. Furthermore, backscatter electron SEM imaging of the wear tracks with applied normal loading conditions past 10 N, such as that of the 12.5 N load sample wear track in Fig. 4.35, highlighted the frequent occurrence of bright spotted areas. EDS analysis found that these areas were composed primarily of iron, with chrome, oxygen, titanium, and trace amounts of boron, indicative of material transfer from the AISI 52100 ball to the wear track and the formation of MML in this higher load regime.

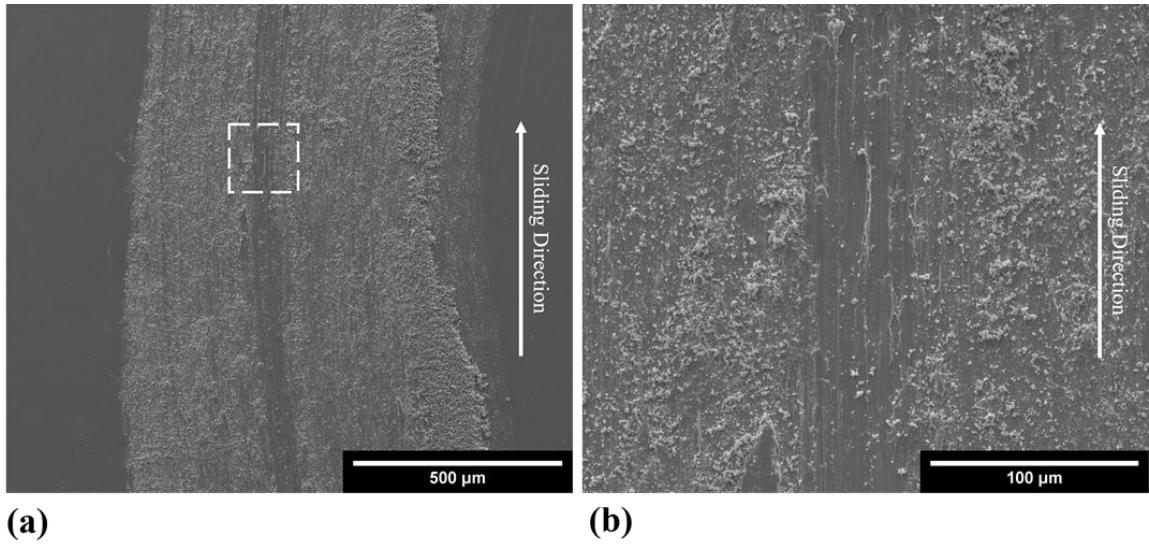


**Fig. 4.33.** SE SEM image of the 1N load untreated PTA-SFFF Ti-TiB wear track (a) showing fine oxide debris particles on the surface. (b) Higher magnification SE SEM imaging featuring surface abrasion towards the center of the track, taken from the enclosed white dashed rectangle in (a).

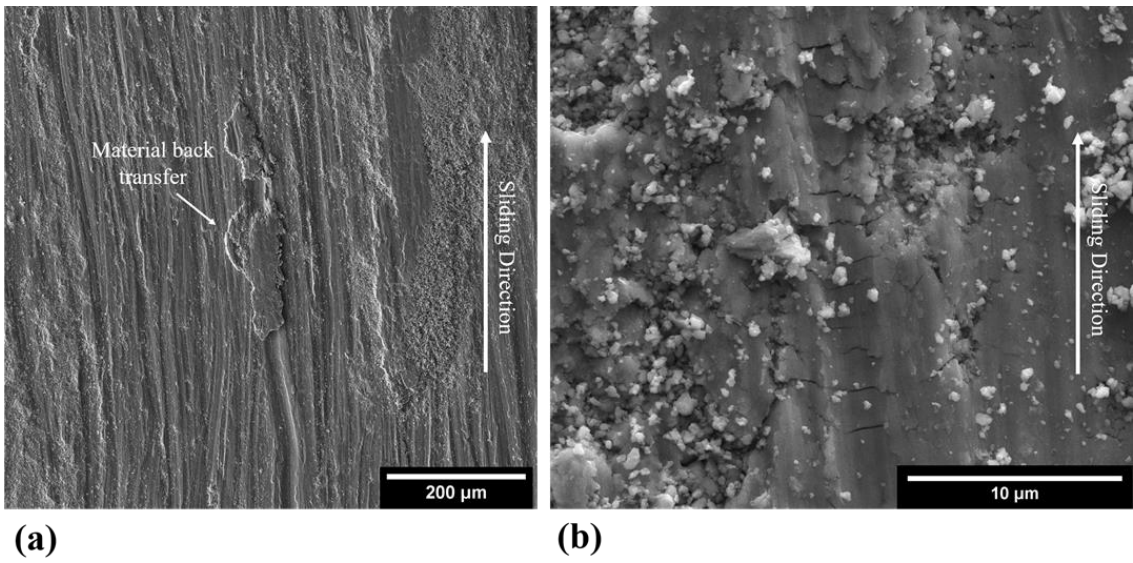


**Fig. 4.34.** SE SEM image of the 8N load untreated PTA-SFFF Ti-TiB wear track highlighting (a) material back-transfer on the track. (b) Higher magnification of a separate area directly in the centre of the track where wear fatigue cracks are observed with fine oxide particle debris featured on the worn surface.

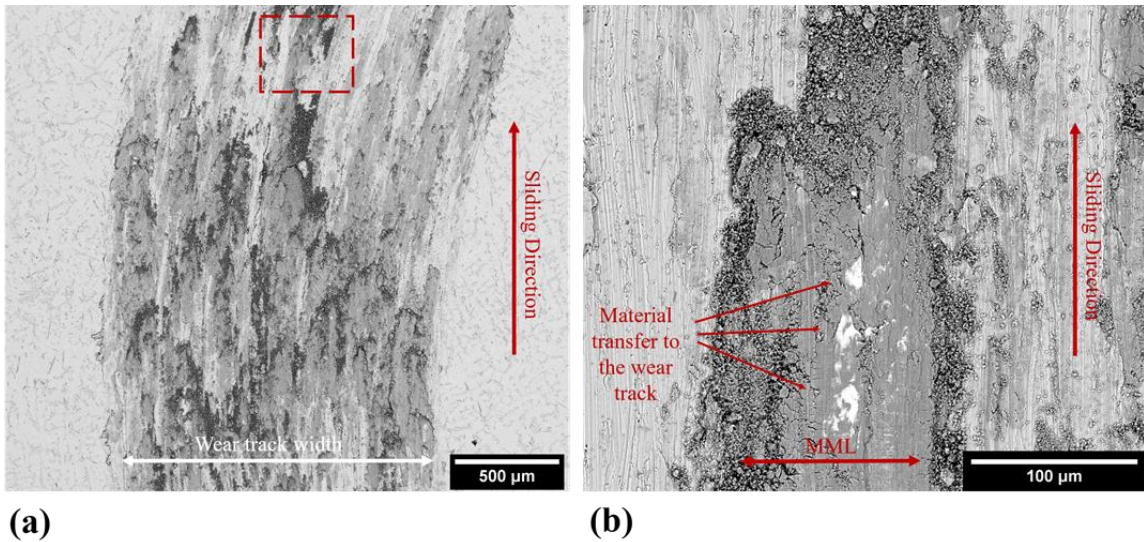


**Fig. 4.35.** BSE SEM images of the 12.5N load untreated PTA-SFFF Ti-TiB sample wear track (a) showing a portion of the wear track and (b) showing in greater detail the wear morphology of a smaller representative section of the track, taken from the red dashed box in (a). EDS elemental analysis detected that the bright white areas observed were composed dominantly of iron, with chrome, titanium, oxygen, and trace amounts of boron detected, indicative of material transfer from the AISI 52100 ball to the wear track as shown in (b).

With the shot-peened wear PTA-SFFF Ti-TiB samples, no clear wear transition point was observed throughout testing, though some similar trends in wear mechanisms highlighted in Figures 4.36-4.38 can be noted to the wear Regime I identified from the untreated samples. The wear tracks were formed by grooves parallel to the sliding direction made by the AISI 52100 counterface balls and feature fine to large debris particles on the surface based on loading conditions. At lower loading conditions, such as the 1N applied normal load wear track shown in Fig. 4.36, fine Ti oxide debris is noted covering the wear track while some abrasion scratches were identified, indicative of oxidation and abrasion wear mechanisms. With increasing load, signs of plastic deformation and material back-transfer wear mechanisms are noted, as seen in Fig. 4.37 for the 8N loaded surface. Material back-transfer from the steel counter face to the Ti wear track was noted as well in loading conditions past 8N, seen in Fig. 4.38 for the 10N sample, where bright white spots in the BSE were confirmed through EDS analysis to be primarily composed of iron, with chrome,



oxygen, titanium, and trace amounts of boron. Past the 8N applied loading condition, more severe plastic deformation was noted. Oxidation wear was found to be the dominant wear mechanism throughout testing; the formation of a coherent MMLs and their delamination was not found in higher loading testing scenarios.

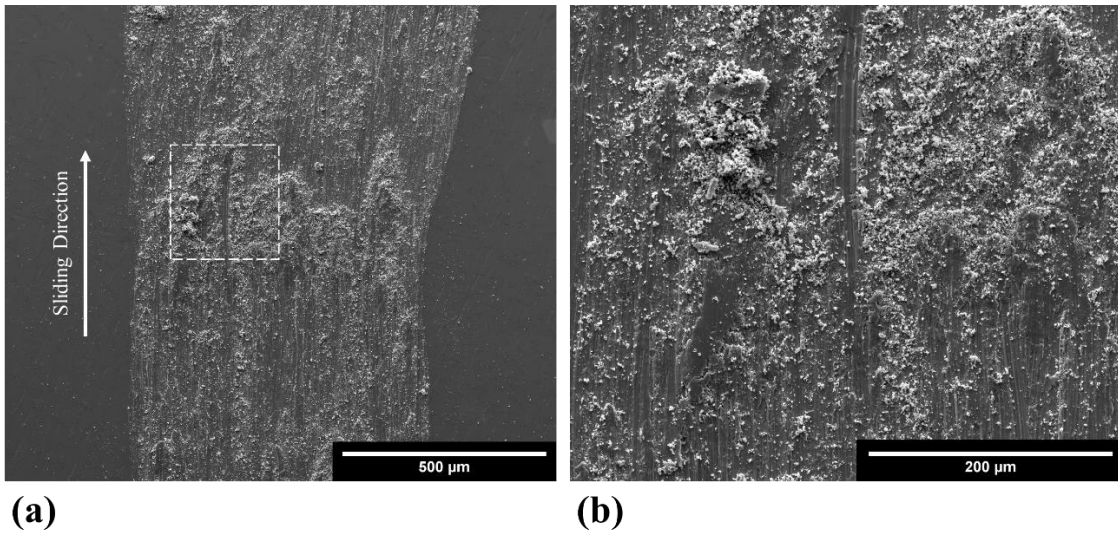


**Fig. 4.36.** SE SEM image of the 1N load shot-peened PTA-SFFF Ti-TiB wear track (a) showing fine oxide debris particles on the surface. (b) Higher magnification SE SEM imaging featuring surface abrasion towards the center of the track, taken from the enclosed white dashed rectangle in (a).

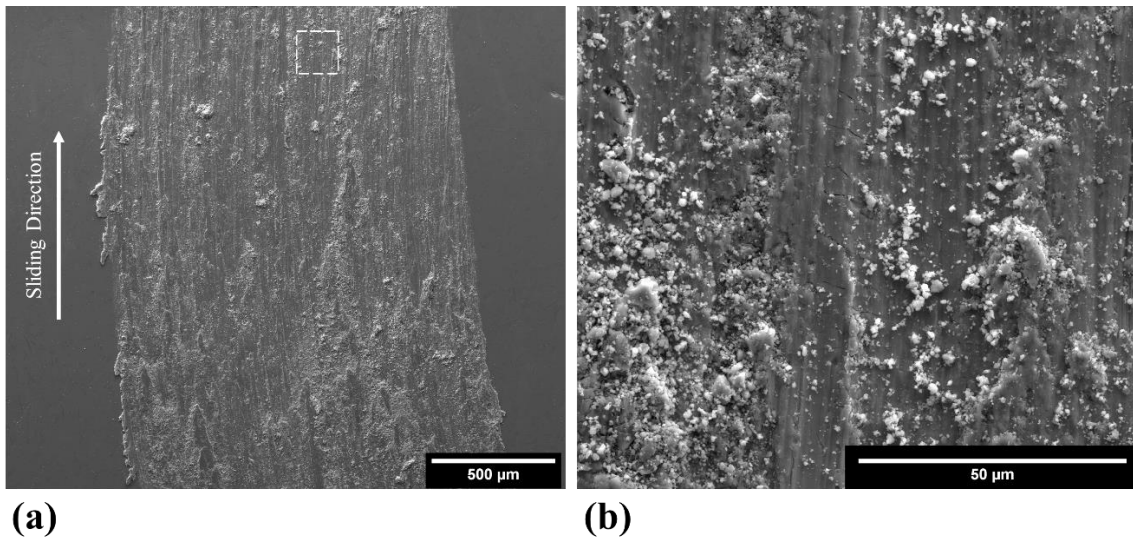


**Fig. 4.37.** SE SEM image of the 8N load shot-peened PTA-SFFF Ti-TiB wear track (a) showing fine oxide debris particles on the surface with abrasive tracks. (b) Higher magnification of the area in the enclosed white

dashed box in (a) where wear fatigue cracks are observed with fine oxide particle debris featured on the worn surface.

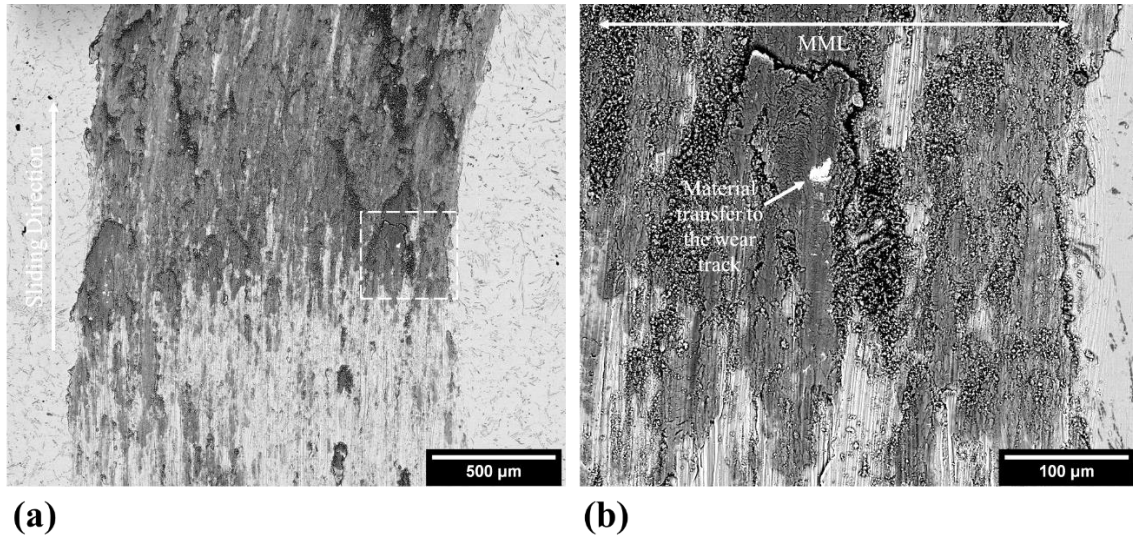


**Fig. 4.38.** BSE SEM images of the 10N load shot-peened PTA-SFFF Ti-TiB sample wear track (a) showing a portion of the wear track and (b) showing in greater detail the wear morphology of a smaller representative section of the track, taken from the white dashed box in (a). EDS elemental analysis detected that the bright white areas observed were composed dominantly of iron, with chrome, titanium, oxygen, and trace amounts of boron detected, indicative of material transfer from the AISI 52100 ball to the wear track as shown in (b).

Shown in Figures 4.39 and 4.40 are SE SEM images of wear debris particles collected from representative applied normal loading conditions for the untreated and shot-peened PTA-SFFF Ti-TiB wear testing, respectively. A clear shift in the debris morphology with increasing load is observed in both testing schemes. SEM and EDS spectra analysis found that debris particles at lower loads consisted of fine Ti oxide and agglomerate Ti matrix particles. In the higher load ranges, coarser Ti matrix debris platelets were noted with smaller wear debris and Ti oxides still present. At the high-end loading scenarios, 17.5N for the untreated samples and 15N for the shot-peened samples, evidence of severe plastic deformation is highlighted in SE SEM images (e) and (f) of Figures 4.39 and 4.40, which shows larger, grossly plastically deformed Ti matrix debris particles that were removed from the Ti coupon during wear.



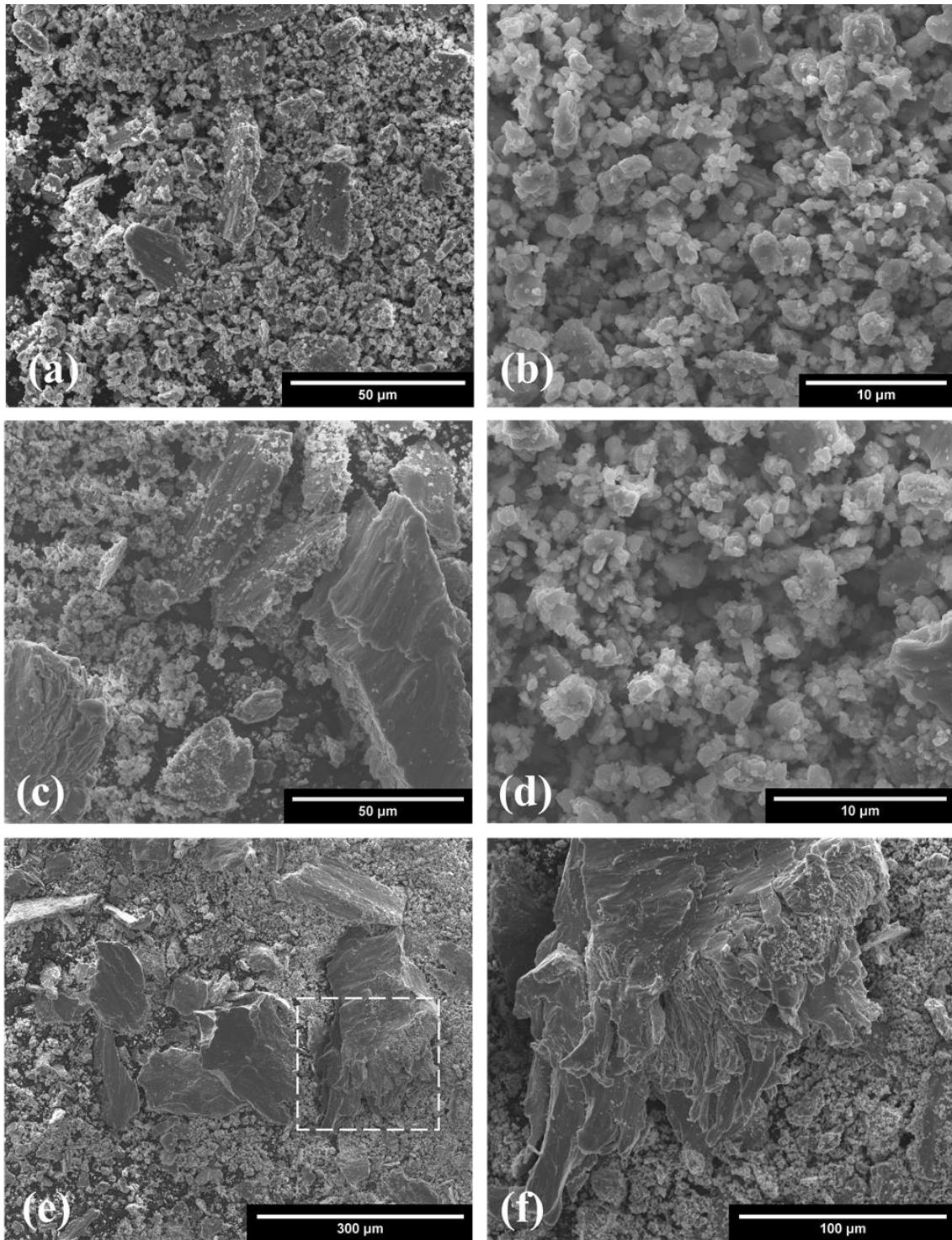


**Fig. 4.39.** Typical SE SEM images of wear debris particles collected during the untreated PTA-SFFF Ti-TiB wear testing. For the 1N applied load, (a) shows Ti oxide debris particles with some loose agglomerated matrix particles, and (b) shows at higher magnification the fine Ti oxide debris particles. For the 10N applied load, highlighted in (c) are coarse detached Ti platelet and agglomerated Ti debris particles, also with fine Ti oxide particles shown in (d). For the 17.5N applied load, (e) shows large detached Ti platelets with smaller wear debris and Ti oxides still present. (f) Highlights the severe plastic deformation of one of the large Ti debris taken from the enclosed dashed rectangle in (e).

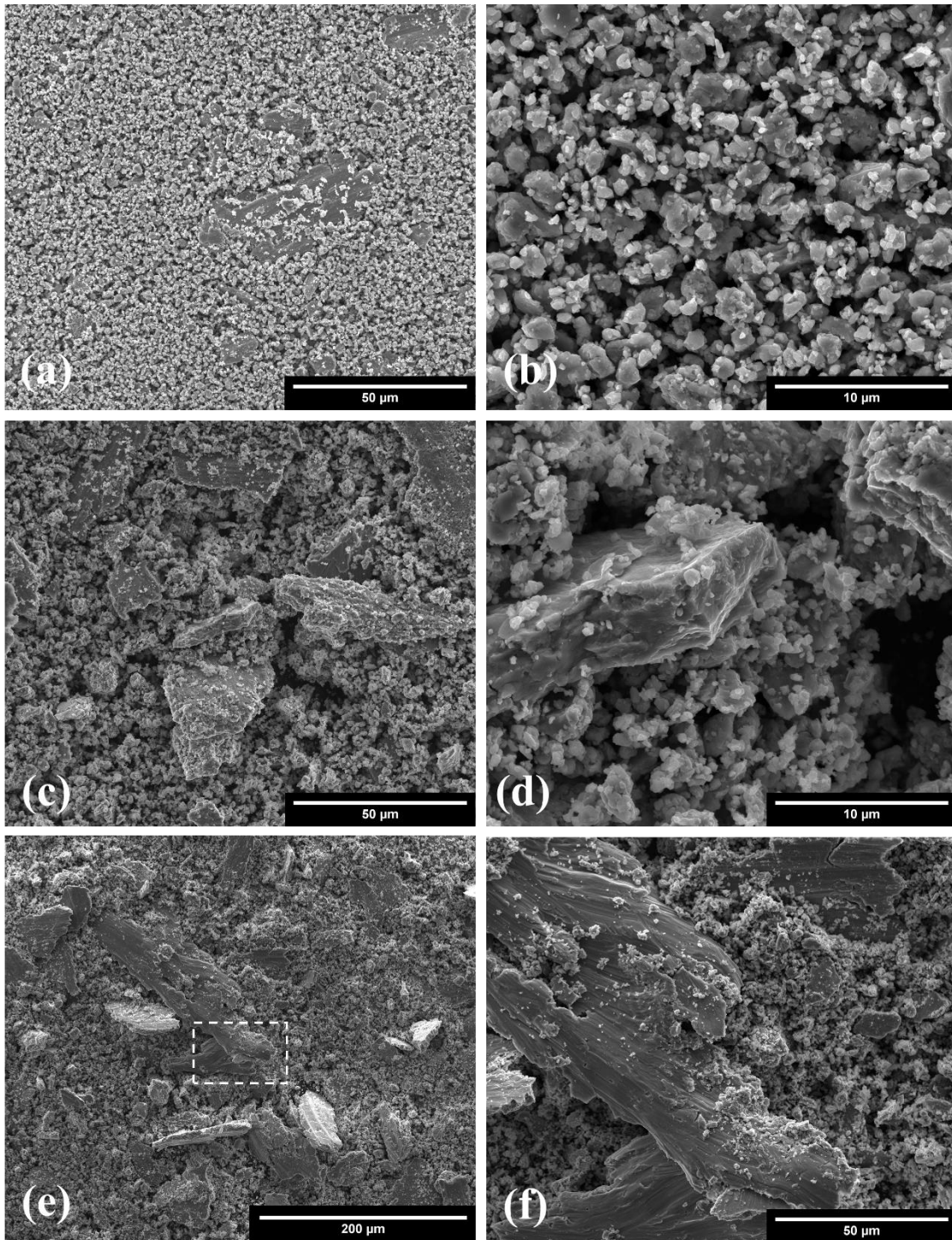


**Fig. 4.40.** Typical SE SEM images of wear debris particles collected during the shot-peened PTA-SFFF Ti-TiB wear testing. For the 1N applied load, (a) shows very fine Ti oxide debris particles, with some larger Ti particles present, and (b) shows at higher magnification the fine Ti oxide debris particles. For the 10N applied load, highlighted in (c) are coarse detached Ti platelet and agglomerated Ti debris particles, also with fine Ti oxide particles shown in (d). For the 15N applied load, (e) shows many large detached Ti platelets with smaller wear debris and Ti oxides still present. (f) Highlights the severe plastic deformation of one of the large Ti debris taken from the enclosed dashed rectangle in (e).

### 4.4.3 Subsurface Damage

Figure 4.41 shows the subsurface damage of the 17.5 N load untreated PTA-SFFF sample, highlighting the formation of a MML tribo layer observed through SEM. Figure 4.41(a) highlights onset delamination cracking behaviour of the formed MML and severe plastic deformation in the subsurface, seen through strain lines in the etched microstructure. Fractured TiB particles are observed in the subsurface region, which appear to have inhibited strain propagation. Figure 4.41(b) highlights at higher magnification the subsurface damage in the plastic deformation region, showing a TiB particle that is strained and fractured just below the MML. Through EDS elemental composition analysis, the formed MML was found to be composed of iron, chrome, oxygen, as well as Ti and trace amounts of boron.

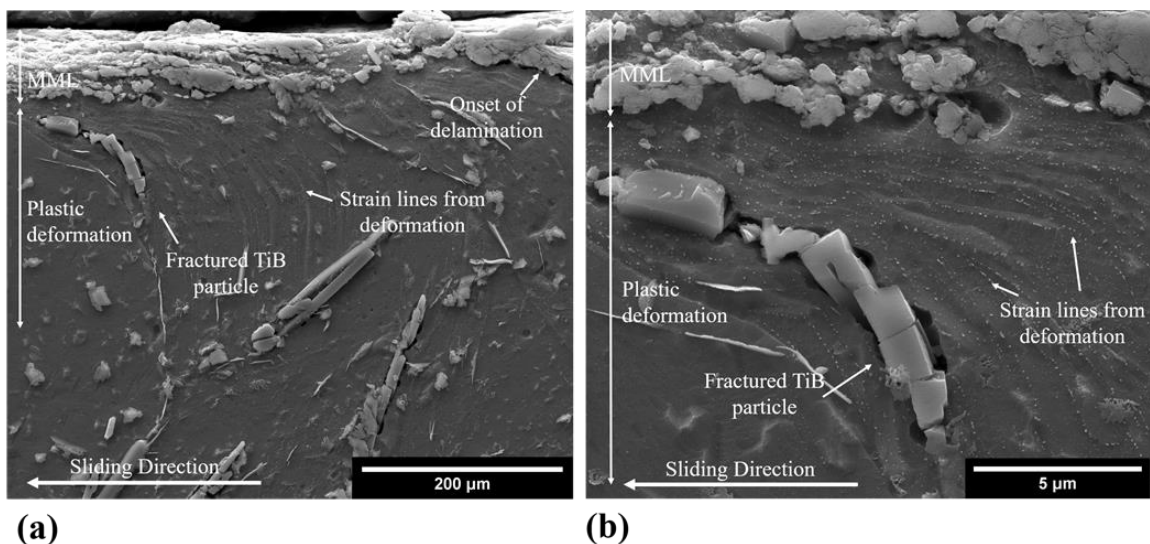


**Fig. 4.41.** (a) SE SEM image showing the subsurface damage present for the 17.5N PTA-SFFF Ti-TiB wear sample, etched with Kroll's reagent. (b) Highlights at higher magnification the subsurface damage in the plastic deformation region, showing a TiB particle that is strained and fractured just below the mechanically mixed layer (MML).

Figure 4.42 shows the subsurface damage of the 15 N load shot-peened PTA-SFFF sample, also highlighting the formation of a less coherent MML on the surface observed

through SEM. Figure 4.41(a) further shows the onset of delamination in the formed MML and severe plastic deformation in the subsurface, seen through strain lines in the etched microstructure. While MMLs were observed in the subsurface, they did not cover the whole wear track and exposed top surface is noted. Fractured TiB particles are observed in the subsurface region, which further appear to have inhibited strain propagation, though it is hard to say whether the particles broke during wear testing or from the shot-peening treatment. Figure 4.42(b) shows at higher magnification the subsurface damage in the plastic deformation region, showing a TiB particle that is strained and fractured just below the surface. Through EDS elemental composition analysis, the smaller formed MML was found to be composed of iron, chrome, oxygen, as well as Ti and trace amounts of boron. Cross-hatched subsurface microstructural shot-peened features as presented in section 4.2 were not evidently observed in the subsurface, though subsurface strain lines are reminiscent of the 45° cross-hatched features.

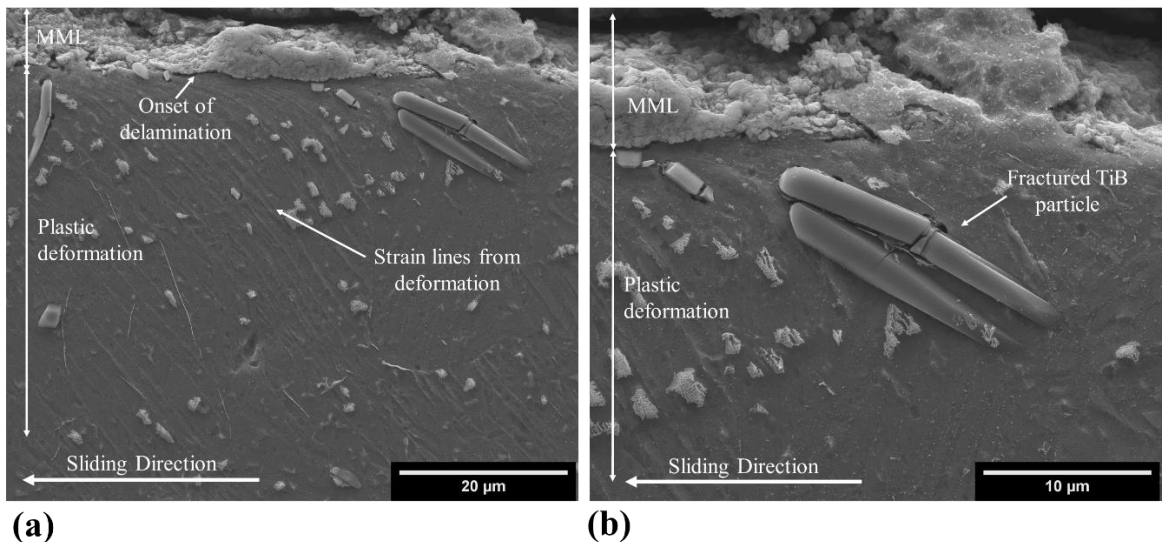


**Fig. 4.42.** (a) SE SEM image showing the subsurface damage present for the 15N PTA-SFFF Ti-TiB shot-peened wear sample, etched with Kroll's reagent. (b) Highlights at higher magnification the subsurface damage in the plastic deformation region, showing a TiB particle that is strained and fractured just below the mechanically mixed layer (MML).

To further understand the subsurface damage in the 17.5 N untreated sample and the 15N shot-peened sample, the equivalent plastic strain in the subsurface is estimated from the tangent of the deformed microstructure strain line features observed, shown schematically in Fig. 4.43(a), using the following equation:

$$\varepsilon_{equivalent} = \frac{\sqrt{3}}{3} \tan \theta \quad (8)$$

Where  $\theta$  is the angle formed between the tangent of the strain line and a reference vertical line and  $\varepsilon_{equivalent}$  is the equivalent plastic strain [120]. Three strain lines appearing at the same depth are taken into consideration for each sample in these calculations and the variation of the average equivalent plastic strain with respect of depth from the top surface is plotted in Fig. 4.43(b). Of the two samples analyzed, the 17.5N untreated samples experienced much lower equivalent strain values than the 15N shot-peened sample. For both conditions, the PTA-SFFF Ti-TiB samples experienced comparable equivalent plastic strain values for the given higher load capacity in reference to both Ti-10V-2Fe-3Al and Ti-6Al-4V alloys analysed in the similar works investigated by Farokhzadeh and Edrisy [21], whose equivalent strain values were evaluated at lower values of 5 N and 0.8 N applied normal conditions.

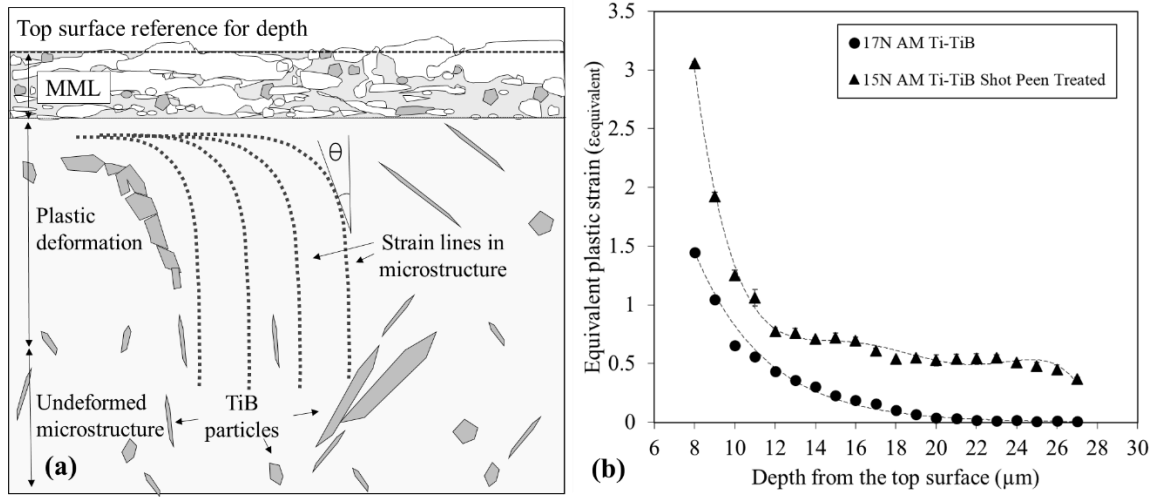


**Fig. 4.43.** (a) Schematic developed from Fig. 4.41(a), highlighting the procedure used to measure the equivalent plastic strain from the subsurface of the 17.5N untreated and 15N shot-peen treated PTA-SFFF Ti-TiB samples, using strain lines in the microstructure in analysis to refer to. (b) Variation of the average equivalent plastic strain with respect of depth from the top surface of each sample (MML: mechanically mixed layer).

## CHAPTER 5: DISCUSSION

The following sections overview and discuss the results obtained during this research investigation and how they reflect to the related objectives of the study. This chapter is subdivided into two main sections. In the first section, the mechanical behaviour of the as-received Ti-TiB PTA-SFFF material is explored, with a focus on the influence of the AM build metallurgy through tensile directional behaviour as well as fatigue behaviour. Furthermore, the influence that shot peening had on fatigue behaviour is discussed. The second section moves to discuss the tribological behaviour of the Ti-TiB structure based on ball-on-disk wear testing and explores the effect that shot peening had on wear behaviour. Reflections related to the microstructure features of the material, notably the TiB particles present and the influence of shot-peening, are made throughout to explain the behaviour patterns noted in both sections.

### **5.1 Mechanical Behaviour of the Ti-TiB PTA-SFFF Material**

From the directionally oriented tensile testing results obtained summarized in Table 4.6 and shown graphically in Fig. 4.14, a near-isotropic behaviour within the as-received AM block structure was observed, despite AM layering strategies used to produce parts seen in literature presented. The core tensile results shown in Table 4.6 feature low standard deviation values for obtained results in the three directions considered. This near-isotropic behaviour in samples can be partially attributed to the fully dense build of the PTA-SFFF blocks as well as the indistinguishable AM bead boundary interface within the structure which shows good fusion between layers. Additionally, TiB particles were observed to be homogeneously distributed and to have no directional dependence on orientation based on

AM deposition which would have influenced directional testing. This was shown quantitatively in particle analysis utilizing the ImageJ software to investigate micrographs from the longitudinal and lateral directions, as summarized in Table 4.2 and Figures 4.3 and 4.4. Based on the similarity of the values presented which describe the size of the TiB particles and their distribution in the matrix, negligible differences in distribution are noted based on the AM build strategy. Furthermore, from fractographic studies of the tensile fracture surfaces, samples were primarily dominated by ductile fracture mechanisms despite TiB additions. Tensile testing results highlight that they had sustained ductility in all directions measured through percent elongation and percent reduction in area, with average values of  $8.9 \pm 1.1 \%$  and  $8.0 \pm 1.2 \%$ , respectively, as presented in Table 4.6.

In reviewing the fatigue behaviour of the PTA-SFFF Ti-TiB material, rotating-bending fatigue tests found that the highest stress at run-out was  $282.5 \pm 5.4$  MPa. Based on the results obtained from the S-N fatigue life curve, the fitted endurance limit of the material was found to be  $247.8 \pm 5.4$  MPa. As discussed in the result section, when observing the fractographic results of failed fatigue surfaces, three distinct fracture regions were identified: Region I, Region II, and Final Rupture. Generally, the Final Rupture regions were ductile in nature, with dimples presented throughout the region, while crack initiation and initial propagation zones were flat with observable cleavage steps and facets thus dominated by brittle fracture mechanisms. Similar features were observed in the low and high cycle fatigue regimes as well, with the differences between the two being with decreasing stress amplitude, the size of Region I and II were observed to increase in area while the Final Rupture zone decreased.



For the PTA-SFFF Ti-TiB samples, the majority of the fatigue samples studied in this research had cracks which initiated at the surface or near surface due to surface defects from fatigue sample preparation, which highlights goodness of the AM build due to its low porosity. Process inheritance defects have a tendency to be detrimental for titanium AM manufactured samples undergoing cyclic loading scenarios, as highlighted in the works of Wycisk et al. [121] with laser sintered Ti-6Al-4V, where fatigue failure initiated at process-related pores and other defects within samples. Previous work [122] from this research group highlighted that this AM Ti-TiB produced material had a porosity of 0.913% determined using Archimedes method. Throughout microstructure review, no pores/voids within the structure, no gaps between Ti and TiB, and no unmelted zones from AM processing were observed throughout microstructure review, from the micro to macro level. High-magnification observations made through FIB and TEM in observing the microstructure and distribution of TiB particles showed that the Ti and TiB interfaces were coherently formed. This is shown in Figures 4.5-4.6 of Ti-TiB interface boundaries in TEM and HR-TEM as well as in the line scan work representatively shown in Fig. 4.8, which shows a smooth transition from Ti to TiB in TEM, with no observable gaps between the two.

As mentioned, TiB particles were found to be nearly homogeneously distributed throughout the structure. However, occasional TiB clusters or agglomerations could be observed throughout the samples studied. Figure 5.1 exemplifies instances where TiB was seen to accumulate in higher density in isolated areas within the structure, where an example of large and small TiB clusters observed are shown.

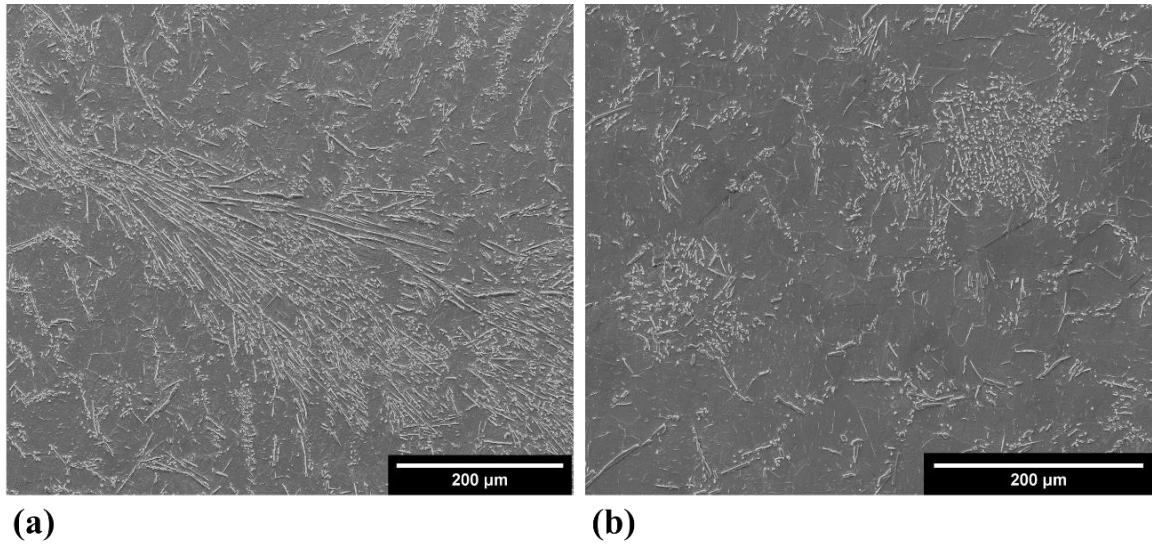


**Fig. 5.1.** SE SEM images of the PTA-SFFF Ti-TiB structures showing TiB (a) large and (b) small agglomerations in the structure.

It is possible that these localized TiB clusters within the structure may have also further influenced results found throughout this investigation, leading to some of the variability observed. Detrimentally, many researchers [7], [54], [55] have found that there is a tendency for TiB whisker clusters to form in localized areas, which may impact mechanical properties of samples and act as stress concentrators as well as crack nucleation sites. Lu et al. [51] found in failure analysis that dislocation pile up would occur at the ends of TiB particles with applied stress, leading to voids to initiate and grow at these locations and potential fracture.

Figure 4.19 (b) showed for one fatigue sample, which was tested at a stress amplitude of 432.5 MPa and failed at 24600 cycles, fatigue crack initiation occurred at an isolated area at the surface where TiB particles were described to be somewhat agglomerated. This could be described as an instance where TiB particle agglomerations acted as stress concentrators and may have led to early onset fatigue crack initiation in the tested sample. However, apart from that fatigue specimen, all other crack initiation sites

observed occurred at localized surface defects where TiB was not detected through EDS analysis. In fractography, TiB particles were observed to stay coherent within the structure, even after fracturing, with no particle pull-out observed. This highlights a strong interfacial bond between Ti-TiB in samples.

Furthermore, TiB particles in the PTA-SFFF material can be described as fine in size, being on average 1.5  $\mu\text{m}$  in width and 4.5  $\mu\text{m}$  in length as found from TiB distribution analysis results. In size, these particles are similar to those studied by Emura et al. [77] in Ti-22Al-27Nb, which they found to lead to improved fatigue strength and dislocation obstruction. They found that smaller TiB particles led not only to classically observed composited strengthening effects but also to grain refinement and dislocation movement blocking. The works of Shufeng et al. [7] found that fine TiB needles with high aspect ratios would act as stress concentrators in fatigue, ultimately blocking crack movement and eventually leading to TiB rupture. However, they found that TiB particles retained interfacial bonding to the Ti matrix after fracture. In fractography analysis of PTA-SFFF Ti-TiB fatigue failure surfaces, the fine TiB particles were observed to keep their retention within the Ti matrix, even after failure, showing similar fatigue improvement influences as presented in the works of Shufeng et al. and Emura et al..

In discussing the influence of shot peening on fatigue, the shot-peening treatment described paired with mild grinding and polishing to reduce surface roughness was observed to lead to drastically improved fatigue behaviour for the Ti-TiB PTA-SFFF material. In comparing the untreated and shot-peened conditions as presented in Fig. 4.17 through the S-N fatigue life curves, the shot-peened fatigue samples showed a much higher  $10^7$  high-cycle fatigue strength with highest value of  $332.5 \pm 5.4$  MPa versus  $282.5 \pm 5.4$

MPa for the untreated samples and overall throughout testing outperformed the untreated samples. The improved fatigue behaviour of shot-peened samples is attributed to the introduced compressive residual stresses which led to localized increases of hardness at the surface of parts and stress-induced cold worked microstructural changes, as shown in the microhardness profiling featured in Fig. 4.10 and etched subsurface SEM images in Fig. 9. The localized increase in hardness and related microstructural cold-work changes made crack initiation harder to occur at the surface of shot-peened parts, as it occurred at in untreated samples, despite their slightly rougher surface finish even after polishing in comparison untreated fatigue samples.

Crack initiation sites for shot-peened samples, shown in Figures 4.20 and 4.21, were found to be approximately situated between 0.7 to 1.5 mm in the subsurface of samples. This is directly relevant to the influence of the shot-peening process. The works of Petit-Renaud [34] highlights that shot-peening introduces high amounts of compressive residual stress at or just below a shot-peened surface, which is balanced by smaller amounts of tensile stress below this compressive stress layer, as shown in Fig. 2.3. The observable depth of the crack initiation sites in samples are similar to where the influence of surface hardening stops being experienced, as observed in the trend presented in the microhardness profile in Fig. 4.10. Thus, crack initiation sites are believed to have occurred outside of the compressive residual stress layer introduced in samples, in the tensile stress balanced region. The formation of voids around crack initiation sites could also be explained by the presence of tensile stresses in the structure, as numerous isolated voids were not observed at crack initiation sites of untreated fatigue samples and were not observed throughout fracture surfaces.

It is important to note that untreated and shot-peened samples showed similar fracture failure mechanisms in Region I, Region II, and the Final Rupture region. However, differences between the two sample types remain that the fatigue crack initiation sites as discussed occurred at different locations and the presence of cross-hatched micro-cracking fracture surface features were observed specifically at the near-subsurface of shot-peened samples. This cross-hatched micro-cracking fracture surface behaviour, exemplified in Fig. 4.20 (c), can be explained due to the microstructural changes in shot-peened samples from the introduced surface treatment process. Shot-peening was noted to result in microstructural twinning and cross-hatched features in the near-subsurface of the material, highlighting shear deformation in the subsurface, featured in Fig. 4.9. This cross-hatching resembles the hatched micro-cracking fracture feature described and is associated to a brittle-like, transgranular fracture mechanism within the residual compressive stress layers introduced through shot-peening.

## **5.2 Tribological Behaviour of the PTA-SFFF Ti-TiB Material**

In this work, the tribological behaviour of as-received PTA-SFFF Ti-TiB samples were evaluated through ball-on-disk rotational testing. Various aspects highlighted from the results section indicated a change in wear behaviour past the 10 N applied normal loading condition, indicating transitional behaviour in the samples studied. This was first indicated by the departure from linearity in the change from the volumetric and mass wear rates (Fig. 4.24(a), Fig. 4.25(a)) of the PTA-SFFF Ti-TiB coupons as well as the change in mass wear rate from mass gain to mass loss (Fig. 4.26(a)) in the AISI 52100 steel counterface balls, all occurring at about 10 N. This was further highlighted by the change in wear behaviour observed through SEM and EDS analysis (Figures 4.27-4.29 & Figures

4.33-4.35) as well as from the change in morphology of debris particle collected during testing (Fig. 4.39). Thus, two wear regimes are noted at low ( $\leq 10$  N) and high ( $> 10$  N) loads during the testing, with a transition at the 10 N applied load.

At low loads ( $\leq 10$  N), dominating wear mechanisms observed in the lower load wear regime appear to be oxidative wear, accompanied by light abrasive wear, highlighted from SEM observations featured in Figures 4.33 and 4.34. Figure 4.33 shows at lower loads in this regime ( $\leq 2$  N) limited abrasive wear and plastic deformation was observed and the wear mechanisms was dominated solely by oxidation wear, while past 2 N, plastic deformation and abrasion wear were observed (Fig. 4.34). In this wear regime ( $\leq 10$  N), weight gain of the AISI 52100 balls was further observed (Fig. 4.26(a)), caused by Ti material transfer to the counterface balls. Figures 4.27-4.29 show fine oxides and small Ti platelets adhering to the surface of the balls at lower loads, while as loading increases, an increase in size and distribution of the adhered platelets was noted.

At high loads ( $> 10$  N) transition in wear mechanisms was observed as the formation and onset of delamination of the tribolayer was noted. The tribolayer, or MML, consisted of harder TiB particles and Ti and Fe oxides mixed into a severely deformed Ti matrix. The subsurface image of 17.5N applied load wear sample in Fig. 4.41 shows this MML at the top surface and highlights micro-voids and cracking just below the layer. As described in the works of Farokhzadeh and Edrisy [21] in the evaluation of the dry-sliding ball-on-disk wear behaviour of Ti-10V-2Fe-3Al and Ti-6Al-4V, micro-voids and cracking of the MML are precursor elements to delamination of tribolayers and severe wear for Ti alloys. Thus, while severe wear was not captured in the 1-17.5N applied loading testing scheme of this study, as onset delamination behaviour was observed, it is suspected that in higher

applied loading scenarios the tribolayer would start to fully delaminate and severe wear would occur in testing due to crack formation and propagation in the subsurface below the MML.

As highlighted from SEM observations exemplified in Fig. 4.35, oxidative and abrasive wear mechanisms were further observed at higher loads. In this wear regime ( $>10$  N), weight loss of the AISI 52100 balls was noted (Fig. 4.26(a)), which suggests that the balls themselves were worn down during testing at these higher loads and that the dynamic surface interactions between the PTA-SFFF Ti-TiB coupons and AISI 52100 balls changed. Hard, fractured TiB wear debris were formed in this higher load regime and resulted in wearing of the steel counterface balls through abrasion. From Fig. 4.24 (a) & Fig. 4.25 (a) showing volumetric and mass wear rates of samples, while wear rates were observed to have increased with increasing load, after the transitional 10N loading condition, the slopes of the wear rate plots were observed to decrease in value in the higher load regime. From Fig. 4.23, average COF values are further observed to decrease with increasing load. This may be attributed to the surface evolution of the wear tracks and the formation of MMLs.

Overviewing the subsurface damage of the 17.5 N load sample, the formed MML are observed along with severe plastic deformation and TiB particle fracture (Fig. 4.41). Overall in wear testing, TiB particles were observed to stop strain propagation within the subsurface, bending and then fracturing in the subsurface during applied loading while remaining coherent within the structure, shown in Fig. 4.41. During applied stress, discontinuous TiB particles within a Ti matrix tend to deform elastically as ceramics while the Ti matrix, possessing higher ductility, will experience plastic deformation [123].

Observing strain lines in the subsurface, TiB particles seem to act as mitigators to strain propagation, with the strain line continuous group behaviour getting disrupted by the presence of TiB particles and stopping strain propagation in the matrix (Fig. 4.41). In the centre of Fig 4.41(a), one TiB particle is seen fractured in half, cleaved parallel to the sliding direction. Strain lines are observed grouped above the fractured particle though not below it, highlighting the mitigation of strain in the subsurface through the presence of these TiB particles. As a stiffener and strengthening reinforcement particle, additions of TiB can lead to ductility losses, though in low concentrations minimal ductility losses would be expected [123], [124].

In reviewing hardness results, the as-received samples were found to have a Rockwell HRC hardness of  $23.7 \pm 0.6$  HRC and a Vickers microhardness of  $303.1 \pm 22.5$ . When discussing the nano-indentation hardness values and the recorded reduced moduli of elasticity obtained in this work, consistent values were observed in the 1-3 mN loading condition range, making it acceptable to use averaged measurement results and to report the reduced modulus of elasticity and nanohardness to be  $124.58 \pm 7.90$  GPa and  $4.49 \pm 0.32$  GPa, respectively. Similar nanohardness values and reduced modulus of elasticity values were able to be produced through the PTA-SFFF process using less boron added in comparison to SLM CP Ti samples studied by Attar et al. [68]. Using ratios between nanohardness and reduced modulus of elasticity values, ratios of  $H/E_r$  and  $H^3/E_r^2$  are calculated as an indication of wear resistance are 0.036 and 0.006 GPa, respectively.

In contrast to fatigue testing, the described shot-peening treatment paired with mild grinding and polishing did not lead to drastically different numerical results in wear testing such as COF values and wear rates. From the untreated to treated conditions, a maintained



wear resistance was observed in shot-peened samples, with similar numerical results such as wear rates and COF values in wear testing noted though different wear mechanisms observed, as discussed in the following paragraphs.

Comparing COF results from the two sample types, Figures 4.22 and 4.23 show that the two have very similar trends in averaged COF values obtained for the same loading conditions and that trends in the break-in and steady state areas for COF versus distance were similar as well. The values obtained from volumetric and mass wear rates for the shot-peened samples (Fig. 4.24(b) and Fig. 4.25(b)) in comparison to the untreated samples (Fig. 4.24(a) and Fig. 4.25(a)) were comparable as well, with almost the same numerical values obtained in both testing schemes. One key difference between the two samples remains the 10N wear transition point in the untreated samples, which was not found for the shot-peened samples. Shot-peened samples had a linear trend in both volumetric and mass wear rate graphs (Fig. 4.24(b) and Fig. 4.25(b)). Moreover, while for the mass wear rates of the AISI 52100 steel balls were observed to transition from mass gain to mass loss at 10N for the untreated Ti-TiB coupons, this was observed to occur at 6N for shot-peened Ti-TiB coupons.

From the SEM observations of the worn surfaces and debris particles collected from testing, similar trends in worn AISI 52100 steel balls and coupons were observed throughout loading for the untreated and shot-peened coupons, exemplified in Figures 4.36-4.38. Throughout testing, samples were dominated by oxidation wear mechanisms. This is attributed to the higher hardness, compressive residual stresses in the subsurface, and thus higher surface energy in these samples which would have contributed to faster oxidation wear rates. Plastic deformation and abrasion wearing mechanisms were noted at

the higher end of the loading conditions, though were not as prominent as oxidation wear. Unlike with the untreated samples, material back-transfer from the steel ball was observed onto the Ti-TiB shot-peened wear track at earlier loads of 8N through EDS analysis. This is expected as AISI 52100 steel balls were observed to transition from mass gain to mass loss at the 6N load for the shot-peened tests. When comparing the morphology of the wear debris obtained throughout testing, similar trends were noted, though it is clear when comparing the results of the untreated samples (Fig. 4.39) and shot-peened samples (Fig. 4.40) that finer, Ti-oxide debris were obtained in shot-peened testing at low loads. Moreover, through EDS mapping, the wear tracks of the shot-peened samples were found to have higher amounts of oxygen present on the track than untreated samples, which highlights that oxidation wear mechanisms played a more dominant role throughout testing in shot-peened samples.

From these discussions, transitional wear behaviour was not noted while observing the counterface surfaces from shot-peened samples. When comparing the subsurface of the untreated 17.5N tested wear sample (Fig. 4.42) to that of the 15N tested shot-peened wear sample (Fig. 4.41), the MML formed on the 17.5 N untreated sample is coherent and covers the top surface while the MML of the 15N shot-peened sample is small and exposed top surface of the wear track is seen. The dominant oxidation wearing mechanisms in shot-peened samples is suspected to have impeded the formation of a coherent MML in samples through the quick removal of oxides formed instantaneously on the surface. When comparing the values of equivalent strain plotted in Fig. 4.43 (b), the 15N shot-peened sample has higher equivalent strain values obtained than the untreated sample tested at 17.5N. It would be expected that due to the higher hardness of the subsurface of the shot-

peened sample, subsurface shear deformation would be less pronounced than in untreated samples. However, the results found in Fig. 4.43 (b) from the methodology used to trace subsurface strain highlight that these samples suffered more severely from plastic deformation due to higher cyclical strain in the subsurface from wear testing. These higher equivalent strain values may be explained by the presence of cross-hatched features in the shot-peened subsurface (Fig. 4.9), artifacts of shear deformation introduced by shot-peening. Thus, the strain lines observed from wear may have been influenced by the prior-strained microstructure of the shot-peened samples. One recommendation in future is to take the samples and analyze them using electron back scatter diffraction (EBSD) to analyze the grain orientation and shearing damage of the subsurface of worn and unworn samples to fully understand this phenomenon and the true value of these equivalent strain calculations. It is further recommended that a wear marker be used in future wear testing to facilitate equivalent strain calculations.

## CHAPTER 6: CONCLUSIONS

### 6.1 Conclusions

From the material characterization as well as mechanical and tribological testing of the alpha PTA-SFFF Ti-TiB material described, with a concentration on wear and fatigue behaviour, the following conclusions can be summarised from this investigation:

- The PTA-SFFF process offers a new alternative manufacturing method which can reduce machining needs by producing low-porosity, near-net shaped parts with coherent Ti-TiB structures. Directionally aimed tensile and compressive testing of AM PTA-SFFF blocks showed a near-isotropic behaviour within the structure, despite AM layering strategies used. Moreover, no unmelted powder zones were noted and bead boundaries were found to be indistinguishable in the etched microstructure. This highlights the goodness of the AM build strategy used to produce as-received samples and the potential of the PTA-SFFF as a competitive alternate manufacturing method to conventional methodologies as opposed to other AM strategies.
- From nanoindentation testing varying from 1-3 mN applied loads, the average reduced modulus of elasticity and nanohardness of samples studied was  $124.58 \pm 7.90$  GPa and  $4.49 \pm 0.32$  GPa, respectively. Using ratios between nanohardness and reduced modulus of elasticity values, ratios of  $H/E_r$  and  $H^3/E_r^2$  are calculated as an indication of wear resistance are 0.036 and 0.006 GPa, respectively. This can be used as a fundamental measure in comparing this material to others in design consideration in future applications. Nanoindentation testing is suggested for use

as an efficient, highly non-destructive analysis method for material characterization means.

- From fatigue testing, overall the fatigue performance of shot-peened samples in this study was superior to untreated samples in both the low and high cycle fatigue regimes. The fitted endurance limit from testing obtained for untreated samples was found to be  $247.8 \pm 5.4$  MPa and for shot-peened samples  $318.3 \pm 5.4$  MPa, which highlights an approximate 28% increase in fatigue resistance obtained through shot-peening. This is attributed to the localized surface hardening and related microstructural changes from cold work as well as introduced residual compressive stresses from the shot peening stage, which helped mitigate and impede crack initiation and initial crack propagation. It is recommended that in fatigue scenarios where the applied stress is anticipated to approach or more 242.4 MPa for this as-received material, that shot peening with paired post-grinding/polishing in the described methodology be applied to ensure that samples have a higher survivability in application.
- From pin-on-disk testing, two different wear regimes were observed in the 1N-17.5 N loading range of as-received, untreated samples. A transition in wear behaviour was found to have occurred at the 10 N applied normal load. The dominating wear mechanism observed in the lower load regime ( $\leq 10$  N) appear to be oxidative wear accompanied with weight gain of the steel counterface balls. In the higher load regime ( $>10$  N), MMLs are observed which consist of fractured TiB particles as well as Ti and Fe oxide in a severely deformed Ti layer. Severe plastic deformation is further highlighted, as well as oxidative and abrasive wear mechanisms are

further observed accompanied with weight loss of the steel counterface balls in the higher load regime. These observations describe the key wear mechanisms observed and help shed light to the fundamental tribological behaviour of Ti-TiB materials.

- Described shot-peening treatment followed by mild grinding and polishing was ultimately found to lead to maintained wear resistance in samples, with similar COF and wear rates obtained as well as comparable counterface and debris observations. Three key differences observed between the shot-peened and untreated wear testing results were: (1) shot-peened samples did not have a transitional point in wear and were found to stay within the Regime I described in the untreated testing scheme, (2) wear was more prominently dominated by oxidation wear for shot-peened samples, and (3) the 15N shot-peened sample had higher equivalent strain values obtained in its subsurface than the higher loaded 17.5N untreated sample. As shot-peened samples stayed within the described Regime I and did not transition to Regime II, where signs of onset severe occurred, it is suggested that shot-peening be used in wear applications past 17.5N to delay severe wear in application.
- TiB particles were found to have a strong interfacial bond and coherent relationship to the alpha Ti structure, with no voids observed in the structure at Ti-TiB interfaces. TiB particles are known to be a low-cost composite addition to Ti as well as have similar material properties and good crystallographic compatibility to Ti. Moreover, no particle pull-out was observed in fatigue testing and TiB particles

were observed to block strain movement in the subsurface in wear testing. For these reasons, it is suggested that TiB makes an ideal reinforcement addition in Ti alloys.

## **6.2 Recommendations**

To further expand what is known about the Ti-TiB materials and the capabilities of the PTA-SFFF process, it would be recommended to repeat a similar testing scheme as presented with varying levels of boron concentrations varying from 0-15 wt% to compare with other studies conducted using Ti-TiB materials. This would help better identify whether any anisotropic or directional behaviour is observed from the manufacturing methods used with increasing/decreasing amounts of boron within the structure as well as provide a guideline to users on optimal amounts of boron to add to the structure for desired properties. Additionally, it could be suggested to vary boron percentages in other popularly used Ti alloys such as Ti-6Al-4V to explore its influence on other Ti alloys produced through the PTA-SFFF process. Moreover, it would be beneficial to explore the influence of shot-peening parameters such as shot-peening time and intensity to optimize its application for this material. It is recommended that the compressive residual stresses introduced through shot-peening be analyzed through XRD analysis as well be used to compliment microhardness profiling.

Additional future work that may be recommended to further develop this research would be to explore the influence of thermal oxidation may have on the wear and fatigue properties of these samples as an additional method of wear and fatigue improvement. In the works of Dalili et al. [125] from this research group, thermal oxidation has been used as a proven wear improvement treatment on a composite Ti-6Al-4V featuring 10 wt% TiC.

The works of Ebrahimi and Khosroshahi [126] illustrated that thermal oxidation can both improve or negatively impact fatigue behaviour with Ti-4Al-2V based on oxidation temperature due to the simultaneous effect of compressive residual stresses and oxide layer scaling. Moreover, the results from Unal et al. [39] showed that a combination of severe shot-peening and thermal oxidation for CP Ti can result in improved wear properties in samples.

Finally, as mentioned earlier, one last recommendation to be made to compliment this study would be to take the samples and analyze them using electron back scatter diffraction (EBSD) to analyze the grain orientation and shearing damage of the subsurface of worn and unworn samples. This would help in fully understanding why the equivalent strain values of the shot-peened samples were higher than the untreated samples. Additionally, it is suggested that in future wear testing, a subsurface marker should be used to calculate the subsurface wear equivalent strain values to facilitate the analysis and calculation of this component.



## REFERENCES

- [1] M. Niinomi, "Mechanical properties of biomedical titanium alloys," *Mater. Sci. Eng. A*, vol. 243, pp. 231–236, 1998.
- [2] M. J. J. Donachie, "A Primer on Titanium and Its Alloys," in *Titanium - A Technical Guide*, 2nd ed., Materials Park: ASM International, 2000, pp. 1–3.
- [3] G. Lütjering and J. C. Williams, *Titanium : Engineering Materials and Processes*, 2nd ed. New York: Springer, 2007.
- [4] S. A. Niknam, R. Khettabi, and V. Songmene, "Machinability and Machining of Titanium Alloys: A Review," in *Machining of Titanium Alloys*, J. P. Davim, Ed. New York: Springer-Verlag Berlin Heidelberg, 2014, pp. 1–10.
- [5] P. J. Arrazola, A. Garay, L. M. Iriarte, M. Armendia, S. Marya, and F. Le Maître, "Machinability of titanium alloys (Ti6Al4V and Ti555.3)," *J. Mater. Process. Technol.*, vol. 209, no. 5, pp. 2223–2230, 2009.
- [6] R. Storm and K. Loutfy, "Plasma Transferred Arc Solid Free Form Fabrication (Rapid Manufacturing)." [Online]. Available: <http://www.mercorp.com/pta.pdf>. [Accessed: 05-Sep-2018].
- [7] S. Li, K. Kondoh, H. Imai, B. Chen, L. Jia, and J. Umeda, "Microstructure and mechanical properties of P/M titanium matrix composites reinforced by in-situ synthesized TiC-TiB," *Mater. Sci. Eng. A*, vol. 628, pp. 75–83, 2015.
- [8] A. P. I. Popoola, L. Phume, S. Pityana, and V. S. Aigbodion, "In-situ formation of laser Ti6Al4V-TiB composite coatings on Ti6Al4V alloy for biomedical application," *Surf. Coatings Technol.*, vol. 285, pp. 161–170, 2016.
- [9] C. Cai, B. Song, C. Qiu, L. Li, P. Xue, Q. Wei, J. Zhou, H. Nan, H. Chen, and Y. Shi, "Hot isostatic pressing of in-situ TiB/Ti-6Al-4V composites with novel reinforcement architecture, enhanced hardness and elevated tribological properties," *J. Alloys Compd.*, vol. 710, pp. 364–374, 2017.
- [10] D. B. Boudreau, "Characterization of Powder Metallurgy Lightweight Alloys," MAsc Thesis - University of Windsor, 2017.
- [11] F. C. Campbell, *Phase Diagrams: Understanding the Basics*. Ohio: ASM International.
- [12] J. R. Evlon, D. Newman and J. K. Thorne, "Wrought Titanium and Titanium Alloys - Titanium Alloy Castings, Properties and Selection: Nonferrous Alloys and Special-Purpose Materials," in *ASM Handbook*, Materials Park: ASM International, 1990, pp. 634–646.

- [13] W. D. J. Callister and D. G. Rethwisch, *Materials Science and Engineering - An Introduction*, 8th ed. Hoboken: John Wiley & Sons, Inc., 2010.
- [14] D. R. Askeland and P. P. Fulay, *Essentials of Materials Science and Engineering*, 2nd ed. Connecticut: Cengage Learning, 2010.
- [15] A. Fitzner, D. G. L. Prakash, J. Quinta da Fonseca, M. Thomas, S.-Y. Zhang, J. Kelleher, P. Manuel, and M. Preuss, "The effect of aluminium on twinning in binary alpha-titanium," *Acta Mater.*, vol. 103, pp. 341–351, 2016.
- [16] M. Ahmed, D. Wexler, G. Casillas, D. G. Savvakina, and E. V. Pereloma, "Strain rate dependence of deformation-induced transformation and twinning in a metastable titanium alloy," *Acta Mater.*, vol. 104, pp. 190–200, 2016.
- [17] L. M. Gammon, R. D. Briggs, J. M. Packard, K. W. Batson, R. Boyer, and C. W. Domby, "Metallography and Microstructures: Metallography and Microstructures of Titanium and Its Alloys," in *ASM Handbook*, Materials Park: ASM International, 2004, pp. 899–917.
- [18] K. G. Budinski, "Tribological properties of titanium alloys," *Wear*, vol. 151, no. 2, pp. 203–217, 1991.
- [19] A. Molinari, G. Straffelini, B. Tesi, and T. Bacci, "Dry sliding wear mechanisms of the Ti6Al4V alloy," *Wear*, vol. 208, no. 1–2, pp. 105–112, 1997.
- [20] S. Yerramareddy and S. Bahadur, "The effect of laser surface treatments on the tribological behavior of Ti-6Al-4V," *Wear*, vol. 157, no. 2, pp. 245–262, 1992.
- [21] K. Farokhzadeh and A. Edrissy, "Transition between mild and severe wear in titanium alloys," *Tribol. Int.*, vol. 94, pp. 98–111, 2016.
- [22] K. Miyoshi and D. H. Buckley, "Relationship Between the Ideal Tensile Strength and the Friction Properties of Metals in Contact With Nonmetals and Themselves," *NASA Technical P*, no. Vol. 1883. NASA, pp. 1–10, 1981.
- [23] D. H. Buckley, *Surface Effects in Adhesion, Friction, Wear, and Lubrication*, 1st ed. Amsterdam: Elsevier Scientific, 1981.
- [24] Q. Wang, P. Zhang, D. Wei, X. Chen, R. Wang, and H. Wang, "Microstructure and Sliding Wear Behavior of Pure Titanium Surface Modified by Double-Glow Plasma Surface Alloying with Nb," *Mater. Des.*, vol. 52, pp. 265–273, 2013.
- [25] R. G. Budynas and J. K. Nisbett, "Fatigue Failure Resulting from Variable Loading," in *Shigley's Mechanical Engineering Design*, 10th ed., New York: McGraw-Hill Education, 2015, pp. 274–348.
- [26] G. E. Dieter, "Fatigue of Metals," in *Mechanical Metallurgy*, London: McGraw-Hill Book Company, 1988, pp. 296–336.

- [27] “Fatigue and Fracture Properties of Titanium Alloys,” in *ASM Handbook Volume 9: Fatigue and Fracture*, Materials Park, 1996, pp. 829–853.
- [28] U. Bathini, T. S. Srivatsan, A. K. Patnaik, and C. C. Menzemer, “Mechanisms Governing Fatigue, Damage, and Fracture of Commercially Pure Titanium for Viable Aerospace Applications,” *J. Aerosp. Eng.*, vol. 24, no. October, pp. 415–424, 2011.
- [29] K. Takao and K. Kusukawa, “Low-cycle fatigue behavior of commercially pure titanium,” *Mater. Sci. Eng. A*, vol. A213, pp. 81–85, 1996.
- [30] J. Schijve, “Fatigue Properties,” in *Fatigue of Structures and Materials*, Berlin: Springer Science+Business Media, 2009, pp. 141–170.
- [31] G. R. Leverant, B. S. Langer, A. Yuen, and S. W. Hopkins, “Surface residual stresses, surface topography and the fatigue behavior of Ti-6Al-4V,” *Metall. Trans. A*, vol. 10, no. 2, pp. 251–257, 1979.
- [32] P. Starker, H. Wohlfahrt, and E. Macherauch, “Subsurface Crack Initiation During Fatigue As a Result of Residual Stresses,” *Fatigue Fract. Eng. Mater. Struct.*, vol. 1, no. 3, pp. 319–327, 1979.
- [33] L. Wagner and G. Luetjeringe, “Influence Of Shot Peening on the Fatigue Behavior of Titanium Alloys,” in *International Conference on Shot Peening - 1*, 1981, pp. 453–460.
- [34] F. Petit-Renaud, “Optimization of the Shot Peening Parameters,” in *Shot Peening - Proceedings of the 8th International Conference on Shot Peening*, L. Wagner, Ed. Weinheim: Wiley-VCH Verlag GmbH & Co. KGaA, 2003.
- [35] B. K. C. Ganesh, N. Ramanaih, and P. V. Chandrasekhar Rao, “Dry Sliding Wear Behavior of Ti – 6Al – 4V Implant Alloy Subjected to Various Surface Treatments,” *Trans. Indian Inst. Met.*, vol. 65, no. October, pp. 425–434, 2012.
- [36] B. K. C. Ganesh, W. Sha, N. Ramanaiah, and A. Krishnaiah, “Effect of shotpeening on sliding wear and tensile behavior of titanium implant alloys,” *J. Mater. Des.*, vol. 56, pp. 480–486, 2014.
- [37] J. F. Archard, “Contact and rubbing of flat surfaces,” *J. Appl. Phys.*, vol. 24, no. 8, pp. 981–988, 1953.
- [38] O. Unal, A. C. Karaoglanli, R. Varol, and A. Kobayashi, “Microstructure evolution and mechanical behavior of severe shot peened commercially pure titanium,” *Vaccum*, vol. 110, pp. 202–206, 2014.
- [39] O. Unal, A. C. Karaoglanli, Y. Ozgurluk, K. M. Doleker, E. Maleki, and R. Varol, “Wear Behavior of Severe Shot Peened and Thermally Oxidized Commercially Pure Titanium,” in *Advanced Structured Materials*, no. vol. 92, New York:

Springer International Publishing, 2019, pp. 461–470.

- [40] Q. Yang, W. Zhou, Z. Niu, X. Zheng, Q. Wang, X. Fu, G. Chen, and Z. Li, “Effect of different surface asperities and surface hardness induced by shot-peening on the fretting wear behavior of Ti-6Al-4V,” *Surf. Coat. Technol.*, vol. 349, pp. 1098–1106, 2018.
- [41] L. H. Burck, C. P. Sullivan, and C. H. Wells, “Fatigue of a glass bead blasted nickel-base superalloy,” *Metall. Trans.*, vol. 1, no. JUNE, pp. 1595–1600, 1970.
- [42] P. He, M. Yang, T. Lin, and Z. Jiao, “Improving the strength of brazed joints with in situ synthesized TiB whiskers,” *J. Alloys Compd.*, vol. 509, no. 29, pp. L289–L292, 2011.
- [43] F. Weng, H. Yu, C. Chen, J. Liu, L. Zhao, J. Dai, and Z. Zhao, “Effect of process parameters on the microstructure evolution and wear property of the laser cladding coatings on Ti-6Al-4V alloy,” *J. Alloys Compd.*, vol. 692, pp. 989–996, 2017.
- [44] F. Ma, P. Liu, W. Li, X. Liu, X. Chen, K. Zhang, D. Pan, and W. Lu, “The mechanical behavior dependence on the TiB whisker realignment during hot-working in titanium matrix composites,” *Sci. Rep.*, vol. 6, no. October, pp. 1–9, 2016.
- [45] S. Pouzet, P. Peyre, C. Gorny, O. Castelnau, T. Baudin, F. Brisset, C. Colin, and P. Gadaud, “Additive layer manufacturing of titanium matrix composites using the direct metal deposition laser process,” *Mater. Sci. Eng. A*, vol. 677, pp. 171–181, 2016.
- [46] S. Gorsse, J. . Chaminade, and Y. Le Petitcorps, “In situ preparation of titanium base composites reinforced by TiB single crystals using a powder metallurgy technique,” *Compos. Part A Appl. Sci. Manuf.*, vol. 29, no. 9, pp. 1229–1234, 1998.
- [47] A. Miklaszewski, “Ultrafast densification and microstructure evolution of in situ Ti/TiB metal matrix composite obtained by PPS approach,” *Int. J. Refract. Met. Hard Mater.*, vol. 65, pp. 34–38, 2017.
- [48] R. Chaudhari and R. Bauri, “Reaction mechanism, microstructure and properties of Ti – TiB in situ composite processed by spark plasma sintering,” *Mater. Sci. Eng. A*, vol. 587, pp. 161–167, 2013.
- [49] S. Tamirisakandala, R. B. Bhat, D. B. Miracle, S. Boddapati, R. Bordia, R. Vanover, and V. K. Vasudevan, “Effect of boron on the beta transus of Ti-6Al-4V alloy,” *Scr. Mater.*, vol. 53, no. 2, pp. 217–222, 2005.
- [50] S. Dubey, R. J. Lederich, and W. O. Soboyejo, “Fatigue and Fracture of Damage-Tolerant In Situ Titanium Matrix Composites,” *Metall. Mater. Trans. A*, vol. 28, no. 7883, pp. 2037–2047, 1997.

- [51] W. Lu, D. Zhang, X. Zhang, and R. Wu, “Creep Rupture Life of in situ synthesized ( TiB +TiC )/ Ti Matrix Composites,” *Scr. Mater.*, vol. 44, pp. 2449–2455, 2001.
- [52] Z. Fan, A. P. Miodownik, L. Chandrasekaran, and M. Ward-Close, “The Young’s moduli of in situ Ti / TiB composites obtained by rapid solidification processing,” *J. Mater.*, vol. 29, pp. 1127–1134, 1994.
- [53] W. O. Soboyejo, R. J. Lederic, and S. M. L. Sastry, “Mechanical behavior of damage tolerant TiB whisker-reinforced in situ titanium matrix composites,” *Acta Metall. Mater.*, vol. 42, pp. 2579–2591, 1994.
- [54] S. Ghesmati Tabrizi, A. Babakhani, S. A. Sajjadi, and W. J. Lü, “Microstructural aspects of in-situ TiB reinforced Ti-6Al-4V composite processed by spark plasma sintering,” *Trans. Nonferrous Met. Soc. China*, vol. 25, no. 5, pp. 1460–1467, 2015.
- [55] A. Miklaszewski, “Effect of starting material character and its sintering temperature on microstructure and mechanical properties of super hard Ti/TiB metal matrix composites,” *Int. J. Refract. Met. Hard Mater.*, vol. 53, pp. 56–60, 2015.
- [56] N. Makuch, M. Kulka, P. Dziarski, and D. Przystacki, “Laser surface alloying of commercially pure titanium with boron and carbon,” *Opt. Lasers Eng.*, vol. 57, pp. 64–81, 2014.
- [57] M. Kaczmarek, M. U. Jurczyk, A. Miklaszewski, A. Paszel-Jaworska, A. Romaniuk, N. Lipińska, J. Żurawski, P. Urbaniak, and K. Jurczyk, “In vitro biocompatibility of titanium after plasma surface alloying with boron,” *Mater. Sci. Eng. C*, vol. 69, pp. 1240–1247, 2016.
- [58] A. Miklaszewski, M. U. Jurczyk, K. Jurczyk, and M. Jurczyk, “Plasma surface modification of titanium by TiB precipitation for biomedical applications,” *Surf. Coatings Technol.*, vol. 206, no. 2–3, pp. 330–337, 2011.
- [59] Y. S. Tian, Q. Y. Zhang, and D. Y. Wang, “Study on the microstructures and properties of the boride layers laser fabricated on Ti-6Al-4V alloy,” *J. Mater. Process. Technol.*, vol. 209, no. 6, pp. 2887–2891, 2009.
- [60] Y. S. Tian, “Growth mechanism of the tubular TiB crystals in situ formed in the coatings laser-borided on Ti-6Al-4V alloy,” *Mater. Lett.*, vol. 64, no. 22, pp. 2483–2486, 2010.
- [61] M. Ozerov, N. Stepanov, A. Kolesnikov, V. Sokolovsky, and S. Zhrebtsov, “Brittle-to-ductile transition in a Ti–TiB metal-matrix composite,” *Mater. Lett.*, vol. 187, no. October 2016, pp. 28–31, 2017.
- [62] M. Y. Koo, J. S. Park, M. K. Park, K. T. Kim, and S. H. Hong, “Effect of aspect

ratios of in situ formed TiB whiskers on the mechanical properties of TiBw/Ti-6Al-4V composites,” *Scr. Mater.*, vol. 66, no. 7, pp. 487–490, 2012.

- [63] P. Nandwana, “Titanium Boride Formation and Its Subsequent Influence on Morphology and Crystallography of Alpha Precipitates in Titanium Alloys,” University of North Texas, 2013.
- [64] S. Aich and K. S. Ravi Chandran, “TiB whisker coating on titanium surfaces by solid-state diffusion: Synthesis, microstructure, and mechanical properties,” *Metall. Mater. Trans. A*, vol. 33, no. 11, pp. 3489–3498, 2002.
- [65] S. S. Sahay, K. S. Ravichandran, R. Atri, B. Chen, and J. Rubin, “Evolution of microstructure and phases in in situ processed Ti – TiB composites containing high volume fractions of TiB whiskers,” *J. Mater. Res.*, vol. 14, no. 11, pp. 4214–4223, 1999.
- [66] J. Zhang, W. Ke, W. Ji, Z. Fan, W. Wang, and Z. Fu, “Microstructure and properties of insitu titanium boride (TiB)/titanium (Ti) composites,” *Mater. Sci. Eng. A*, vol. 648, pp. 158–163, 2015.
- [67] B. J. Kooi, Y. T. Pei, and J. T. M. De Hosson, “The evolution of microstructure in a laser clad TiB-Ti composite coating,” *Acta Mater.*, vol. 51, no. 3, pp. 831–845, 2003.
- [68] H. Attar, S. Ehtemam-Haghighi, D. Kent, I. V. Okulov, H. Wendrock, M. Bönisch, A. S. Volegov, M. Calin, J. Eckert, and M. S. Dargusch, “Nanoindentation and wear properties of Ti and Ti-TiB composite materials produced by selective laser melting,” *Mater. Sci. Eng. A*, vol. 688, no. December 2016, pp. 20–26, 2017.
- [69] R. Banerjee, P. C. Collins, and H. L. Fraser, “Laser Deposition of In Situ Ti – TiB Composites,” *Adv. Eng. Mater.*, vol. 4, no. 11, pp. 847–851, 2002.
- [70] *ASM Handbook Volume 3, Alloy Phase Diagrams*, vol. 3. Materials Park: ASM International, 2016.
- [71] K. Soorya Prakash, P. M. Gopal, D. Anburose, and V. Kavimani, “Mechanical, corrosion and wear characteristics of powder metallurgy processed Ti-6Al-4V/B4C metal matrix composites,” *Ain Shams Eng. J.*, pp. 0–7, 2016.
- [72] I. Y. Kim, B. J. Choi, Y. J. Kim, and Y. Z. Lee, “Friction and wear behavior of titanium matrix (TiB+TiC) composites,” *Wear*, vol. 271, no. 9–10, pp. 1962–1965, 2011.
- [73] B. Choi, S. Sung, M. Kim, and Y. Kim, “Evaluation the Properties of Titanium Matrix Composites by Melting Route Synthesis,” *J. Mater. Sci. Technol.*, vol. 24, no. 1, pp. 105–109, 2008.
- [74] B. J. Choi, I. Y. Kim, Y. Z. Lee, and Y. J. Kim, “Microstructure and friction/wear

- behavior of (TiB + TiC) particulate-reinforced titanium matrix composites,” *Wear*, vol. 318, no. 1–2, pp. 68–77, 2014.
- [75] J. Kim, K. Lee, D. Cho, and Y. Lee, “Fretting wear characteristics of titanium matrix composites reinforced by titanium boride and titanium carbide particulates,” *Wear*, vol. 301, no. 1–2, pp. 562–568, 2013.
- [76] T. Saito, H. Takamiya, and T. Furuta, “Thermomechanical properties of P/M  $\beta$  titanium metal matrix composite,” *Mater. Sci. Eng. A*, vol. 243, no. 1–2, pp. 273–278, 1998.
- [77] S. Emura, S. J. I. N. Yang, and M. Hagiwara, “Room-Temperature Tensile and High-Cycle-Fatigue Strength of Fine TiB Particulate-Reinforced Ti-22Al-27Nb Composites,” *Metall. Mater. Trans. A*, vol. 35, pp. 2971–2979, 2004.
- [78] S. Dubey, Y. Li, K. Reece, W. O. Soboyejo, and R. J. Lederich, “Fatigue crack growth in an in-situ titanium matrix composite,” *Mater. Sci. Eng. A*, vol. 266, pp. 303–309, 1999.
- [79] P. Majumdar, S. B. Singh, and M. Chakraborty, “Fatigue behaviour of in situ TiB reinforced  $\beta$  -titanium alloy composite,” *Mater. Lett.*, vol. 64, no. 24, pp. 2748–2751, 2010.
- [80] S. Gorsse and D. B. Miracle, “Mechanical properties of Ti-6Al-4V / TiB composites with randomly oriented and aligned TiB reinforcements,” *Acta Mater.*, vol. 51, pp. 2427–2442, 2003.
- [81] “ASTM F2792-12a Standard Terminology for Additive Manufacturing Technologies.” ASTM International, West Conshohocken, PA, pp. 1–3, 2013.
- [82] L. Nickels, “Additive manufacturing: A user’s guide,” *Met. Powder Rep.*, vol. 71, no. 2, pp. 100–105, 2016.
- [83] T. Debroy, H. L. Wei, J. S. Zuback, T. Mukherjee, J. W. Elmer, J. O. Milewski, A. M. Beese, A. Wilson-heid, A. De, and W. Zhang, “Progress in Materials Science Additive manufacturing of metallic components – Process , structure and properties,” *Prog. Mater. Sci.*, vol. 92, pp. 112–224, 2018.
- [84] D. Herzog, V. Seyda, E. Wycisk, and C. Emmelmann, “Additive manufacturing of metals,” *Acta Mater.*, vol. 117, pp. 371–392, 2016.
- [85] S. Singh, S. Ramakrishna, and R. Singh, “Material issues in additive manufacturing : A review,” *J. Manuf. Process.*, vol. 25, pp. 185–200, 2017.
- [86] Y. Huang, M. C. Leu, J. Mazumder, and A. Donmez, “Additive Manufacturing : Current State , Future Potential , Gaps and Needs , and Recommendations,” *Journal Manuf. Sci. Eng.*, vol. 137, no. February 2015, pp. 1–10, 2015.

- [87] R. Liu, Z. Wang, T. Sparks, F. Liou, and J. Newkirk, "Aerospace applications of laser additive manufacturing," in *Laser Additive Manufacturing - Materials, Design, Technologies, and Applications*, M. Brandt, Ed. Duxford: Woodhead Publishing, Elsevier Ltd., 2017, pp. 351–371.
- [88] B. Dutta and F. H. Froes, "The Additive Manufacturing (AM) of titanium alloys," *Met. Powder Rep.*, vol. 72, no. 2, pp. 96–106, 2017.
- [89] D. Clark, M. T. Whittaker, and M. R. Bache, "Microstructural Characterization of a Prototype Titanium Alloy Structure Processed via Direct Laser Deposition ( DLD )," *Metall. Mater. Trans. B*, vol. 43B, pp. 388–396, 2011.
- [90] P. A. Kobryn and S. L. Semiatin, "Microstructure and texture evolution during solidification processing of Ti – 6Al – 4V," *J. Mater. Process. Technol.*, vol. 135, pp. 330–339, 2003.
- [91] B. E. Carroll, A. Palmer, and A. M. Beese, "ScienceDirect Anisotropic tensile behavior of Ti – 6Al – 4V components fabricated with directed energy deposition additive manufacturing," *Acta Mater.*, vol. 87, pp. 309–320, 2015.
- [92] K. S. Chan, M. Koike, R. L. Mason, and T. Okabe, "Fatigue Life of Titanium Alloys Fabricated by Additive Layer Manufacturing Techniques for Dental Implants," *Metall. Mater. Trans. A*, vol. 44A, no. February, pp. 1010–1023, 2013.
- [93] "Welcome to Manufacturing Unbound." Arcam EBM - a GE Additive company, Mölndal, pp. 1–20, 2018.
- [94] "New manufacturing milestone: 30,000 additive fuel nozzles," *GE Additive*, 2018. [Online]. Available: <https://www.ge.com/additive/blog/new-manufacturing-milestone-30000-additive-fuel-nozzles>. [Accessed: 14-Apr-2019].
- [95] Y. H. Li, X. J. Liang, and T. Fan, "Research development of biomedical titanium alloy," *Appl. Mech. Mater.*, vol. 55–57, no. 2011, pp. 2009–2012, 2011.
- [96] S. Lampman, "Volume 23: Titanium and Its Alloys for Biomedical Implants - Materials for Medical Devices," in *ASM Handbooks*, Materials Park: ASM International, 2012, pp. 223–236.
- [97] G. Manivasagam, D. Dhinasekaran, and A. Rajamanickam, "Biomedical Implants : Corrosion and its Prevention - A Review," *Recent Patents Corros. Sci.*, vol. 2, pp. 40–54, 2010.
- [98] G. Lütjering and J. C. Williams, "Special Properties and Applications of Titanium," in *Titanium*, 2nd ed., New York: Springer, 2007, pp. 383–415.
- [99] S. Nag and R. Banerjee, "Volume 23: Fundamentals of Medical Implant Materials - Materials for Medical Devices," in *ASM Handbook*, Materials Park: ASM International, 2012, pp. 6–17.



- [100] J. Tedesco, B. E. J. Lee, A. Y. W. Lin, D. M. Binkley, K. H. Delaney, J. M. Kwiecien, and K. Grandfield, "Osseointegration of a 3D Printed Stemmed Titanium Dental Implant: A Pilot Study," *Int. J. Dent.*, vol. 2017, 2017.
- [101] S. Tunchel, A. Blay, R. Kolerman, E. Mijiritsky, and J. A. Shibli, "3D Printing/Additive Manufacturing Single Titanium Dental Implants: A Prospective Multicenter Study with 3 Years of Follow-Up," *Int. J. Dent.*, vol. 2016, 2016.
- [102] "Amos - Additive Repair for Aerospace," 2017. [Online]. Available: <http://amos-project.com/amos>. [Accessed: 24-Apr-2019].
- [103] "ASTM-E407 - Standard Practice for Microetching Metals and Alloys." ASTM International, West Conshohocken, pp. 1–22, 2016.
- [104] Y. Xu and P. Yamazaki, Masayoshi Villars, "Inorganic Materials Database for Exploring the Nature of Material," *TiB - National Institute for Materials Science (NIMS)* -, 2011. [Online]. Available: <http://crystdb.nims.go.jp>. [Accessed: 30-Oct-2018].
- [105] L. Reinking, "Examples of Image Analysis Using ImageJ," Millersville, 2007.
- [106] T. Ferreira and W. Rasband, "ImageJ User Guide," 2012.
- [107] "Particle Analysis," *ImageJ*, 2017. [Online]. Available: [https://imagej.net/Particle\\_Analysis](https://imagej.net/Particle_Analysis). [Accessed: 30-Oct-2018].
- [108] "ASTM E384 Standard Test Method for Knoop and Vickers Hardness of Materials." ASTM International, Conshohocken, PA, pp. 1–43, 2012.
- [109] A. A. Elmustafa and D. S. Stone, "Nanoindentation and the indentation size effect : Kinetics of deformation and strain gradient plasticity," *J. Mech. Phys. Solids*, vol. 51, pp. 357–381, 2003.
- [110] W. C. Oliver and G. M. Pharr, "An improved technique for determining hardness and elastic modulus using load and displacement sensing indentation experiments," *J. Mater. Res.*, vol. 7, no. 6, pp. 1564–1583, 1992.
- [111] "Probe Calibration Service Document - UBI 1 Nano Mechanical Tester." Hysitron, Minneapolis, pp. 1–6, 2014.
- [112] A. Hynowska, E. Pellicer, J. Fornell, S. González, N. Van Steenberge, S. Suriñach, A. Gebert, M. Calin, J. Eckert, M. Dolores, and J. Sort, "Nanostructure  $\beta$ -phase Ti-31.0Fe-9.0Sn and sub- $\mu\text{m}$  structured Ti-39.3Nb-13.3Zr-10.7Ta alloys for biomedical applications: Microstructure benefits on the mechanical and corrosion performances," *Mater. Sci. Eng. C*, vol. 32, no. 8, pp. 2418–2425, 2012.
- [113] A. Leyland and A. Matthews, "On the significance of the H/E ratio in wear control: A nanocomposite coating approach to optimised tribological behaviour,"

*Wear*, vol. 246, no. 1–2, pp. 1–11, 2000.

- [114] J. F. Archard and W. Hirst, “The Wear of Metals under Unlubricated Conditions,” in *Series A, Mathematical and Physical Sciences*, 1956, vol. 236, no. 1206, pp. 397–410.
- [115] J. Xu, G. D. Wang, X. Lu, L. Liu, P. Munroe, and Z. H. Xie, “Mechanical and corrosion-resistant properties of Ti-Nb-Si-N nanocomposite films prepared by a double glow discharge plasma technique,” *Ceram. Int.*, vol. 40, no. 6, pp. 8621–8630, 2014.
- [116] “ASTM F3122-14 Standard Guide for Evaluating Mechanical Properties of Metal Materials Made via Additive Manufacturing Processes.” ASTM International, West Conshohocken, PA, pp. 1–6, 2014.
- [117] “ASTM E9-09 Standard Test Methods of Compression Testing of Metallic Materials at Room Temperature.” ASTM International, West Conshohocken, PA, pp. 1–9, 2018.
- [118] “ASTM E8/E8M-16a Standard Test Methods for Tension Testing of Metallic Materials.” ASTM International, West Conshohocken, PA, pp. 1–27, 2016.
- [119] B. F. Decker and J. S. Kasper, “The crystal structure of TiB,” *Acta Crystallogr.*, vol. 7, no. 1, pp. 77–80, 1954.
- [120] J. Zhang and A. T. Alpas, “Delamination wear in ductile materials containing second phase particles,” *Materials Science and Engineering A*, vol. 160. Elsevier B.V., pp. 25–35, 1993.
- [121] E. Wycisk, “Fatigue performance of laser additive Manufactured Ti – 6Al – 4V in very high cycle fatigue regime up to  $10^9$  cycles,” *Front. Mater.*, vol. 2, pp. 2–9, 2015.
- [122] D. B. Boudreau, L.-A. DiCecco, O. Gali, and A. Edrissy, “Fatigue Behaviour of Additive Manufactured Ti-TiB,” *MRS Adv.*, vol. 3, no. 62 (International Materials Research Congress XXVII), pp. 3641–3653, 2018.
- [123] T. S. Srivatsan, W. O. Soboyejo, and R. J. Lederich, “Tensile deformation of a titanium-alloy and fracture behaviour composite,” *Compos. Part A*, no. 1997, pp. 365–376, 1997.
- [124] W. Lu, D. I. Zhang, X. Zhang, Y. Bian, and R. Wu, “Microstructure and tensile properties of in situ synthesized ( TiB w + TiC p )/ Ti6242 composites,” *J. Mater. Sci.*, vol. 6, pp. 3707–3714, 2001.
- [125] N. Dalili, A. Edrissy, K. Farokhzadeh, J. Li, J. Lo, and A. R. Riahi, “Improving the wear resistance of Ti-6Al-4V/TiC composites through thermal oxidation (TO),” *Wear*, vol. 269, no. 7–8, pp. 590–601, 2010.

- [126] A. R. Ebrahimi, F. Zarei, and R. A. Khosroshahi, "Effect of thermal oxidation process on fatigue behavior of Ti-4Al-2V alloy," *Surf. Coatings Technol.*, vol. 203, no. 3–4, pp. 199–203, 2008.

## APPENDIX A: RESEARCH CONTRIBUTIONS

The following points highlight research contributions made throughout the duration of this master's research.

1. Boudreau D, **DiCecco L**, Gali O, Edrisy A. Fatigue Behaviour of Additive Manufactured Ti-TiB. *MRS Advances*, Vol. 3, no. 62, pp. 3641-3653, 2018. *Published peer-reviewed journal paper.*
2. Urbanic J, **DiCecco L**. Bead Representation and Virtual Surface Roughness Evaluation Challenges for Additive Manufacturing Material Extrusion Processes. *The International Journal of Advanced Manufacturing Technology*, Vol. 102, no. 9-12, pp 2993-3009, 2018. *Published peer-reviewed journal paper.*
3. **DiCecco L**, Edrisy A. Wear Mechanisms for Additive Manufacturing Titanium Featuring TiB Reinforcement. *Journal submitted 06/2019 to Tribology International for peer-review.*
4. **DiCecco L**, Edrisy A. Shot Peening Influence on the Fatigue Behaviour of Additive Manufactured Ti-TiB Material. *Journal in preparation for submission.*
5. **DiCecco L**, Edrisy A Fatigue Behaviour of Shot-Peened Additive Manufactured Ti-TiB. Oral conference presentation at the 2019 Canadian Materials Science Conference.
  - a. Received the Best Podium Presentation Award in the Additive Manufacturing Session
6. **DiCecco L**, Edrisy A. Properties and Performance of Additive Manufactured Titanium with TiB Reinforcement. Conference poster presentation at the TMS 2019 Annual Meeting & Exhibition.

7. **DiCecco L**, Urbanic J, Edrisy A. Wear Mechanisms for Additive Manufactured Titanium with TiB Reinforcement. Oral conference presentation at the 2018 Canadian Materials Science Conference.
  - a. Received the Best Podium Presentation Award in the Additive Manufacturing Session
8. **DiCecco L**. Move Over Plastic, We're 3D Printing Titanium. Competitive oral presentation at the University of Windsor institutional and provincial Three Minute Thesis (3MT) competition.
  - a. Won 2nd place at University of Windsor competition and went forward to present at the provincial level to represent the University of Windsor.

## VITA AUCTORIS

NAME: Liza-Anastasia DiCecco

PLACE OF BIRTH: Windsor, ON

YEAR OF BIRTH: 1995

EDUCATION: École Secondaire E. J. Lajeunesse, Windsor, ON,  
2013

University of Windsor, B.A.Sc., Windsor, ON,  
2017

University of Windsor, M.A.Sc., Windsor, ON,  
2019